DISSERTATION

Hybrid material toughening of photopolymers in 3D printing

carried out for the purpose of obtaining the degree of Doctor technicae (Dr. techn.), submitted at TU Wien, Faculty of Mechanical and Industrial Engineering, by

Dipl.-Ing. Mag. Johannes STÖGERER, BSc.

Matr. Nr. 0900820

under the supervision of

Univ.-Prof. Dipl.-Ing. Dr. mont. Jürgen Stampfl

(Institute of Materials Science and Technology, E308)

Vienna, April, 2022

Reviewed by

Univ. Prof. Dipl.-Ing. Dr. techn. Robert Liska	Univ. Prof. Dr. Otmar Kolednik
Institute of Applied Synthetic Chemistry,	Erich Schmid Institute of Materials Science,
TU Wien	Austrian Academy of Sciences
Getreidemarkt 9, 1060 Wien	Jahnstrasse 12, 8700 Leoben

Affidavit

I declare in lieu of oath, that I wrote this thesis and performed the associated research myself, using only literature cited in this volume. If text passages from sources are used literally, they are marked as such.

I confirm that this work is original and has not been submitted elsewhere for any examination, nor is it currently under consideration for a thesis elsewhere.

I acknowledge that the submitted work will be checked electronically-technically using suitable and state-of-the-art means (plagiarism detection software). On the one hand, this ensures that the submitted work was prepared according to the high-quality standards within the applicable rules to ensure good scientific practice "Code of Conduct" at the TU Wien. On the other hand, a comparison with other student theses avoids violations of my personal copyright.

Vienna, March, 2022

Signature

Acknowledgements

I would like to thank the following people, who helped and supported me and without whom I would not have been able to complete this research.

First and foremost, I would like to thank my supervisor Prof. Jürgen Stampfl, who gave me the opportunity to work in a fascinating and inspiring research area and always provided insight and knowledge into the subject matter. His enthusiasm for the topic, his support, encouragement, and patience steered me through this research.

This work would not have been feasible without the support from my colleagues. You helped me solving various questions, both scientific and other ones. My special gratitude goes to Dr. Sonja Baumgartner, who helped me find the right way through the thicket of a doctoral programme and Anna-Lea Kutsch whose work attitude motivated me to finish this thesis in the planned timeframe. Thanks to Bernhard Steyrer, Jürgen Kollmer, Thaddäa Rath, Julia Schönherr, Bettina Koch, and Alexander Hochwallner who made the last three years unforgettable.

Special thanks to Dr. Thomas Koch and Stefan Zellhofer, who helped me plan, conduct, and evaluate countless experiments.

Thanks to my friends who had to put up with my stresses and moans for the past three years and provided distraction whenever necessary.

And my biggest thanks go to my family for all the support you have shown me through this research.

Table of Contents

Acknowledgements I

Table of Contents I

Abstract III

Kurzfassung IV

List of Figures V

List of Tables IX

List of Abbreviations X

1 Introduction and Motivation 1

2 Fundamentals 3

2.1 Manufacturing technologies 3

2.2 Additive manufacturing 4

2.2.1 Stereolithography 6

2.2.2 Digital Light Processing 6

2.2.3 Inkjet Printing 7

2.3 Photopolymers 12

2.3.1 Free radical chain polymerisation 13

2.3.2 Classification of photopolymers 15

2.3.3 Additives 16

2.4 Thermo-mechanical testing 21

2.4.1 Tensile test 21

2.4.2 Bending test 24

2.4.3 Dynamic mechanical analysis 26

2.4.4 Hardness tests 29

2.4.5 Impact strength 30

2.4.6 Fracture mechanics 32

2.4.6.3 Toughening of photopolymers 39

3 Material composition and printing method 41

3.1 Resin Compositions 41

3.1.1 TCP I Resin 41

3.1.2 TCP II Resin 42

3.1.3 TCP III Resin 44

3.2 Ink Composition 46

3.2.1 Cyano Ink 46

3.2.2 Tango Ink 47

3.3 Hybrid printing system 48

3.3.1 SLA Printer 48

3.3.2 Inkjet system 52

3.3.3 Hybrid printing system 54

4 Experimental 56

4.1 Assessment of thermo-mechanical anisotropy 56

4.1.1 Sample preparation 57

4.1.2 Thermo-mechanical tests 57

4.1.3 Results 61

4.2 Bio-inspired toughening of a polymer composite 69

4.2.1 Sample preparation 71

4.2.2 Thermo-mechanical testing 74

4.2.3 Results 75

4.3 Application of the hybrid printing system to enhance fracture toughness 86

4.3.1 Sample preparation 87

4.3.2 Testing 88

4.3.3 Results 92

5 Discussion and Outlook 99

5.1 Resin characterisation and thermo-mechanical performance 99

5.2 Toughness modification by 3D hybrid printing 101

5.3 Application of the material inhomogeneity effect 103

5.4. Outlook 105

References i

Abstract

Stereolithography is the oldest 3D printing technique allowing high spatial resolution and almost arbitrary geometries to be produced. One of the fundamental disadvantages of stereolithography is the limitation to one raw material being processible at the same time. In this work, a new approach for the modification of 3D printed parts is developed by using an innovative hybrid 3D printing system. This machine allows to simultaneously use two separate additive manufacturing processes, namely stereolithography and inkjet printing.

In the first part of this work, the stereolithographic process is tested and analysed with respect to the mechanical properties of the produced parts. The resin used is mainly based on monomers and ceramic fillers. This composite material is utilised to print standardised mechanical test specimens. Relevant mechanical parameters in the field of composite materials as well as potential anisotropic behaviour because of varying layer orientation are assessed. Bending and fracture toughness tests yield reasonable results for a composite material (i.e., 6000 MPa for the bending modulus, 60 MPa for 3-point bending strength, 2 % elongation at break, and 1.6 MPa*m$^{(1/2)}$ for fracture toughness, respectively. No indication of anisotropy is found.

The second part deals with the application of the hybrid printing system. Different material combinations are tested for the modification of the mechanical properties. The focus is on the improvement of the fracture toughness of inherently brittle composite materials. In contrast to conventional toughening methods, where the composition of the resin is adapted, the toughening effect arises from the combination of two different materials. The underlying material inhomogeneity effect is inspired by biological materials and allows the increase of fracture toughness without the deterioration of strength and stiffness.

The hybrid 3D printing system is successfully used to toughen the composite resin. The semi-automatic process enables the production of samples featuring alternating layers of materials with strongly varying mechanical properties. The toughness and elongation at break of testing samples are increased by 70 % and 22 %, respectively under impact loading. Sample behaviour is changed at low deformation rates, displaying stable crack growth. However, bending modulus and yield strength are reduced by 50 % and 12 %, respectively. Hence, the total conservation of the initial properties of the matrix material remains a challenging task for the future. Additionally, suppression of the diffusion between the separate layers leads to the undesired harmonisation of the mechanical properties diminishing the toughening effect.

Kurzfassung

Stereolithographie ist die älteste 3D-Drucktechnik. und erlaubt den Druck von Bauteilen mit fast beliebiger Geometrie bei herausragender geometrischer Auflösungen und besonders dünnen Schichtdicken. Ein großer Nachteil dieser Technik ist, dass sie auf die Verarbeitung eines Materials zur gleichen Zeit beschränkt ist. Dieser Umstand wird in der vorliegenden Arbeit durch die Verwendung eines neuartigen hybriden 3D-Druckers verändert. Die Maschine vereint den konventionellen Stereolithographieprozess mit dem Tintenstrahldruck. Damit ist die Kombination von zwei unterschiedlichen Materialien, möglich.

Im ersten Teil dieser Arbeit wird der stereolithographische Prozess genauer analysiert. Dies geschieht durch die Herstellung und Testung unterschiedlicher mechanischer Prüfkörper. Das Ausgangsmaterial bildet ein Komposit, mit Monomeren und anorganischem Keramikpulver als Hauptbestandteilen. Mittels Prüfkörpern werden die wichtigsten mechanischen Eigenschaften und potentielle Anisotropie untersucht. Biege- und Bruchmechanikversuche ergeben Werte von 6000 MPa, 60 MPa, 2 % und 1,6 MPa* $m^{(1/2)}$ für Biegemodul, Biegefestigkeit, Bruchdehnung und Schlagzähigkeit. Es wurde kein Hinweis auf mechanische Anisotropie gefunden.

Der zweite Teil der Arbeit befasst sich mit der Anwendung des hybriden 3D Druckers mit unterschiedlichen Materialkombinationen. Ziel ist es, die Bruchzähigkeit von spröden Kompositwerkstoffen zu verbessern. Dies geschieht durch die Einbringung eines zweiten Materials mittels Tintenstrahldruck. Dadurch ist es möglich einen Werkstoff zu erzeugen, der aus Schichten periodisch wechselnden Materials besteht. Der „material inhomogeneity effect“, der von biologischen Organismen inspiriert ist und auf starke Unterschiede der mechanischen Eigenschaften innerhalb einer Struktur beruht, wird erfolgreich angewendet.

Der teilweise automatisierte hybrid 3D Druck erlaubt die Erzeugung von Prüfkörpern mit verbesserter Schlagzähigkeit und Bruchdehnung. Die Schlagzähigkeit und die Bruchdehnung bei hohen Deformationsraten konnten um 70 % und 22 % gesteigert werden. Das Materialverhalten bei niedrigen Deformationsraten änderte sich und zeigte stabile Rissausbreitung. Dennoch wurden Biegemodul und Streckgrenze um 50 % und 12 % verringert. Die vollständige Erhaltung der ursprünglichen mechanischen Eigenschaften des Kompositwerkstoffes stellt somit eine Herausforderung für die Zukunft dar. Außerdem muss die Diffusion zwischen den unterschiedlichen Materialschichten, die zu einer Angleichung der mechanischen Eigenschaften und somit zu einer Verringerung des Zähigkeitsgewinns führt, zukünftig unterdrückt werden.

List of Figures

Figure 1. Principle of AM: A 3D-object is generated via staggered layers. 4

Figure 2. Process chain of an AM part. 5

Figure 3. SLA process following the top-down approach. 6

Figure 4. 3D printing using DLP technology (a) [23]. Principle of DMD (b). 7

Figure 5. Schematic view of a CIJ system (top). Liquid jet collapsing into single droplets (bottom). 9

Figure 6. Schematic drawing of the actuation principle. 9

Figure 7. Schematic view of a DOD system (top). Single drop ejected from a nozzle (bottom). 10

Figure 8. Operation regime for inkjet printing in terms of *Re* and *Oh*. 12

Figure 9. Typical polymerisable molecule (a) and initiation stage (b). 13

Figure 10. Propagation of the radical chain polymerisation. 13

Figure 11. Termination of radical chain polymerisation via recombination of two active sites. 14

Figure 12. Termination of radical chain polymerisation via transfer of an H atom resulting in a deactivation. 14

Figure 13. Elastic modulus as a function of temperature. Operating area and thermomechanical behaviour for amorphous (top left) and semi-crystalline (top right) thermoplasts as well as elastomers (bottom left) and thermosets (bottom right). 16

Figure 14. Polymeric stabilisation mechanisms. Electrostatic stabilisation (top) and steric stabilisation (bottom). 19

Figure 15. Schemtic view of the different tensile test specimen designs and their behavior under loading. 22

Figure 16. Stress-strain curves of a brittle material (a), ductile materials with yield point (b,c), ductile material without yield point (d), and elastomeric material (e). 23

Figure 17. Impact of deformation rate ($\varepsilon_1 > \varepsilon_2 > \ldots > \varepsilon_6$) (a) and temperature (b) ($T_1 < T2 < \ldots < T_5$) on the material behavior a. 24

Figure 18. Standard bending test specimen and its relation to the tensile test specimen. 24

Figure 19. Bending tests in 3-point (a) and 4-point (b) configuration a. 25

Figure 20. Typical stress-strain curves for polymers in 3-point bending tests. Brittle fracture (a), ductile behaviour with yield point (b) and ductile behaviour without yield point. 26

Figure 21. Phase shift between stress and strain under driven oscillation in DMA. 27

Figure 22. Representation of the complex Young's modulus E^*. 27

Figure 23. Temperature dependent DMA yielding storage and loss modulus as well as T_g defined by the peak of the *tan δ* curve. 28

Figure 24. Time dependent deformation behavior (top) and the resulting indentation mark (bottom) of an elastic (a), viscoelastic (b) and plastic (c) material. 29

Figure 25. Set-up of theDynstat impact strength test. 31

Figure 26. A stiff and high strength material (red) and a weaker ductile material (blue) achieving the same amount of impact strength. 32

Figure 27. Shape and dimensions of the SENB. 33

Figure 28. Crack propagation at linear elastic conditions. . **Fehler! Textmarke nicht definiert.**

Figure 29. Stress modes at the tip of a crack with infinitely small crack tip radius. 36

Figure 30. Different sizes of the plastic zone around the crack tip, described as small-scale yielding (a), contained yielding (b), and fully developed plasticity (c). 37

Figure 31. Path independent J-Integral around the plastic zone (1) at the crack tip in the linear-elastic region. 38

Figure 32. Experimental determination of Jc. 39

Figure 33. After crack initiation, the crack with initiatl length a_n propagates through a brittle material resulting in fracture (a). Thin soft interlayers featuring low Young's modulus act as effective crack stoppers (b). Smaller distance between interlayers λ results in higher fracture strength of the specimen (c). 40

Figure 34. SEM images of the TCP poder used. Overview of particles (a) and higher magnification images of orange area (b) and red area (c). 46

Figure 35. Top view of the vat. The heating element contains a window for the exposure by the light source below. 49

Figure 36. Rotatable vat with the height adjustable coating knife attached. 49

Figure 37. Building platform consisting of a glass plate fixed to a metal mounting. 50

Figure 38. Building platform mounted to the printer. The rotatable vat is visible at the bottom side. 51

Figure 39.Workflow of the 3D-printing process. Main components of the 3D-printer (a). Top view of the building platform (b). Building platform with the attached layers is immersed into the vat (c). A layer is cured by UV light and attaches to the already existing layers (d). The platform is lifted (e). Vat surface is coated with fresh resin (f). 51

Figure 40. Illustration of the inkjet system. Yellow arrows indicate the direction of the ink flow. 54

Figure 41. Workflow of the hybrid printing system. (a) The building platform immerses into the vat and a layer is printed; (b) the building platform rotates upwards; (c) an inkjet layer is printed and fixated; (d) after rotating downwards, the ink layer is fully cured and the next resin layer is printed. 55
Figure 42. Illustration of the three orthogonal building directions 57
Figure 43. Cylinder for resin stability measurements. 58
Figure 44. Positioning of Vickers indentation marks fixed by diagonal length of indentations and distance to the specimen boundaries. The distance between two adjacent marks is bigger than 10*d. 61
Figure 45. Results of the TGA measurements. 62
Figure 46. Representative curve of 3-point bending test specimens for each respective group 62
Figure 47. Figure 6. Fracture surface of 3-point bending specimens in XYZ (a), YZX (b), and ZXY (c) direction. 63
Figure 48. Influence of the building directions on the fracture toughness K_{IC}. 64
Figure 49. Influence of the building direction on the toughness under impact loading. 64
Figure 50. Influence of building direction on bending modulus (a), bending strength (b), and elongation at break (c). 65
Figure 51. Influence of building directions on Vickers hardness. 66
Figure 52. Results of the DMA measurements. Storage moduli (continuous line) and tan δ (dashed line) for all three sample orientations. 66
Figure 53. Structural analysis of the skeleton of Euplectella Aspergillum. Entire skeleton (a). Regular structure of the cage structure (b). Single beam of the cage showing multiple spicules inside (c). Cross-section through a single spicule. Inorganic areas (dark) are divided by thin organic layers (bright) (d). Fractured spicule displaying an organic interlayer between silica regimes (e). 70
Figure 54. Dynstat impact strength test set-up for an unnotched sample (S) fixed between two thrust blocks (TB). The force applied by the hammer (H) is perpendicular to the orientation of the layers. 74
Figure 55. Dynstat impact strength tests show no differences between groups A and B and significantly higher values for group C. 76
Figure 56. Bending tests clearly show a reduction in Young's modulus for group C samples. 77
Figure 57. Bending tests yield a slight decrease in yield strength for group C samples. 77

Figure 58. Bending tests reveal a significant increase in elongation at break for group C samples. ... 78
Figure 59. Results of DMA measurements. Means of storage modulus (continuous) and *tan δ* (dashed) for sample of all groups. ... 81
Figure 60. Digital microscopy imaging of the cross sectional area. Samples from group A (a) and B (b) appear homogeneous. Separated resin and ink layers are visible in group C samples (c). ... 82
Figure 61. Coloured cross section of a group C sample. Ink layers (thin dark lines) are visible between brighter resin layers. ... 83
Figure 62. SEM image of a group C sample. Count rate for Ca equivalent to the Ca content in this region is decreased in the area of ink layers. ... 84
Figure 63. Schematic view of the 3-point bending test setup (dark objects symbolize rollers) with respect to the layer orientation (i.e., dark lines) of groups XT and XC (a) as well as YT and YC (b).. ... 90
Figure 64. Temperature profile of pure ink viscosity. ... 93
Figure 65. Force-displacement curves of SENB samples from all groups displaying significant differences prior to total failure. ... 94
Figure 66. Means and standard deviations of J fracture toughness for all groups. ... 95
Figure 67. LSM images showing fluorescent ink layers between dark resin layers for group XT (top) and YT (bottom). Scale bar is 200 µm. ... 96
Figure 68. SEM imaging of a YT sample. Ink layers appear as dark vertical lines. Scale bars are 20 µm (left) and 10 µm (right). ... 96
Figure 69. SEM imaging of a YT sample fracture surface in different magnifications. Ink layers appear as dark lines. ... 97
Figure 70. Analysation of the Young's modulus with z being the vertical direction of the sample with respect to printing direction. The marked region of low stiffness represents an ink layer. ... 98

List of Tables

Table 1. Main functions of polymer additives. 17
Table 2. Composition of the TCP I resin 41
Table 3. Composition of the TCP II resin 43
Table 4. Composition of the TCP III Resin 44
Table 5. Composition of the Cyano ink. 47
Table 6. Composition of the Tango ink. 47
Table 7. Printing parameters for TCP resins. 52
Table 8. Inkjet parameters for the different inks. 54
Table 9. Summarized results of the bending tests. 65
Table 10. Results of Shapiro-Wilk test and Levene test. * Significant difference (p= 0.05)... 67
Table 11. Results of the ANOVA and Welch-ANOVA (†) showing no significant differences (p=0.05). 68
Table 12. Comparison of homogeneous materials. 71
Table 13. Composition and printing systems used for each group. 72
Table 14. Sample dimensions and respective layer heights for all groups. 73
Table 15. Results of the bending tests. 76
Table 16. Results of Shapiro-Wilk test and Levene test. * Significant difference (p= 0.05)... 78
Table 17. Results of the ANOVA and Welch-ANOVA (†). * Significant differences (p=0.05). 79
Table 18. Results from the Bonferroni post-hoc test specifying the differences between the groups. 79
Table 19. Labelling, building direction, and composition of all groups. 88
Table 20. Number of layers and layer thickness for all groups. 88
Table 21. Assessed mechanical parameters for all groups. 95

List of Abbreviations

ANOVA	Analysis of variances
BAPO	Phenylbis (2,4,6-trimethylbenzoyl)-phosphine oxide
CAD	Computer aided design
CIJ	Continuous inkjet
DLP	Digital light processing
DMA	Dynamical mechanical analysis
DMD	Digital mirror device
DOD	Drop on demand
DPI	dots per inch
DW	Drop watcher
LED	Light emitting diode
PI	Photoinitiator
SEM	Scanning electron microscope
SENB	Single edged notched bending
SLA	Stereolithography
STL	Standard tessellation language
TCP	Tricalcium phosphate
TGA	Thermogravimetric analysis
TIJ	Thermal inkjet
TPO-L	(2,4,6-trimethylbenzoyl)-phenylethoxyphosphine oxide

1 Introduction and Motivation

Today, numerous 3D printing techniques are available and used in industrial applications. This technology developed from its original research based focus to a reliable manufacturing process used in various fields like aviation [1], automotive industry [2], and the medical sector [3]. Via the adaptation of the manufacturing processes, some 3D printing techniques allow large-scale production [4], [5]. In order to establish and justify their position in various application areas, 3D printing technologies have to challenge the traditionally used manufacturing techniques (e.g., injection moulding, casting, forging).

Besides the production capabilities, the final properties of the produced parts play a key role in the comparison between 3D printed and conventionally used manufacturing techniques. One of the big advantages of additive manufacturing is that the final properties of the produced samples are determined during the printing process. This renders the field of 3D printing very interdisciplinary. Expertise in the fields of engineering, physics, and chemistry is required to assemble an optimal production process resulting in the best possible material properties. Consequently, the 3D printer and the materials processed must be matched to yield the desired results.

Stereolithography (SLA) is the oldest 3D printing technology. It allows exceptional spatial resolution and high quality surface finishes. Additionally, almost arbitrary geometries are feasible with this process. One of the main application areas is the processing of polymeric substances [6]–[8]. Polymer parts produced by SLA 3D printing are currently used in dentistry [9], cell culture [10], or in the electronic industry [11]. The versatility arises from the fact that a multitude of monomer combinations is possible. Additionally, material properties can be adapted by adding particles to the liquid resin.

One major drawback of conventional SLA is that the process is limited to a single liquid material. This limits the available material spectrum in comparison to other AM technologies (e.g. inkjet printing).

In this work, SLA technique is used to produce parts by means of light induced radical chain polymerisation (i.e., photopolymerisation). The monomers and oligomers are acrylate and methacrylate based and very well suited for this particular polymerisation technique. Samples created in this manner typically feature high stiffness and strength but lack sufficient fracture toughness [12]. Increasing the toughness of photopolymers is a challenging task which is usually tackled by adding toughening agents to the raw material or manipulating the polymerisation process [12], [13]. This procedure often leads to a deterioration of the initial properties of the material.

To circumvent this problem a radically new approach is taken. A hybrid printing system allowing the connection of conventional SLA technique with inkjet printing is used to adapt the properties of the printed samples. The general applicability of this new printing technique is tested and the toughening possibilities are sounded out.

2 Fundamentals

In this chapter an overview of manufacturing technologies in general and additive manufacturing in particular is given. The 3D printing techniques used in this work, namely SLA and Digital light processing (DLP) technology as well as inkjet printing are described in detail focusing on both the building process itself as well as the fundamental physical principals. Since all raw materials used are based on photopolymerisation, a brief introduction to the chemical reactions occurring during the manufacturing is given. Furthermore, a brief description of typical additives for photopolymers is given. Thereafter, the theoretical foundation of the thermomechanical tests utilised in this work is given.

2.1 Manufacturing technologies

Manufacturing techniques can be categorised with regard to the geometry of the processed sample. Three fundamentally different categories can be distinguished:

1. formative manufacturing techniques
2. subtractive manufacturing techniques
3. additive manufacturing techniques

Formative manufacturing is characterised by constant part volume during the building process. External forces (e.g. bending, forging, and casting) as well as heat can be applied to alter the geometry of the building part.

Subtractive manufacturing methods remove material from the surface of the raw part to derive the desired shape (e.g. milling, turning). The removal is achieved by contact with tools and produces chips [14].

Additive manufacturing (AM) builds the desired geometry via the addition of single material layers onto each other. These layers are unified to gain the final part without the usage of specialised tooling and apparatus [15]. Thus, this manufacturing category is also called layer-based technology. It is fundamentally based on the idea that any 3-dimensional body can be sliced into thin layers. Hence, arbitrary geometries can be created by the continuous addition of material layers. In contrast to the aforementioned techniques, a block of raw material is not required to produce the desired geometry [14]. The principle of AM is displayed in Figure 1.

Figure 1. Principle of AM: A 3D-object is generated via staggered layers. [16]

2.2 Additive manufacturing

The foundation of additive manufacturing lies in the development of the SLA process invented in 1984 [17]. Today, additive manufacturing, rapid prototyping, solid freeform fabrication, 3D printing, and other similar terms are used synonymously [14]. Although this unification is not fully justifiable (e.g., 3D printing is a particular additive manufacturing method), all of these terms describe the formation of a building part in a layer-wise process. In recent years, the generic term 3D printing has frequently replaced all other terms because it is easily understood and appeals to a wider user group [18]. Hence, all techniques relying on the building of samples layer by layer will be subsumed under the term 3D printing. 3D printing involves a number of steps in a process chain, starting with a virtual computer model of the desired geometry and ending with the physical building part. The individual production segments of the building process can be separated into three main phases.

The pre-process including all operations in the virtual realm. The starting point is a model created by computer-aided design (CAD) software. The CAD model can arise either from manual drawings or from imaging techniques (e.g., computer tomography) of already existing parts [14]. This model includes all information about the part geometry and potential support structures depending on the shape of the printed object. Thereafter, the virtual model is conversed into the surface tessellation language (STL) file format. This system independent format contains the external closed surfaces and is a de facto standard for all printed parts [14]. STL is the most widely used format in 3D printing. However, this format fails to represent properties such as colour and material used. Other formats including further information are therefore available (e.g. additive manufacturing file format, object format, virtual reality modelling language, polygon file format) [18], [19].

The in-process is described by the actual building of the part via continuous addition of material layers in the machine. The 3D printers usually work autonomously compiling the information from the computer files.

The post-process includes all necessary production steps after the building of the part. These include the removal of the printed sample from the build platform and the cleaning of the sample from residues by (thermo-) mechanical means (e.g. heat, compressed air, tissues). Potential support structures, which might be necessary for printing overhangs, are removed in this step. Depending on the AM technique and the used material, final part properties are achieved in this phase by means of post building treatment (e.g., exposer to UV-light, sintering). The process steps from the virtual CAD model to the physical part are displayed in Figure 2.

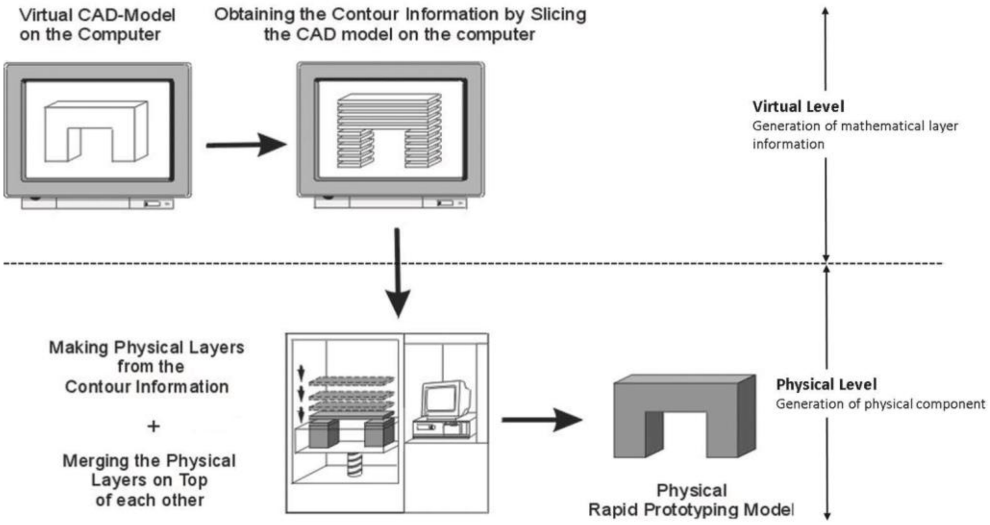

Figure 2. Process chain of an AM part [18].

Although numerous 3D printing techniques exist, only those relevant for the understanding of this work will be described in the following.

2.2.1 Stereolithography

SLA is based on the solidification of a liquid via the means of light induced polymerisation (i.e. photopolymerisation). The liquid resembling the basic material usually consists of a blend of monomers, at least one photoinitiator to trigger the polymerisation process and potentially additives (e.g., fillers, absorber). The raw material is located inside a material vat. A moving laser spot scans over the liquid solidifying the desired shape. The solidified layer adheres to the building platform which can either be immersed from the top or from the bottom (i.e., top-down and bottom-up approach). Although both approaches are utilised the top-down is advantageous to the bottom-up because of the confined light source, easier recoating, and a smother surface [20]. Recoating of the material vat is done either by means of gravity in case of sufficiently low viscosity or with a coating knife. The principle of SLA with a top-down approach is displayed in Figure 3.

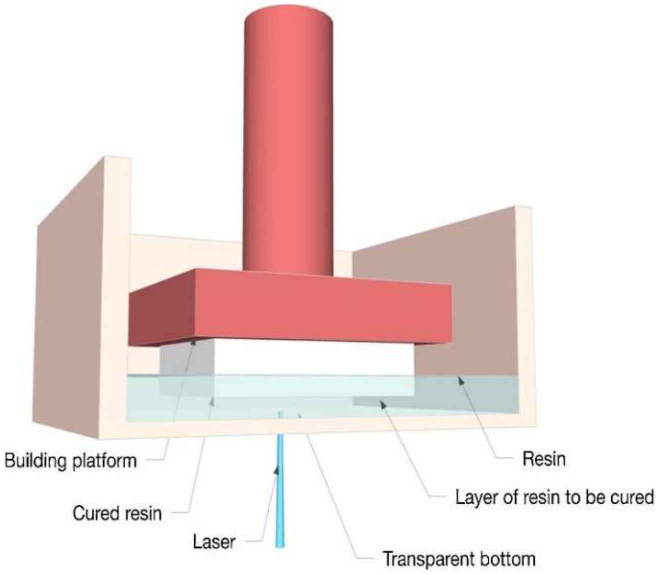

Figure 3. SLA process following the top-down approach [8].

2.2.2 Digital Light Processing

DLP is closely connected to the SLA process. Similar to SLA, this technique utilises light to trigger polymerisation and consequently solidification of a photopolymerisable resin. In contrast to SLA technology where a single laser beam moves along the surface to cure the liquid, DLP systems operate with a dynamic mask based on a digital mirror device (DMD) [21]. The DMD is located in the optical path of the light source (i.e., light emitting diode) and consists of numerous small mirrors, each one movable between two positions. A single mirror represents a distinct pixel on the building field. Depending on their position, these mirrors either reflect the incoming light towards the building field or towards a light trap. Hence, exposure of each pixel of the building field can be controlled individually by switching the mirror position. This technique allows full curing of a layer at the same time, thus drastically decreasing the building time compared to conventional SLA [22]. The projector determines the possible resolution via the fixed number of available pixels which is independent of the build area. Consequently, the achieved surface quality decreases with increasing sample size because a bigger curing area needs to be covered by the same amount of pixels. The principle of DLP technique and the fundamental functionality of the DMD assembled in DLP systems are displayed in Figure 4.

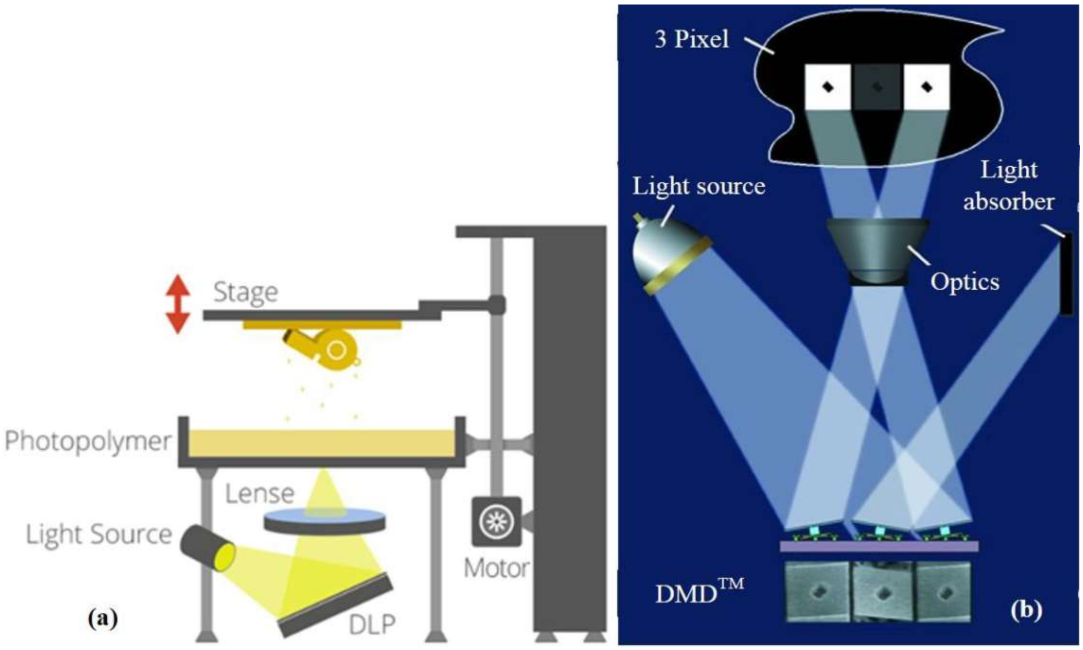

Figure 4. 3D printing using DLP technology (a) [23]. Principle of DMD (b), adapted from [24].

2.2.3 Inkjet Printing

Inkjet printing has evolved from conventional printing methods (e.g., flexography, lithography, screen-printing), which have been used and adapted over centuries to print newspapers, food packages, or textiles. All these conventional printing methods share a specific feature, that is a physical machine part (e.g., roll, plate) is utilised to transfer the pattern to be printed onto the substrate. Thus, alternation of the final printing pattern includes changing of the physical master pattern inside the printing machine. In contrast to all conventional printing techniques, inkjet printing omits the aforementioned physical printing masks and creates the desired shape by directly placing ink droplets on the substrate [25]. The deposition of ink drops, which usually feature a diameter between 10 µm-100 µm is managed by digital data files. Thus, the printed pattern can easily be changed between printing processes and even within the same production cycle by exchanging the source file.

In recent years, inkjet printing technique is applied in advanced areas such as 3D printing. A 3-dimensional structure can be created by jetting the ink onto a powder bed or jetting a photopolymer which is subsequently cured [26]. Assuming correct rheological properties, inks containing polymers, biomaterials, and ceramic as well as metallic suspensions are processible [27]. In combination with the advancements in print head technology, the development of sophisticated inks opens a wide range of applications in 3D printing [28]. Inkjet printing systems can be roughly distinguished by the method of droplet formation. Two different modes, namely continuous inkjet (CIJ) and drop on demand (DOD) are present in the field of inkjet printing [29].

2.2.3.1 Drop formation

In both modes, the ink is ejected through a nozzle towards the area to be printed. In CIJ printing the material emerges as a stream of ink from the nozzle. This stream is inherently unstable and breaks up into numerous droplets. This behaviour originates from the Plateau–Rayleigh instability where a liquid column always breaks up into spherical droplets to achieve minimization of the surface energy [30], [31]. This phenomenon is utilised to manipulate the individual droplets by means of electric force. Electrostatic force is used to alternate the flight path of the ink droplets. This allows the deliberate application of ink onto the desired spot of the substrate [32]. Since the amount of ink required for the CIJ process is substantially higher than in DOD printing, only some droplets are deflected by the electrostatic field while the remaining ink is collected in a reservoir and recycled back to the nozzle [33]. Single or multi-nozzle configurations are available. Printing of different locations on the substrate is achieved either through deliberate focus of the ink stream or by moving the substrate under the nozzle. The working-flow of a CIJ printing system is displayed in Figure 5.

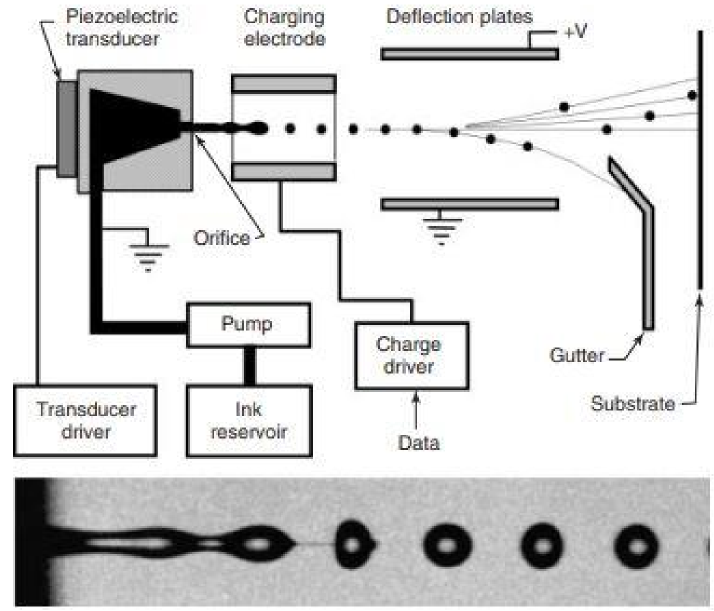

Figure 5. Schematic view of a CIJ system (top). Liquid jet collapsing into single droplets (bottom) [34].

In DOD printing, pressure pulses are used to eject a drop from the nozzle. Two different approaches of creating this pressure wave can be characterised. In the first and more common one, piezoelectric ceramic elements are deformed by means of changing electric currents and thus ink is pushed through the nozzle channel towards the orifice. An electric voltage on a piezo actuator changes the diameter of the ink channel and thus generates pressure. By reflection on the reservoir side of the channel this pressure wave gets enhanced and amplified by a second pulse resulting in a large pressure peak at the nozzle, which ejects a droplet [35]. The wave generation via a piezo actuator is shown in Figure 6.

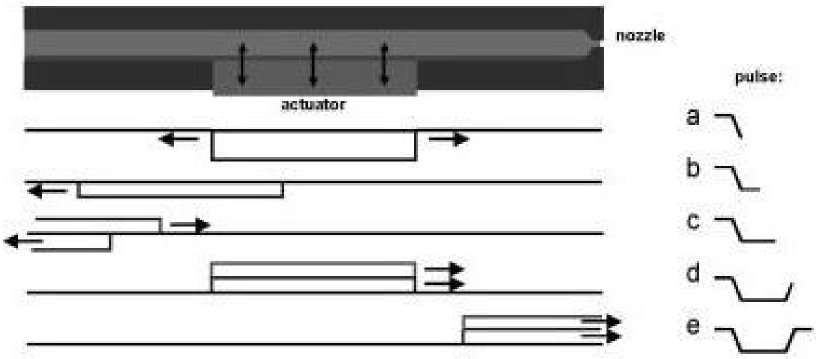

Figure 6. Schematic drawing of the actuation principle [35].

The second method uses thermal energy in a heating element to create small vapour bubbles in the liquid that push the ink towards the nozzle opening (i.e., Thermal Inkjet, TIJ) [34]. Although the majority of all DOD printers are based on TIJ (e.g., desktop printer), this method is not suited for all materials. The vapour bubble necessary for the ejection process is created by directly heating the ink in the nozzle. Thus, some parts of the liquid material need to boil, which can, depending on the raw material of the ink, permanently change the ink properties [36]. Hence, for 3D printing purposes, DOD systems based on piezoelectric elements are preferred. In contrast to CIJ systems, the ejection direction of nozzles cannot be alternated. Thus, DOD print heads consist of numerous nozzles, which can be triggered individually to selectively print the substrate resulting in very precise droplet placement [37]. Generally, DOD technology allows smaller droplet sizes in the range of picoliters compared to CIJ and requires less raw material [38]. A DOD printing system based on piezoelectric elements is depicted schematically in Figure 7.

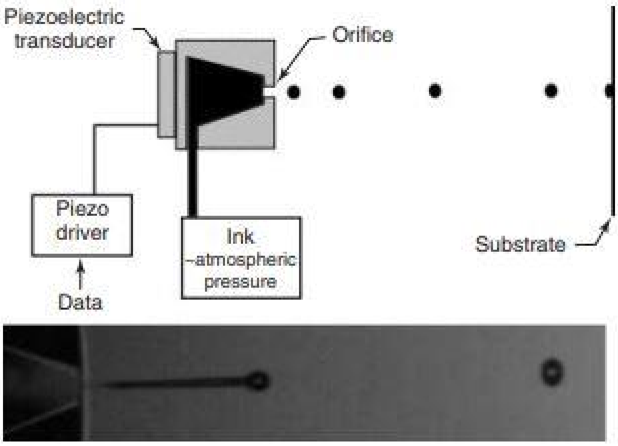

Figure 7. Schematic view of a DOD system (top). Single drop ejected from a nozzle (bottom) [34].

2.2.3.2 Ink parameters

The two physical properties dominant for the behaviour of the liquid ink inside the printing system and the generation of the drops are surface tension and dynamic viscosity [29]. The surface tension, denoted with γ, reflects the fact that liquids form a specific geometrical shape to minimize their surface energy. For a free droplet not in contact with any other surface, that is a sphere. This tendency of a free liquid to form spheres is responsible for the generation of single drops in CIJ printing as well as the main drop and potential satellite drops in DOD systems [39, S.].

The dynamic viscosity, denoted with η, is the proportionality factor between the shear stress τ and the shear velocity $\dot{\gamma}$:

$$\tau = \eta\dot{\gamma} \tag{I}$$

If η is independent of $\dot{\gamma}$ then the liquid behaviour is called Newtonian.

These two for the inkjet process fundamental variables are included in two factors (i.e., Reynolds number *Re* and Weber Number *We*) representing the ratio between inertial forces (i.e., density ρ, velocity v, and characteristic length *d*) and viscosity as well as surface tension, respectively:

$$Re = \frac{\rho v d}{\eta} \tag{II}$$

$$We = \frac{\rho v d}{\gamma} \tag{III}$$

These two factors can be combined to form a dimensionless variable, called the Ohnesorge number *Oh*

$$Oh = \frac{\sqrt{We}}{Re} \frac{\eta}{\sqrt{\gamma\rho d}}, \tag{IV}$$

where *d* is the characteristic length equal to the diameter of the nozzle and ρ is den density of the fluid. *Oh* solely takes the physical properties of the liquid into account ink while driving parameters (e.g., drop velocity) are omitted. Nevertheless, this parameter is closely related to the drop behaviour and represents boundaries for the printability of an ink [40]. In case of high values of *Oh* high viscosity will prevent drop formation, while too small values might result in a large number of undesired satellite drops [41]. This leads to the rule of thumb

$$0{,}1 < Oh < 1, \tag{V}$$

which will result in a printable ink when combined with satisfying machine parameters (e.g., piezo crystal firing rate in DOD). The operating regime for inks is depicted in Figure 8.

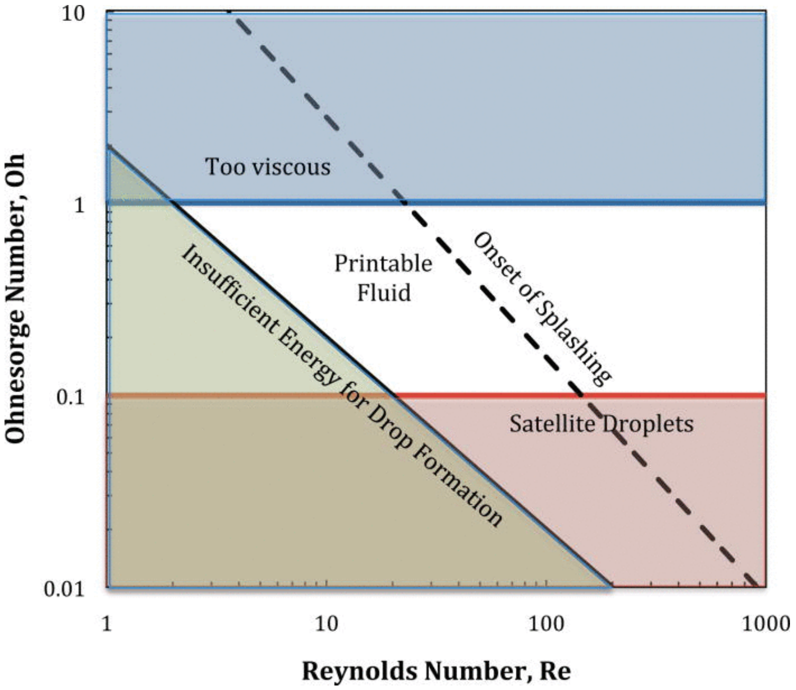

Figure 8. Operation regime for inkjet printing in terms of *Re* and *Oh* [42].

However, depending on the constituents of the ink (e.g., fillers, suspensions, polymeric, metallic elements) the printability range of *Oh* can differ substantially [40], [43].

2.3 Photopolymers

A photopolymer is any species that undergoes a direct or indirect interaction with light to alter its physical or chemical properties [44]. They consist of monomers, oligomers, polymers, or combination of these as well as a photoinitiator (PI). These systems undergo polymerisation when exposed to a light source with a suited wavelength. Light induced polymerisation is feasible at room temperature and offers high spatial resolution (i.e., polymerisation reaction is constricted to exposed areas) and is therefore fit for the 3D printing of polymer-based parts [45]. There are various forms of polymerisations (e.g., chain growth, step growth) as well as sub-categories (e.g., free radical, cationic, anionic). However, only the reaction mechanism relevant for this work will be covered in the following.

2.3.1 Free radical chain polymerisation

Free radical chain polymerisation is the most commonly used method of chain polymerisations and can be divided into the three basic stages, namely initiation, propagation, and termination. The initiation involves the creation of a free radical by decay of an initiator. In case of photopolymers, this substance is the PI, which forms free radicals when exposed to an appropriate light source. The free radical reacts with a suitable monomer by adding to the C=C double bond of that monomer leading to an active site at the monomer (i.e., the monomer features a free valence electron) [46]. This further implies that not all monomers are suitable for radical chain polymerisation. The general structure of a monomer which polymerises radically as well as the initiation process are depicted in Figure 9.

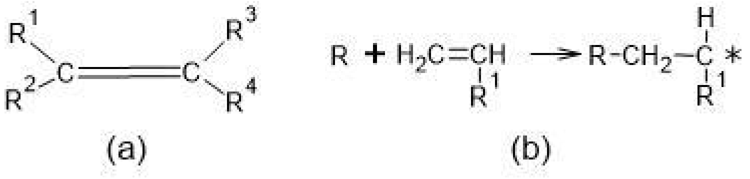

Figure 9. Typical polymerisable molecule (a) and initiation stage (b), adapted from [46]

The propagation stage starts when this particular monomer now bonds to another monomer, forming a polymer chain while transferring the active site to the next monomer. Hence, the newly formed polymer chain reacts with another monomer adding to its length and transferring the radical further (see Figure 10). Depending on the functionality of the monomers (i.e., number of potentially reactive C=C bonds) the macromolecular structure differs significantly. Polymerisation of monomers with few functional groups leads to long polymer chains with a low amount of cross-links between them. On the contrary, polymerisation of high functionality monomers result in a highly cross-linked polymer network [13]. This propagation continues until no more monomers are available or the chain growth is terminated.

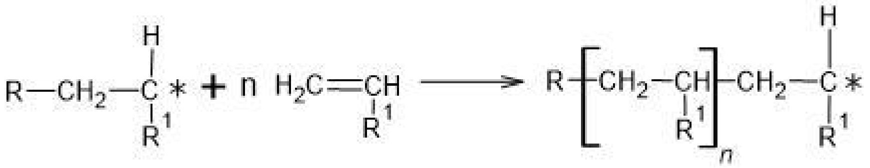

Figure 10. Propagation of the radical chain polymerisation [46].

The termination of the polymerisation process occurs by either recombination or disproportionation. Recombination takes place when two active sites of polymer chains react with each other to form a stable macromolecule. Disproportionation means the transfer of a hydrogen atom from one chain to another to form two non-reactive molecules [47]. Both reactions are depicted in Figure 11and Figure 12 respectively.

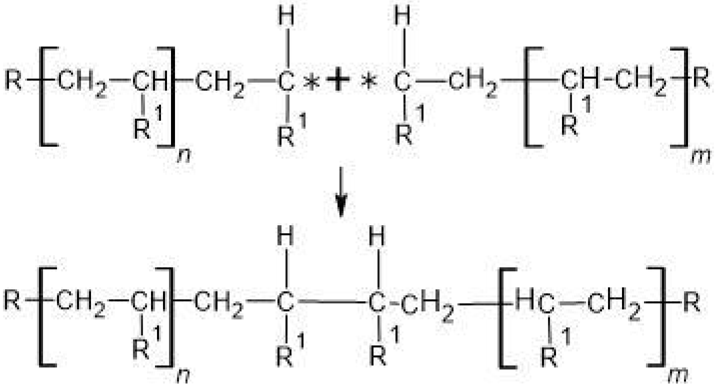

Figure 11. Termination of radical chain polymerisation via recombination of two active sites [46].

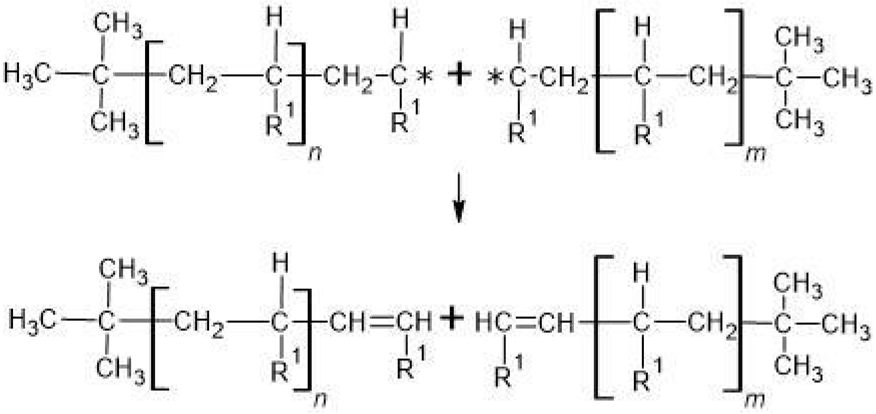

Figure 12. Termination of radical chain polymerisation via transfer of an H atom resulting in a deactivation [46].

The total length of polymer chains derived from radical chain polymerisation can therefore be adjusted to some extent. Nevertheless the length is limited due to wanted and unwanted (e.g., oxidation of free radicals) termination processes. This results in a certain amount of unreacted monomers remaining present in the polymerised structure. These substances represent undesired residues causing alteration in material properties via unwanted reactions after the polymerisation process (e.g., degradation of mechanical properties). Moreover, these residues are often toxic and thus limit biological and medical applications.

2.3.2 Classification of photopolymers

Polymers can be classified by their structure and morphology. This results in three categories of polymers with partially overlapping properties. These include thermoplasts, thermosets, and elastomers [48].

Thermoplasts consist of long polymer chains, which have no permanent chemical bonds to their neighbours. Between individual polymer chains only weak physical bonds are present. They exhibit either a distinct spatial orientation or a random distribution (i.e., amorphous or crystalline phase). Full crystallinity is only theoretically achievable. Consequently, thermoplasts are either amorphous or semi-crystalline with ordered chains building crystalline areas are embedded in amorphous regions. These polymers can be melted, shaped, and reshaped by temperature application without deterioration of the material properties. They are swellable and dissolve in proper solvents.

The long polymer chains of elastomers are loosely cross-linked resulting in a wide-meshed polymer network. These covalent bonds allow high mobility of the network resulting in the characteristic properties of this class. These include rubber elasticity, high elongation at break, and low strength [49].

Thermosets consist of polymer chains, which form a tight network. This network is built by a high amount of irreversible bonds between those polymer chains resulting in high crosslinking between the chains. The tight network is responsible for the material properties of thermosets, which are in many regards opposite to those of elastomers (e.g., high stiffness and strength). On the other hand, thermosets are brittle with and prone to fracture due to crack propagation. They cannot be melted or remodelled by heat treatment but exhibit high stability against solvents and temperature. Instead, excessive heat treatment will destroy the network permanently resulting in the disintegration of the material [49].

The structural differences between the groups result in strongly varying thermomechanical behaviour. As a result the application areas with respect to the temperature and particularly the glass transition temperature T_g differ significantly. Figure 13 shows the application range of the four polymer classes schematically.

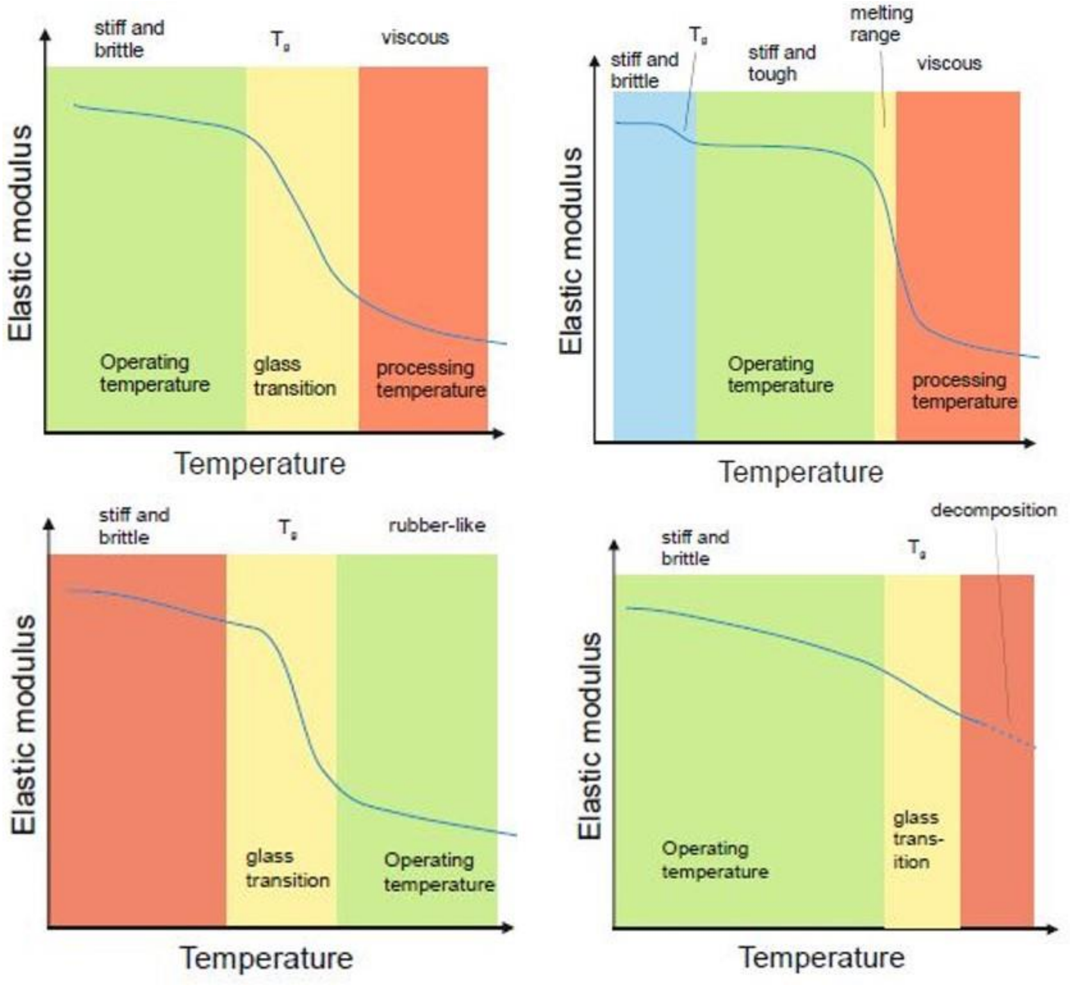

Figure 13. Elastic modulus as a function of temperature. Operating area and thermomechanical behaviour for amorphous (top left) and semi-crystalline (top right) thermoplasts as well as elastomers (bottom left) and thermosets (bottom right) [50].

Although there are approaches to mix different types of polymers together and add additives (e.g., rubber particles) to modify the final material properties, photopolymers are predominantly classified as thermosets [13], [51]–[53].

2.3.3 Additives

The usage of additives in the polymer industry has widened the range of applications for plastic materials significantly. Additives are incorporated substances, to achieve a technical effect in the production process or finished polymer part. They can be classified by their performance, that is clustered into groups with similar functionalities. Table 1 gives an overview of the most important groups of additives as well as some examples for each group.

Table 1. Main functions of polymer additives, adapted from [54].

Group	**Examples**
Polymerisation modification	Chain growth regulators, cross-linking agents
Improvement in processability	Defoaming agents, thixotropic agents, surfactants, dispersing agents, lubricants
Degradation resistance	UV stabilisers, thermal stabilisers, metal deactivators
Modification of mechanical properties	Impact modifiers, fillers and particle reinforcements, fibres
Improvement of surface properties	Adhesion promoters, antiwear additives, wetting agents, antistatic agents
Improvement of optical properties	Pigments, dyes
Reduction of formulation cost	Diluents, particle fillers

The mixing of the base polymers with the respective additives is called compounding. The result is a system (i.e., blend) with the desired final properties. Beside from homogeneity of the formulation to guarantee uniform properties in the entire batch, stability of all components during the mixing process is required. This includes thermal as well as mechanical stability. During the mixing process, increased temperature and high shear rates might lead to the selective degradation of additive components. Consequently, the quality of the final product is impacted by variations of compound quality [55]. Thus, the manufacturing of the polymeric compound is a complex procedure, which needs extensive monitoring.

In the following sections, additive classes and their functioning relevant for this work are described in detail.

2.3.3.1 Dispersing agents

The dispersion of a powder in a liquid is a two-step process. First, bigger groups of particles (i.e., aggregates and agglomerates) are separated into small units. Second, the resulting dispersion must be stabilised against aggregation (i.e., agglomeration of singular powder particles). The first step is achieved by application of mechanical energy. High-speed mixers producing high shear rates via turbulent flow in the resin represent an efficient way to disperse agglomerates and aggregates [56]. However, high particle content increasing extensive heat generation must be avoided to prohibit additive degradation. During the dispersing process, the individual particles are coated with the dispersing agent. Thus, the dispersant forms a thin coating around the particles enabling the stabilisation of the system by two different mechanisms, that is electrostatic stabilisation and steric stabilizstion. Both mechanisms can be combined in a single compound and serve the purpose of preventing particle agglomeration and aggregation by building repulsive forces between them [57].

In electrostatic stabilisation, the dispersant builds an electrical double layer around the particles. This double layer consists of a charge on the pigment surface and an oppositely charged cloud of ions around it. The electrical double layer has identical charge distribution for each particle. Thus, the charge cloud impedes particle agglomeration by repulsive electrical forces. Electrostatic stabilisation is particularly effective in water or other media of reasonably high dielectric constant [58].

Steric stabilisation fundaments on the adsorption of polymer chains on the particle surface. Polymer chains with similar conformity coat each particle forming an envelope. When two particles approximate each other, the polymeric envelopes overlap. In this zone, the polymer concentration is increased resulting in an osmotic pressure, which causes liquid material to be transported to this area. Thus, the two particles are separated by the liquid flow. Additionally, polymeric chain overlapping restricts the molecules resulting in the reduction of the entropy of the system. Hence, this represents an unfavourable state and the system changes to maximise the entropy by repulsion of the particles. Steric stabilisation is particularly effective in organic solvents and plasticizers featuring low dielectric constant [59]. Both stabilisation mechanisms are displayed schematically in Figure 14.

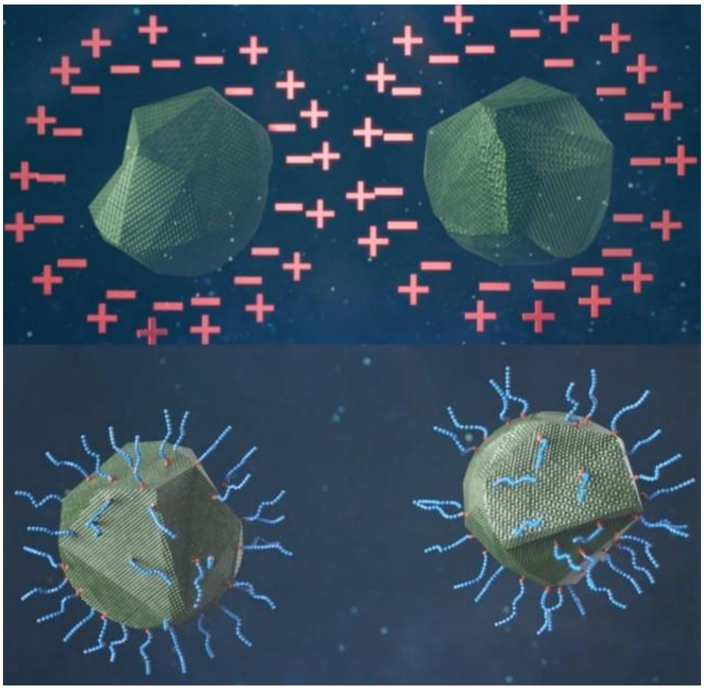

Figure 14. Polymeric stabilisation mechanisms. Electrostatic stabilisation (top) and steric stabilisation (bottom) [58].

2.3.3.2 Rheology additive

In order to grant long-term stability to a dispersed system it is essential to balance the effect of sedimentation. Sedimentation is a potential result of gravitational forces acting on all particles in a suspension. The particles move randomly through the liquid medium due to their Brownian motion. Adsorbed dispersants prohibit agglomeration and aggregation. However, when gravitational forces exceed the thermal motion of individual particles all particles start to sediment to the bottom of the system. Thus, sedimentation leads to a gradient in filler content in the medium, ultimately producing a compact sediment, so called “clay” [56]. The sediment formation must be prevented by adapting the liquid phase. The most common technique to prevent sedimentation is the application of “thickeners”. Through the addition of these polymeric substances, the viscosity of the liquid medium can be modified for distinct regimes. In low stress regimes, typically generated by the slow movement of the particles, the viscosity is increased drastically. A gel type system is formed which effectively prevents particle sedimentation. At high stresses (e.g., mixing), the system shows shear-thinning behaviour resulting in a significant reduction of viscosity [60]. Thus, good workability is guaranteed.

2.3.3.3 Colouring agents

Naturally, light including all wavelengths of the visible spectrum appears white to the human eye. Colouring agents function by selectively absorbing distinct wavelengths from the whole spectrum of light and consequently removing them from the human perception. Hence, deliberate absorption of wavelengths allows the specific colouring of an area [61]. Dyes are chemical compounds colouring selected areas or the entirety of the applied field. In the regime of polymers, these chemical structures dissolve in the matrix and are thus not present as discrete particles. Pigments on the other hand are discrete particulate materials, which cannot be dissolved in the polymer matrix. After the polymerisation process, they remain as particles with grain sizes ranging from 1 nm to 40 µm and bigger in the matrix [62], [63]. Thus, these additives can agglomerate, are prone to sedimentation like other particles, and require a more sophisticated handling than dyes. However, compared to dyes, pigments exhibit good thermal stability, higher resistance to bleaching, and higher brightness [55]. Therefore, the colouring is more stable and maintained over a longer timeframe.

2.3.3.4 Photoinitiators

Photopolymerisation is fundamentally based on the presence of substances inducing the curing of the material. These photoinitiators perform in various ways. Although different polymerisation techniques and thus different categories of photoinitiators exist, only those relevant for radical chain polymerisation are explained in the following.

Through the absorption of a photon (i.e., light irradiation), the production of radicals is initiated. Based on the type of reaction occurring, two different types of photoinitiators (i.e., PI type I and PI type II) [64]. Type I photoinitiators directly produce radicals by decay induced by the proper light source. Type II photoinitiators abstract a hydrogen atom from another molecule generating two radicals which start the reaction. The absorption range of a photoinitiator determines its area of application [65].

2.3.3.5 Fillers

Fillers are organic or inorganic substances, which can be mixed into the polymer batch to achieve various effects. The combination of polymers with different types of fillers allows the production of a wide range of materials (e.g., composites, sintered ceramics, and metal-polymer parts) [66]–[68]. Most importantly, inorganic powders are included to improve the mechanical properties of the polymerised part. Improving the strength and stiffness as well as the hardness of a polymeric material is thus possible. Moreover, resistance to heat as well as creep can be improved and electrical as well as thermal conductivity may be adapted [69]. Depending on the quality of filler materials and the polymeric components, fillers can act as a basic filling material solely for the purpose of lower production costs. Fillers must be suspended homogeneously in the liquid to ensure uniform particle distribution in the polymerised matrix. Additionally, agglomeration and re-agglomeration as well as sedimentation of filler particles must be prohibited because particle accumulations can act as defects deteriorating the properties of the matrix [70].

2.4 Thermo-mechanical testing

In this section, the methodology of all tests relevant for this work as well as their theoretical fundaments are described.

2.4.1 Tensile test

The tensile test is the most commonly used quasi-static measurement and represents the fundament for the examination of mechanical properties. Since a specific standard for polymer parts manufactured by 3D printing does not exist, the relevant information is obtained from DIN EN ISO 527. This standard covers a wide range of plastics and processing techniques (e.g., thermoplasts, thermosets, and fibre reinforced polymers) [71]. This test is based on the unidirectional tensile loading of shouldered specimens with a gauge section in the middle area. The two different designs available are displayed in Figure 15.

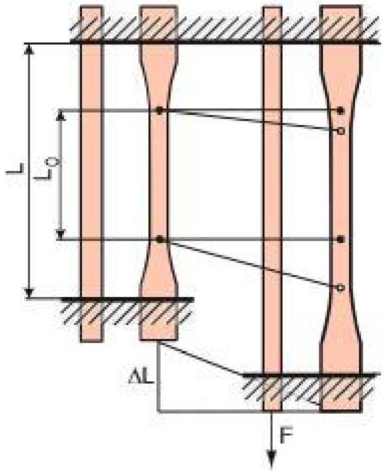

Figure 15. Schemtic view of the different tensile test specimen designs and their behavior under loading [72].

The basic measurement parameters include the loading *F* and the height adjustment of the lifting beam *ΔL*. In combination with the original cross-section of the specimen A_0, the nominal stress σ, and the strain ε are evaluated:

$$\sigma = \frac{F}{A_0} \tag{VI}$$

$$\varepsilon = \frac{\Delta \mathrm{L}}{\mathrm{L}} * 100\% \tag{VII}$$

In real polymer specimens, the cross-sectional area is reduced during the testing procedure due to lateral contraction. After the yield point. this necking effect leads to a significant reduction of the actual cross-section [73]. Hence, the shape of the curve achieved from (VI) does not resemble the true course. In order to gain insight about the true stress during the measurement strain gauges have to be applied to the specimen to continuously measure the change in width.

Polymers show a wide range of characteristics under loading depending on the material. Different typical stress-strain curves as well as the most important parameters for the characterisation are displayed in Figure 16.

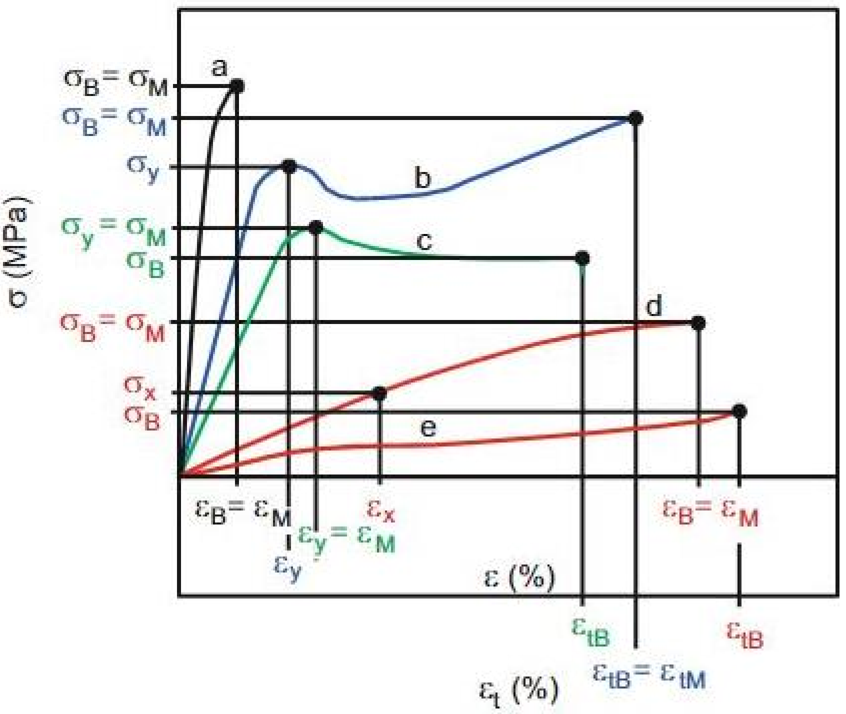

Figure 16. Stress-strain curves of a brittle material (a), ductile materials with yield point (b,c), ductile material without yield point (d), and elastomeric material (e) [72].

The most important parameters include the ultimate stress σ_B at the point of fracture, the tensile strength σ_m representing the maximum value over the course of the measurement, and the yield strength σ_y. Depending on the material, two or more of these values can be identical. The respective elongation values yield the correspondent parameters (e.g., elongation at break). Ductile materials with distinct yield point and necking area show significantly higher values of Young's modulus than those lacking these properties. For the exact measurement of the Young's modulus (i.e., slope of the curve in the linear-elastic region), an additional extensometer is required.

Apart from the material, polymeric behaviour strongly depends on the deformation rate as well as the ambient temperature, that is polymers display viscoelastic behaviour [74]. The results as well as the overall characteristics can change drastically with changing examination parameters. Hence, the deformation rate as well as the temperature and the humidity should be kept constant for all tests to ensure comparable results. The alteration in specimen behaviour in dependence of deformation rate and temperature is displayed schematically in Figure 17.

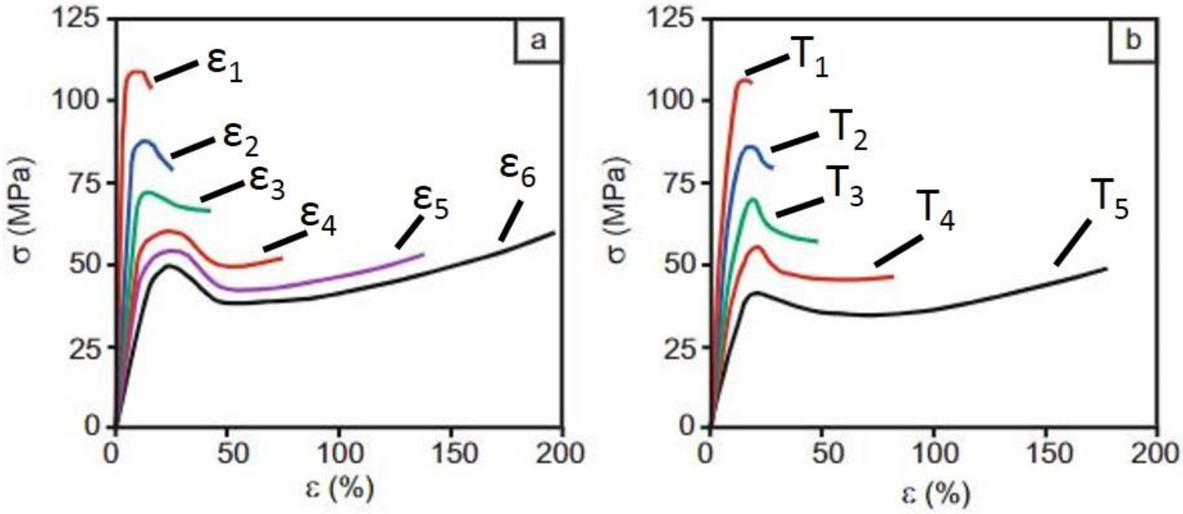

Figure 17. Impact of deformation rate ($\varepsilon_1 > \varepsilon_2 > \ldots > \varepsilon_6$) (a) and temperature (b) ($T_1 <$ T2 $< \ldots < T_5$) on the material behavior adapted from [72].

2.4.2 Bending test

Although the tensile test is the most frequently used testing method, pure tensile loading is rare in real-world scenarios. In industrial applications, parts are very often under the influence of bending loads. Thus, characteristic mechanical values obtained by bending tests are of great importance for specific implementations. In the realm of plastics, the quasi-static bending test according to DIN EN ISO 178 is commonly used to test stiff and brittle materials (e.g., filled thermoplasts, thermosets) [75].

The standard testing specimen is closely related to the standardized tensile test specimen and can be obtained by cutting of the shouldered part (see Figure 18).

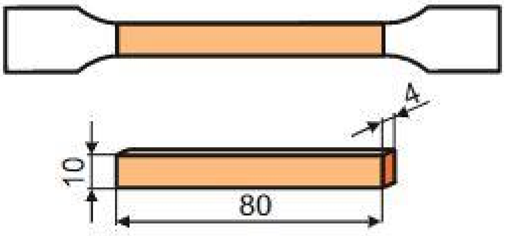

Figure 18. Standard bending test specimen and its relation to the tensile test specimen.

Two different set-ups are eligible for the testing of bending properties, namely the 3-point set-up and the 4-point set-up. Both are displayed schematically in Figure 19.

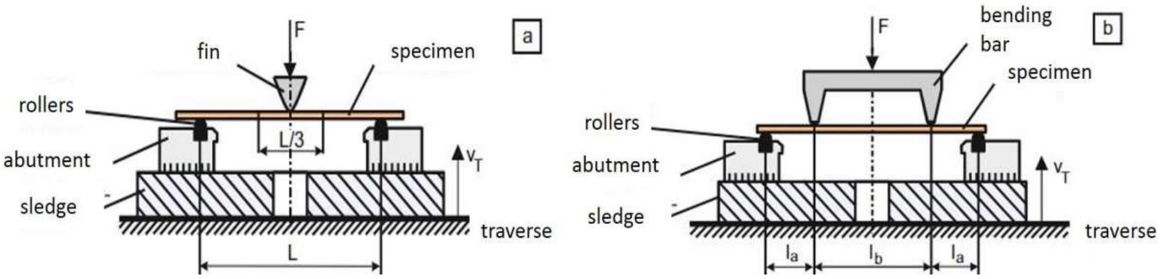

Figure 19. Bending tests in 3-point (a) and 4-point (b) configuration adapted from [72].

The advantages of the 4-point set-up are the homogeneously distributed bending moment and the reduction of transversal forces, increasing the stability of the results. However, the measurement configuration as well as the handling are considerably more complicated and the configuration has higher demands on the precision to yield satisfactory results. Hence, the 3-point set-up is the most commonly used measuring technique for plastics. In any case, results from these two testing set-ups cannot be compared [76].

Under the assumption of symmetrically distributed stresses and strains, a neutral fibre remains in the centre of the specimen. Consequently, the biggest tensile and compression forces act on the outermost fibres of the specimen. The bending stress σ_f in the 3-point set-up is calculated with

$$\sigma_f = \frac{3FL}{2bh^2}, \qquad \text{(VIII)}$$

where F is the applied force, L is the span length, b is the width, and h the height of the specimen. With Hooke's law the respective elongation results in:

$$\varepsilon_f = \frac{3FL}{2bh^2E} \qquad \text{(IX)}$$

Analogous to tensile tests, polymers can show remarkably different behaviour in 3-point bending tests. Typical stress-strain curves and the most important parameters are displayed in Figure 20.

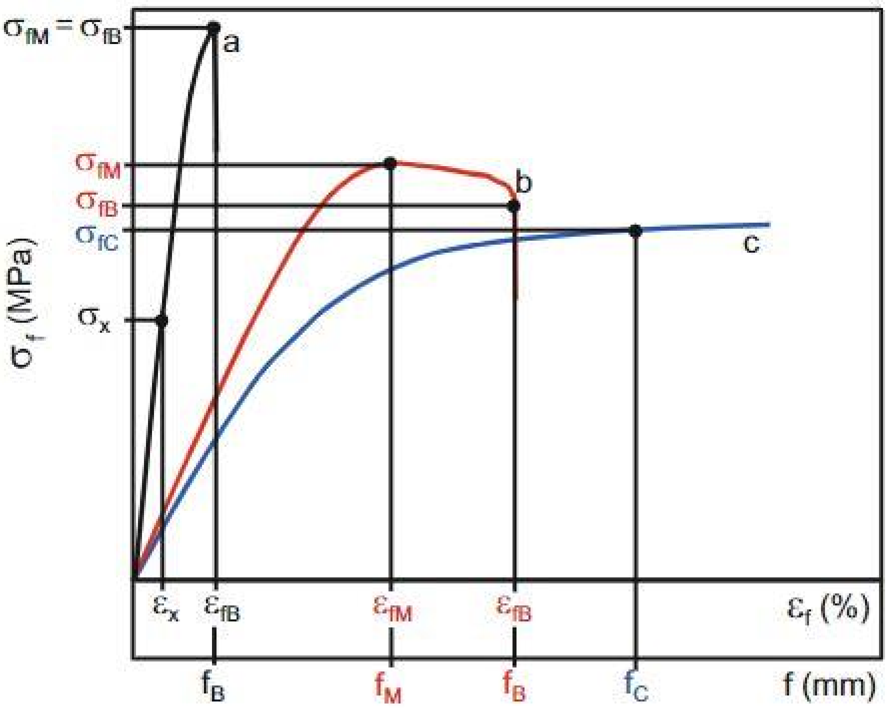

Figure 20. Typical stress-strain curves for polymers in 3-point bending tests. Brittle fracture (a), ductile behaviour with yield point (b) and ductile behaviour without yield point [72].

The resulting parameters are similar to those obtained in tensile test with respect to stress and strain values.

2.4.3 Dynamic mechanical analysis

In Dynamic mechanical analysis (DMA), test specimens are loaded with periodically changing stresses. Multiple testing set-ups are eligible for DMA measurements (e.g., tensile, bending, torsion) and standardized in DIN EN ISO 6721. Two different operation modes can be applied to gain insight into the time and temperature dependent properties [77].

The characterisation for the viscoelastic properties of polymers is conducted by applying a driven sinusoidal oscillation with constant frequency and amplitude onto the sample. The phase shift δ between stress and strain which is constant in linear-viscoelastic materials is measured:

$$\varepsilon(t) = \varepsilon_0 * sin(\omega t) \tag{X}$$

$$\sigma(t) = \sigma_0 * sin(\omega t + \delta) \tag{XI}$$

Hence, stress and strain can be understood as two sinusoidal oscillations with similar frequency and amplitude only shifted by δ (see Figure 21).

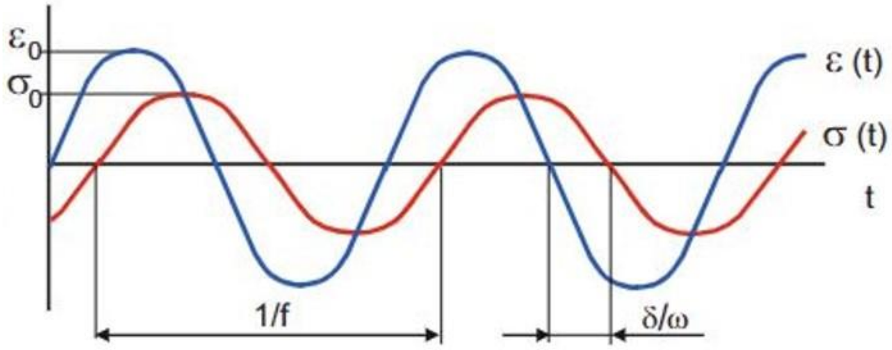

Figure 21. Phase shift between stress and strain under driven oscillation in DMA, adapted from [72].

Hooke's law is still valid but has to be adapted to consider the phase separation:

$$E^* = E' + iE''E \tag{XII}$$

The complex Young's modulus can be viewed as a vector in the complex plane. Its direction is determined by the phase angle δ and its length (i.e., magnitude) is determined by the ratio between stress and strain (see Figure 22).

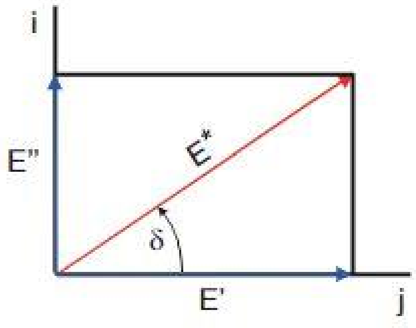

Figure 22. Representation of the complex Young's modulus E^* [72].

Hence, the complex number E^* can be separated into its real part and its imaginary part using standard trigonometric formulae:

$$E' = E^* * cos(\delta) = \frac{\sigma_0}{\varepsilon_0} * cos(\delta) \tag{XIII}$$

$$E'' = E^* * sin(\delta) = \frac{\sigma_0}{\varepsilon_0} * sin(\delta) \tag{XIV}$$

The real part represents the amount of storable energy and is thus called storage modulus. The imaginary part is in connection with the dissipated energy and is hence called loss modulus. Together these two factors characterise the elastic and viscous properties of the tested specimen.

The ratio between storage and loss modulus yields the loss factor *tan δ*. A temperature dependent measurement of storage and loss modulus allows the analysation of the viscoelastic properties over a wide temperature range [78]. The peak of the *tan δ* curve represents the glass transition temperature T_g, a very important parameter defining the application range for polymer materials. An example of a temperature dependent measurement at a frequency of 1 Hz is displayed in Figure 23.

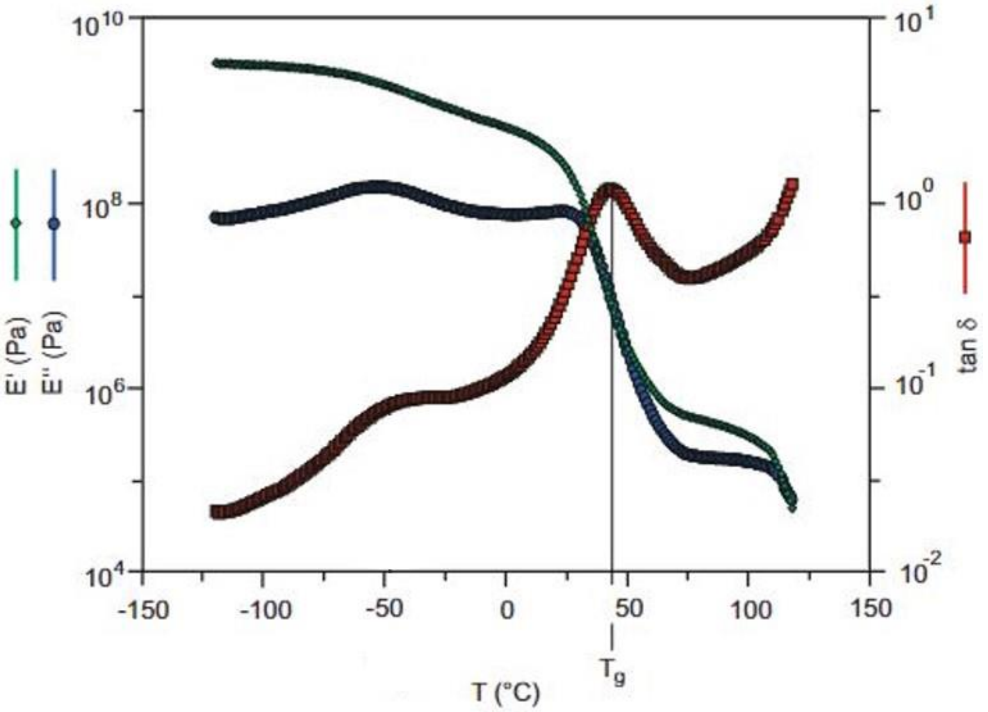

Figure 23. Temperature dependent DMA yielding storage and loss modulus as well as T_g defined by the peak of the *tan δ* curve, adapted from [72].

2.4.4 Hardness tests

Hardness tests are measurement procedures originating from the testing of metals. Generally, hardness describes the ability of a material to withstand the indentation by another body [79]. Different standardised tests are available. In all these tests, a hard indenter (i.e., object penetrating the surface of the specimen) is pressed vertically into the test object. The information about the hardness as well as the material behaviour is gained by analysing the resulting indentation mark. Typical marks for different material characteristics are displayed schematically in Figure 24.

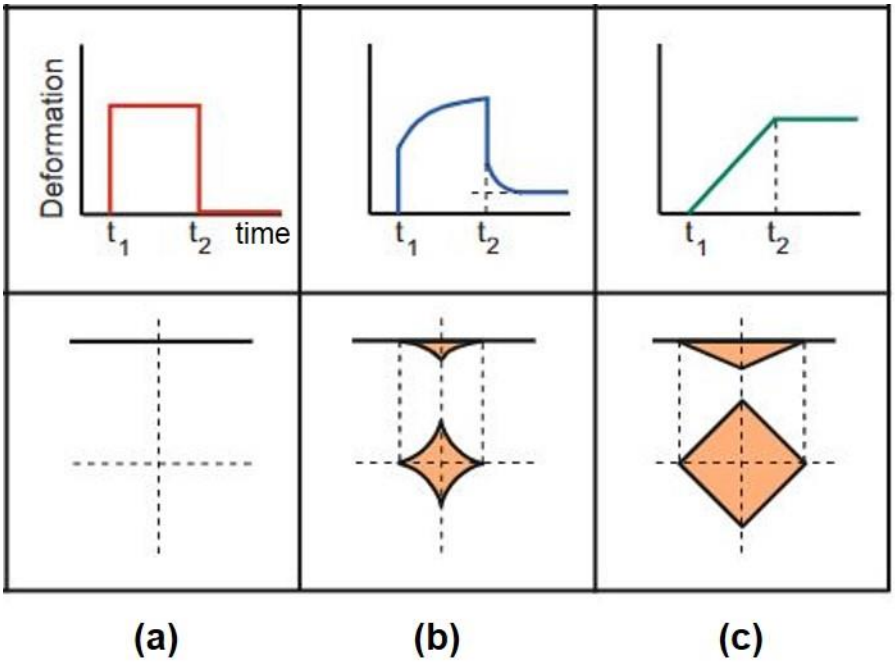

Figure 24. Time dependent deformation behavior (top) and the resulting indentation mark (bottom) of an elastic (a), viscoelastic (b) and plastic (c) material, adapted from [72].

Independently of the used method, hardness tests are relatively easy to perform, requiring only small areas on the surface of the specimen to be destroyed, while the remaining part is conserved. Thus, these procedures are well suited for the testing of small or thin parts. For all these reasons, hardness measurements are one of the most commonly used testing method [80].

The difference between the various measurements is the shape of the indenter, the material of the indenter, as well as the examination parameters (e.g., indentation velocity, indentation depth). Analogous to tensile and bending tests, the specific material behaviour of polymers (e.g., viscoelastic characteristics) must be taken into account [81]. Hence, measuring temperature, velocity, load and indentation time must be noted carefully to guarantee reproducible results.

In the studies present, Vickers hardness measurements are conducted. Thus, this procedure is described in detail in the following.

The indenter is pyramid shaped with a square-based area and an angle of 136 °C between opposite areas. The object is made out of diamond. The measured variable is the length of the diagonal of the somewhat square indentation mark (see Figure 24). The Vickers hardness HV is calculated with:

$$HV = \frac{1{,}8544 * F}{d^2}, \tag{XV}$$

where F is the applied force and d is the mean value of the diagonal length. Vickers measurements are particularly important for measurements in micro hardness measurements where minimal loads and indentation depths are required. [82]–[84].

2.4.5 Impact strength

Apart from slow or quasi-static loading, samples are often under the influence of abrupt stresses [85]. These scenarios are simulated by impact bending tests. Different standardised methods are available for the testing of polymers. The most common ones are Charpy (ISO EN DIN 179) and Izod (ISO EN DIN 180) impact tests, and the less common Dynstat (DIN 53435) standard. The testing set-up for Dynstat impact tests, primarily used in the present work is displayed in Figure 25.

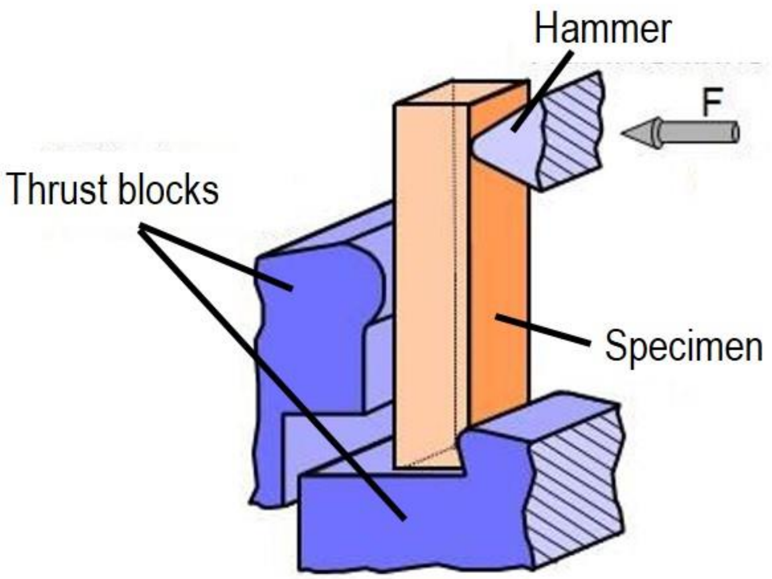

Figure 25. Set-up of theDynstat impact strength test, adapted from [86].

Dynstat impact tests are applicable for small specimen sizes compared to the former two. In all three tests, a hammer fin loads the specimen abruptly. The test is valid if the hammer moves fully through the sample resulting in the destruction of the part. Division of the energy required to destroy the sample by the cross-section yields the impact strength a_c:

$$a_c = \frac{W_c}{b * h}, \tag{XVI}$$

where W_c is the dissipated energy and b and h are the respective width and height.

Although all three testing standards are based on the same principal, the results are not identical and comparison between values obtained by different methods is only viable to a limited extent [87]. Thus, it is essential to note the testing method and reuse the same procedure to gain comparable results.

One major drawback of all these measures is, that the measured impact strength comprises both strength and deformation. This value solely represents the total area under the stress strain curve, that is the result does not allow a direct conclusion to the elastic and plastic properties of the material. A rather stiff as well as a considerably more ductile material can achieve the same value of measured impact strength. This phenomenon is displayed for two different polymer materials in Figure 26.

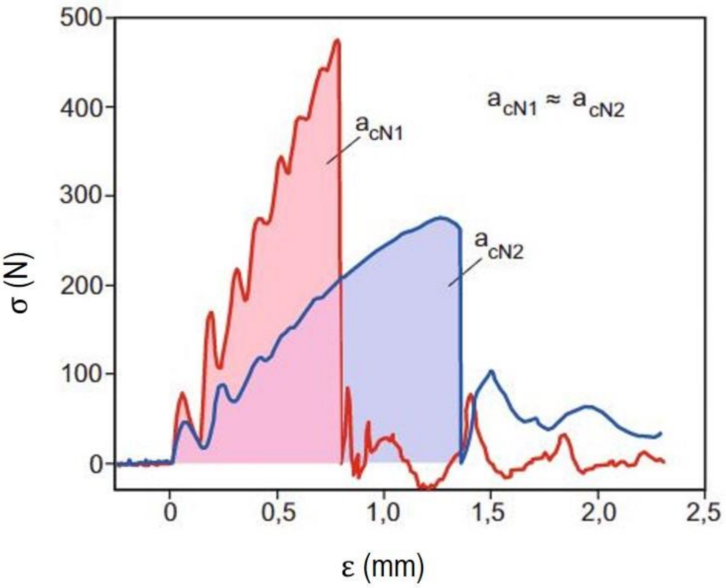

Figure 26. A stiff and high strength material (red) and a weaker ductile material (blue) achieving the same amount of impact strength, adapted from [72].

2.4.6 Fracture mechanics

Samples often fail at lower stresses than theoretically predicted. This can frequently be attributed to the presence of small cracks and notches which lead to local stress concentrations and in further consequence to early failure of the part. Multiaxial stresses, low temperature or high loading rates [88] can also be cause for failure. The origin of cracks are small defects in the material arising either from external factors (e.g., temperature, loading rate, fatigue) or from the internal structure containing imperfections introduced during the production process [89].

2.4.6.1 Testing methods

Special testing procedures are conducted to evaluate the process of fracture. All these examinations require the manipulation of the testing samples before the actual testing, meaning that a crack is deliberately introduced to the specimens by notching it prior to the test.

All testing standards described in 2.4.5 Impact strengthcan be conducted with notched samples to gain insight into the fracture toughness under impact loading. Besides that, the fracture toughness under slow or quasi-static loading can be examined by tensile and bending tests using specifically prepared specimens [90]–[92].

For the studies present, solely the single edged notched bending test specimen (SENB) has been used. Its shape is inspired by the standard bending specimen described in 2.4.2 Bending testwith adapted dimensions and the artificial inclusion of a crack. The dimensions of the SENB standardised in ISO 13586 are displayed in Figure 27.

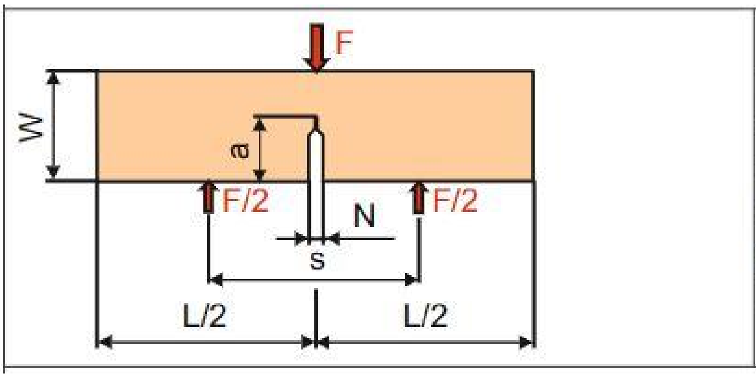

W = 10 mm
B = 2 … 10 mm
L = 80 mm
s = 40 … 70 mm
a = 0,5 … 7,5 mm
N = 2 mm

Figure 27. Shape and dimensions of the SENB [72].

The main difference between fracture mechanical analysis compared to conventional bending tests or impact strength tests is the necessity to measure the position of the crack tip in relation to the applied force continuously [93]. Thus, alterations in the characteristic of the crack can be assigned to specific load values. The quality of the artificially produced crack is one of the key factors for the results of these measurements. In case of polymers, the crack is typically made by slicing the sample with a sharp knife. The blades utilised to produce the crack should be as sharp as possible to ensure that the radius of the crack tip is minimal. Consequently, the stresses at the crack tip and thus the overall stresses on the sample are maximised [94], [95].

2.4.6.2 Basic concepts of linear elastic fracture mechanics

Different theories for the description of the fracture mechanical behavior exist. Depending on the material and its properties, the correct approach has to be taken. Under the assumption of a linear relation between stress and strain and no extensive yielding (i.e., plastic deformation) before fracturing, linear-elastic fracture mechanics (LEFM) can be applied [96]. This theory is also adaptable in case of localised plastic deformation in a small region around the crack tip, which does not lead to the macroscopic yielding in the material. LEFM assumes that the sample stores elastic energy U_{el} when loaded mechanically. A crack with length a needs to convert elastic energy into surface energy δU_0 which is needed to create fresh fracture surfaces to grow by an amount of δa:

$$\delta U_0 = G * t * \delta a, \tag{XVII}$$

where G is the energy release rate and t is the specimen thickness (see Figure 28).

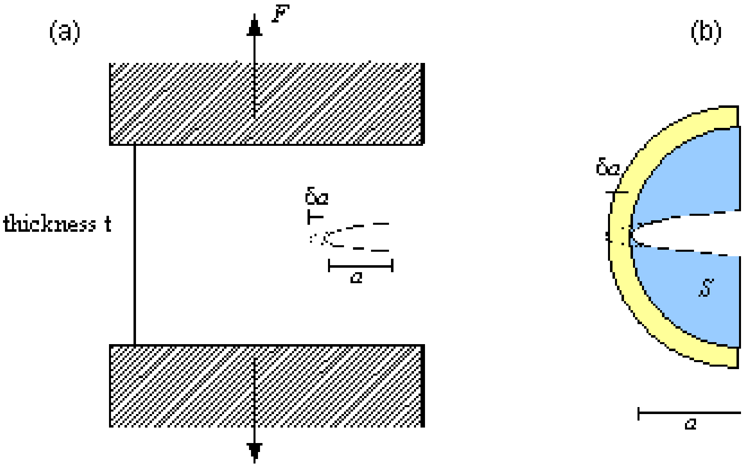

Figure 28. Crack propagation at linear elastic conditions [50].

If the release of elastic energy due to the growing crack is larger than the required surface energy, the crack will grow:

$$-\delta U_{el} = G * t * \delta a \tag{XVIII}$$

Considering that the circumference S of the introduced crack is almost stress-free and linear elastic material behaviour, the released elastic energy can be calculated by multiplying the elastic energy density is $\frac{\sigma^2}{2E}$ with the volume of the semicircle with thickness t:

$$\delta U_{el} = -\frac{\sigma^2}{2E} * \frac{\pi a^2 t}{2} \tag{XIX}$$

If the crack grows by δa additional energy is released:

$$\delta U_{el} = \frac{dU_{el}}{da}\delta a = -\frac{\sigma^2}{2E} * \pi * a * t * \ \delta a \tag{XX}$$

If the elastic energy release rate is larger than the energy-rate required to create new crack surfaces, a critical state involving crack growth and sample failure is reached:

$$G = \frac{{\sigma_c}^2 \pi a_c}{2E} \qquad \text{(XXI)}$$

Rearrangement yields:

$$\sqrt{2GE} = \sigma_c \sqrt{\pi a_c} \qquad \text{(XXII)}$$

Exact crack and specimen geometry is considered by a geometry factor *f*. In many cases *f* = 1 is a good approximation. The term $\sqrt{GE}$ is called the critical stress intensity factor $K_{c.}$ Hence,

$$K_c = \sigma_c f \sqrt{\pi a_c} \qquad \text{(XXIII)}$$

This parameter measures the stress concentration at the crack tip and is dependent on the applied stress and the crack length. If the parameter K exceeds K_c, the specimen will fail. Thus, Kc is the linear elastic fracture toughness.

$$K \; > K_c \qquad \text{(XXIV)}$$

Depending on the direction of the external stresses, various stress states are possible at the crack tip (see Figure 29).

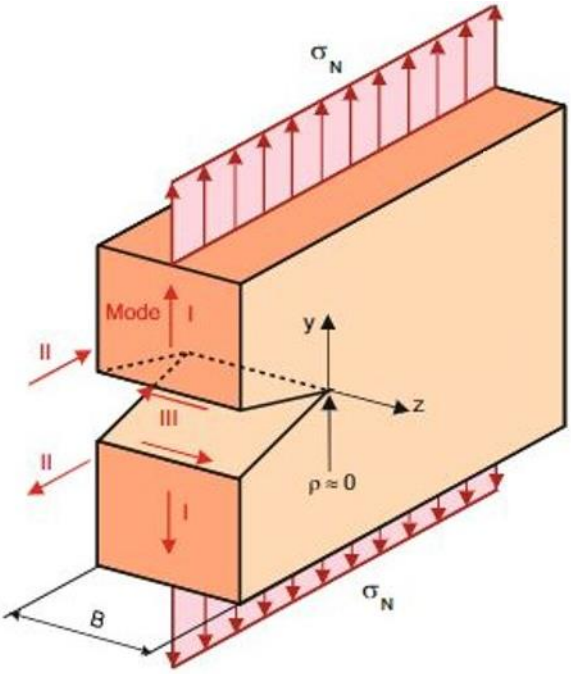

Figure 29. Stress modes at the tip of a crack with infinitely small crack tip radius, adapted from [72].

Although arbitrary combinations of these stress modes are possible, the most common and relevant circumstance is the pure mode I stress condition where the applied load is perpendicular to the crack surface. Modes II and III represent shearing as well as torsion, respectively.

Materials showing plastic deformation in the vicinity of the crack tips cannot be described by linear-elastic fracture mechanics theory. Before crack propagation starts, a plastic zone around the crack tip forms which leads to the blunting of the crack tip. Hence, the assumption of an infinitely small crack tip radius is not valid [97]. Depending on the size of the plastic zone around the crack tip, three different states, depicted in can be defined [98].

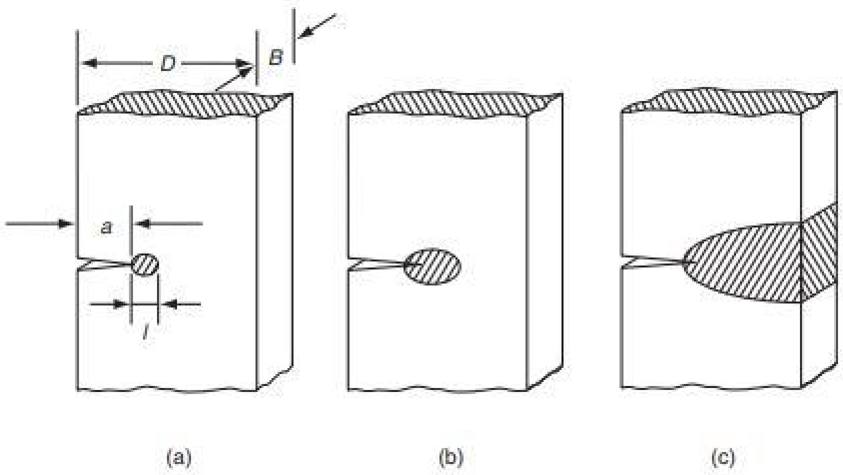

Figure 30. Different sizes of the plastic zone around the crack tip, described as small-scale yielding (a), contained yielding (b), and fully developed plasticity (c) [98].

If the extent of the plastic zone l is small compared to the crack length a, and the specimen thickness and width D and B, respectively, the overall response of the part differs very little from a purely elastic one outside the plastic zone. In case of contained yielding the plastic zone is still smaller than the unaffected ligament but might lead to different stress and strain distributions inside and outside the plastic zone. Fully plasticity implies the plastic zone being developed over the entire cross section of the specimen resulting in substantially different response compared to elastic behaviour [98].

The most commonly used method for the quantification of samples displaying plastic deformation at the crack tip in the field of polymers is the J-Integral [99]. This path-independent line integral, representing a non-linear elastic fracture mechanics approach, encloses the entire plastic zone around the crack tip and lies in the elastically deformed area of the sample (see Figure 31).

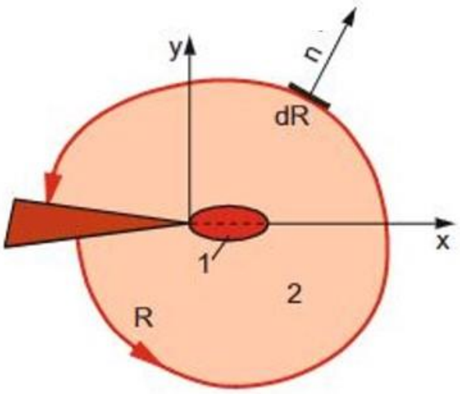

Figure 31. Path independent J-Integral around the plastic zone (1) at the crack tip in the linear-elastic region, adapted from [72].

x- and y- component of the J-Integral are defined as:

$$J_x = \int_R W dy - T_{ij} * n_j \frac{\partial u}{\partial x} dR \tag{XXV}$$

$$J_y = \int_R -W dx - T_{ij} * n_j \frac{\partial u}{\partial x} dR \tag{XXVI}$$

W is the elastic strain energy density, *T* is the stress tensor, *n* is the normal to the curve *R*, and *u* is the displacement vector.

In case of a defect free sample, the integral yields zero but is other than zero for materials containing discontinuities like a crack.

Values for the J-Integral can be found experimentally by constructing JR-curves, where J-values are plotted against the crack growth at each instant. Continuous measurement of load and loading point displacement are required to construct these curves. The diagram then shows two areas, the first describing blunting of the crack tip and the second propagation of the crack. The critical value J_c representing the initiation of crack propagation can be found as the lower number of J_{BL} and $J_{0,2}$ representing the intersection of the measured data points with the blunting line and the 0.2 mm offset line (see Figure 32).

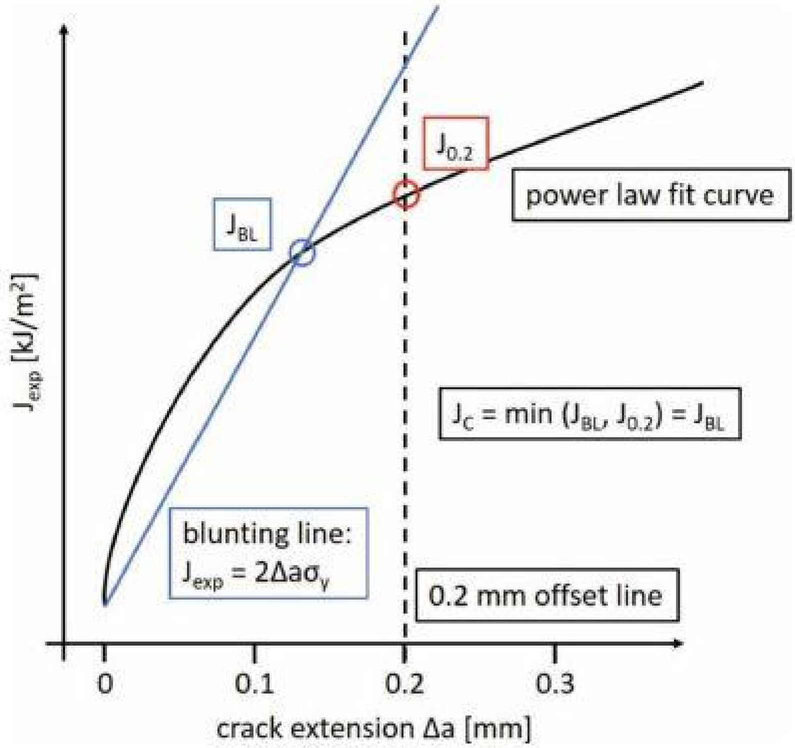

Figure 32. Experimental determination of Jc [100].

2.4.6.3 Toughening of photopolymers

Toughening of photopolymers is a challenging task because these polymers feature a significant amount of cross-links between polymer chains (i.e., thermosets). These covalent bonds yield high stiffness and strength but render photopolymers rather brittle and prone to fracture. This is especially important in 3D printing, since small defects and impurities in the material arising from the production process cannot be avoided completely. These imperfections act as locations of crack initiations and consequently to the failure of the specimen by fatale crack propagation. Although toughening of polymers has been approached in different ways (e.g., rubber particles, adaptation of monomers), it remains a challenging task to increase toughness while conserving strength and stiffness.

A promising technique is the production of composite materials composed of two separate material featuring opposite mechanical properties. A basic design criterion has been established relying on continuous and strong spatial variation of Young’s modulus:

$$\frac{\sigma_{fr}^{comp}}{\sigma_{fr}^{hom}} = (1-\kappa_E)\sqrt{\frac{1}{\psi}\frac{2a_n}{\lambda}\frac{E_g}{E_p}} \tag{XXVII}$$

σ_{fr} represents the fracture strength of a composite and a homogeneous material, respectively. K_E describes the loss in Young's modulus due to the insertion of soft interlayers, ψ is a geometry factor, a_n is the crack length and λ is the distance between the interlayers. Finally, E_g and E_p represent the Young's modulus of stiff and soft material, respectively [101].

Hence, a large difference of Young's Modulus as well as short distances between the interlayers are beneficial. Since, even very thin interlayers work effectively, these structures should be designed rather thin to conserve the stiffness of the homogeneous material. The soft interlayers act as crack stoppers effectively reducing the crack driving force and thus increasing the fracture toughness significantly [101]. Comparison between a homogeneous and a composite material is displayed schematically in Figure 33.

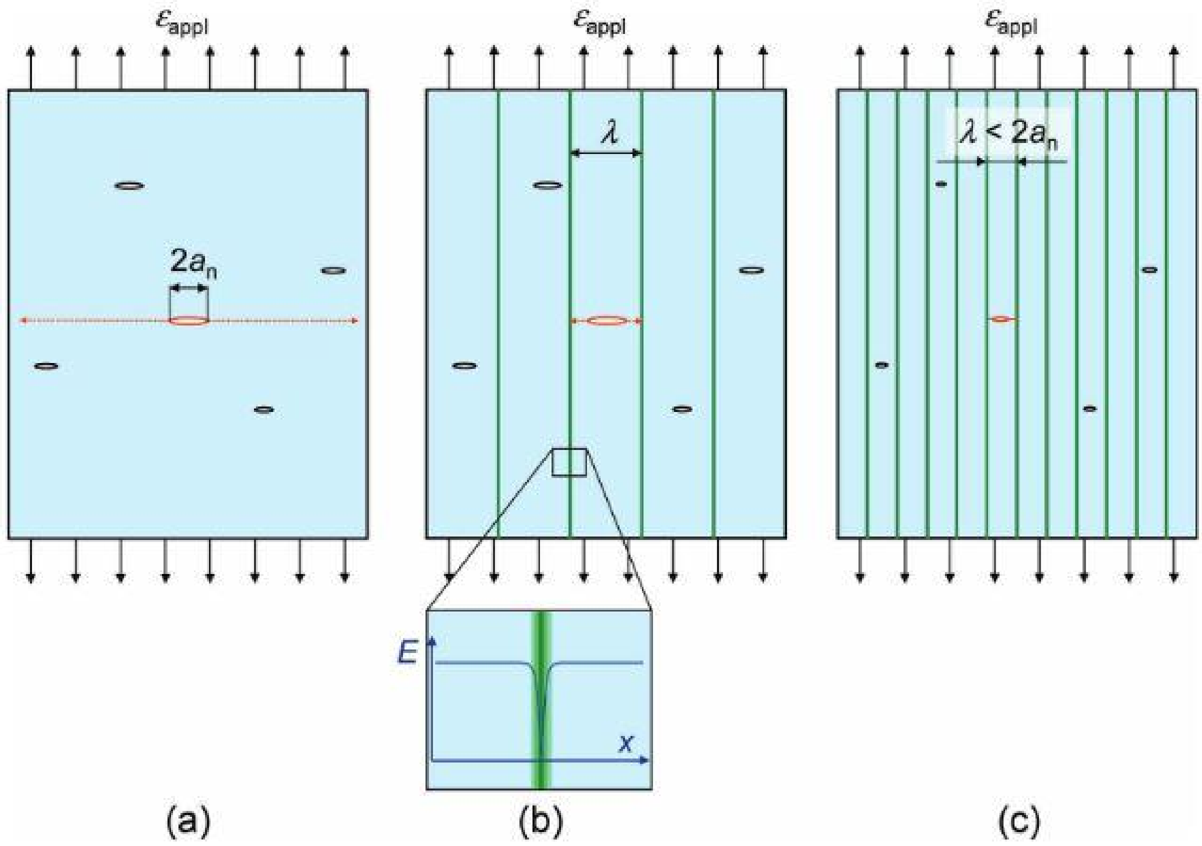

Figure 33. After crack initiation, the crack with initiatl length a_n propagates through a brittle material resulting in fracture (a). Thin soft interlayers featuring low Young's modulus act as effective crack stoppers (b). Smaller distance between interlayers λ results in higher fracture strength of the specimen (c) [101].

3 Material composition and printing method

3.1 Resin Compositions

The resins utilised in this work consist of various organic and inorganic substances. The organic part of the resins mainly consists of different reactive monomers and oligomers as well as a photoinitiator. In addition, the dispersing agent, the absorber and a non-reactive solvent are organic substances. The inorganic part is composed of fillers, and the rheological agent. The compositions of all resins used in this work are based on similar resins successfully applied in 3D printing applications [102]–[104].

3.1.1 TCP I Resin

The reactive part of the Tricalcium phosphate (TCP) resin is composed of a trifunctional methacrylate as well as two difunctional methacrylates in combination with a type I photoinitiator. Additionally, a polymeric dispersant and an absorber is added to the composition. The inorganic phase is composed of TCP particles, and a non-soluble rheology additive. The detailed material composition is displayed in Table 2.

Table 2. Composition of the TCP I resin

Component	**Content (wt %)**	**Content (vol %)**
Ethoxylated 3-Bisphenol A Di-Methacrylate (Arkema, Colombes, France)	33.3	51.6
Triethylenglycoldimethacrylat (Arkema, Colombes, France)	5.0	5.0
Urethane dimethacrylate (Arkema, Colombes, France)	5.0	5.0
Dispersing agent – D540 (Lubrizol, Wickliffe, USA)	1.0	1.5

Component	Content (wt %)	Content (vol %)
(2,4,6-trimethylbenzoyl)-phenylethoxyphosphine oxide (TPO-L) (Lambson, Wetherby, UK)	0.1	0.2
Absorber – 2,2-Dihydroxy-4,4-imethoxybenzophenone (TCI, Tokio, Japan)	0.03	0.05
Rheology additive – Fumed silica (Merck, Darmstadt, Germany)	0.6	0.9
β-Tricalcium phosphate TCP (Merck, Darmstadt, Germany)	55.0	30.4

The combination of three different methacrylates ensures both sufficient cross-linking for mechanical properties and low viscosity, necessary for the printing procedure. Moreover, the toxicity of the composition is reduced by replacing conventionally used acrylate components by methacrylates due to their lower reactivity [105]. A slight increase in photoinitiator content is required to account for the lower reactivity of the monomeric components. The PI used in this composition absorbs in the wavelength range of 325-415 nm with a maximum at 370 nm [106]. The rheology additive prohibits particle sedimentation, thus granting long time storage stability of the liquid resin. The absorber prevents polymerisation in undesired voxels due to light scattering (i.e., over-polymerisation). Thus, specimen contours are sharper and conform to the desired shape. TCP particles are added to increase hardness, strength, and stiffness of the printed specimens.

3.1.2 TCP II Resin

The composition of the TCP II resin evolved from the composition of TCP I. While the principle of different organic components in conjunction with inorganic fillers is preserved, substantial adaptations are made. The detailed composition of the TCP II resin is displayed in Table 3.

Table 3. Composition of the TCP II resin

Component	**Content (wt %)**	**Content (vol %)**
Propoxylated trimethylolpropane triacrylate (Arkema, Colombes, France)	8.72	20.3
Urethane dimethacrylate (Arkema, Colombes, France)	7.80	13.71
Poly(propylene glycol) (Merck, Darmstadt, Germany)	10.52	16.18
Dispersing agent – D500 (Lubrizol, Wickliffe, USA)	0.91	1.49
Rheology additive – Fumed silica (Merck, Darmstadt, Germany)	0.36	3.73
Absorber – 2,2-Dihydroxy-4,4-imethoxybenzophenone (TCI, Tokio, Japan)	0.01	0.03
(2,4,6-trimethylbenzoyl)-phenylethoxyphosphine oxide (TPO-L) (Lambson, Wetherby, UK)	0.05	0.07
β-Tricalcium phosphate (Merck, Darmstadt, Germany)	71.63	44.48

The multifunctional monomeric components ensure sufficient cross-linking between the polymeric chains. Thus, increasing stiffness and strength of the cured resin. The TCP content is significantly increased to further improve strength and stiffness. However, this increase naturally leads to an increase in the viscosity of the raw material. To keep the viscosity at a processible level the overall viscosity has to be decreased which is done by addition of a non-reactive diluent (i.e., Poly(propylene glycol)). The higher TCP particle content results in higher absorption during the curing. Consequently, the amount of absorber could be lowered while conserving good spatial resolution.

3.1.3 TCP III Resin

The most important modification in this composition is the substitution of the non-reactive diluent by a reactive product. Thus, increasing overall reactivity of the resin and omitting unpolymerised liquid phases inside the printed samples. This composition represents a compromise between the former two resins. The biggest achievement is the removal of the non-reactive diluent. However, the TCP content had to be reduced as well to reach sufficiently low resin viscosity. Minor changes in the composition are implemented to further increase the spatial resolution and the surface quality of the printed parts.

The detailed composition of the TCP III resin is displayed in Table 4.

Table 4. Composition of the TCP III Resin

Component	Content (wt %)	Content (vol %)
Ethoxylated 3-Bisphenol A Di-Methacrylate (Arkema, Colombes, France)	33.2	50.6
Triethylenglycoldimethacrylat (Arkema, Colombes, France)	5.0	7.9
Urethane dimethacrylate (Arkema, Colombes, France)	5.0	7.7
Dispersing agent – D540 (Lubrizol, Wickliffe, USA)	1.0	1.5
(2,4,6-trimethylbenzoyl)-phenylethoxyphosphine oxide (TPO-L) (Lambson, Wetherby, UK)	0.15	0.3

Component	Content (wt %)	Content (vol %)
Absorber – 2,2-Dihydroxy-4,4-imethoxybenzophenone (TCI, Tokio, Japan)	0.03	0.05
Rheology additive – Fumed silica (Merck, Darmstadt, Germany)	0.55	0.9
β-Tricalcium phosphate (Merck, Darmstadt, Germany)	55.0	30.4

Representative SEM images of particle size and geometry of the TCP powder used for all resins are displayed in Figure 34.

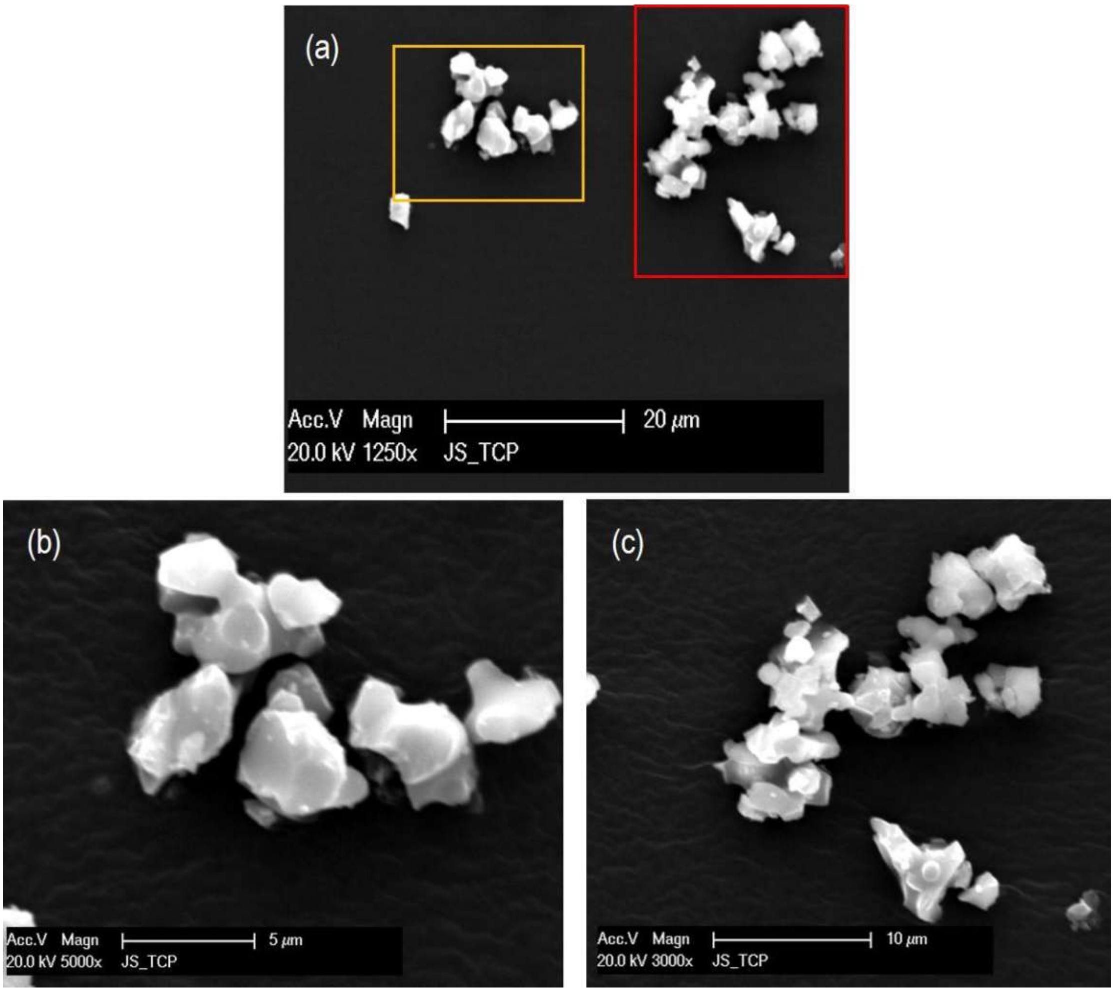

Figure 34. SEM images of the TCP poder used. Overview of particles (a) and higher magnification images of orange area (b) and red area (c).

3.2 Ink Composition

Throughout the studies, two different ink compositions are utilised. Both consist of a specific combination of polymerisable monomers, a photoinitiator and a colouring agent. The latter being important for optical detection and verification of homogeneously jetted layers.

3.2.1 Cyano Ink

This ink is mainly based on two different acrylates. One being mono-functional while the other is di-functional to amplify crosslinking. Both substances are low viscosity materials rendering the final ink processible at room temperature. The colouring agent is not based on pigments thus being soluble (i.e., dye). The PI used in this composition differs from the product processed in the resins. The detailed composition of the Cyano ink developed by Bettina Koch is displayed in Table 5.

Table 5. Composition of the Cyano ink.

Component	**Content (wt %)**	**Content (vol %)**
Cyanoacrylate (Abcr, Karlsruhe, Germany)	90.69	96.89
Poly(propylene glycol) diacrylate (Merck, Darmstadt, Germany)	6.11	1.91
Rhodamine B (Merck, Darmstadt, Germany)	0.12	0.25
Phenylbis (2,4,6-trimethylbenzoyl)-phosphine oxide (BAPO) (Merck, Darmstadt, Germany)	3.08	0.95

Phenylbis (2,4,6-trimethylbenzoyl)-phosphine oxide BAPO offers a broader absorbance spectrum than TPOL used in the resin compositions [107]. This adaptation is necessary to ensure proper polymerisation leading to sufficient solidification of the ink component cured with a 460 nm light emitting diode (LED). Moreover, due to the smaller absorbance band of TPOL at higher wavelengths, the curing process of the ink does not affect the resin component.

3.2.2 Tango Ink

This ink is mainly chosen for its good mechanical properties leading to high elongation at break in mechanical tests [108]. Since this product is a commercially available product, the specific composition and contents are proprietary. The colouring agent Rhodamine B is added to the premixed composition to allow detection of the ink component after the manufacturing process. The composition of the Tango ink produced by Bettina Koch is displayed in Table 6.

Table 6. Composition of the Tango ink.

Component	**Content**

Proprietary	30 – 50 wt. %
Proprietary	30 – 50 wt. %
Proprietary	30 –50 wt. %
Acrylic acid, 2-hydroxyethyl ester	0.3 – 1 wt. %
2,6-Bis(1,1-Dimethylethyl)-4-Methyl-Phenol	0.1 – 0.3 wt. %
Glycerol, propoxylated, esters with acrylic acid	0.1 – 0.3 wt. %
Rhodamine B (Merck, Darmstadt, Germany)	0.02395 wt. %

3.3 Hybrid printing system

The hybrid printing system consists of two independently working systems. First, a stereolithography based 3D-printing system. Second, an inkjet printing station incorporated in the hull of the printer. The combined usage of these two techniques results in the hybrid printing system [109]. This machine as well as the hybrid printing procedure are described in detail in the following sections.

3.3.1 SLA Printer

The SLA printer is based on the principal of DLP. UV-light (wavelength $\lambda = 375$ nm) is utilised to solidify the light sensitive resin. The curing light is projected via a DMD through the vat onto the liquid resin. The light engine (Luxbeam 4600, Visitech Engineering GmbH, Wetzlar, Germany) provides Full HD (i.e., 1920 x 1080 pixel) resolution with a spatial resolution of 50 µm in horizontal directions. Minimal layer thickness is theoretically around 10 µm using this system. Each mirror of the DMD representing a single pixel can be activated separately. The maximum energy density of this system is 40 mW/cm². The UV-light source is located under a transparent glass vat coated with a silicon layer. This silicone layer is located at the top side of the vat facing the material. The compliant layer maximises the contact area between the building platform and the vat. The vat can be heated by means of two heating cartridges located under the vat. An aluminium plate placed between the cartridges and the glass vat to ensure a homogeneous temperature distribution over the vat surface (see Figure 35).

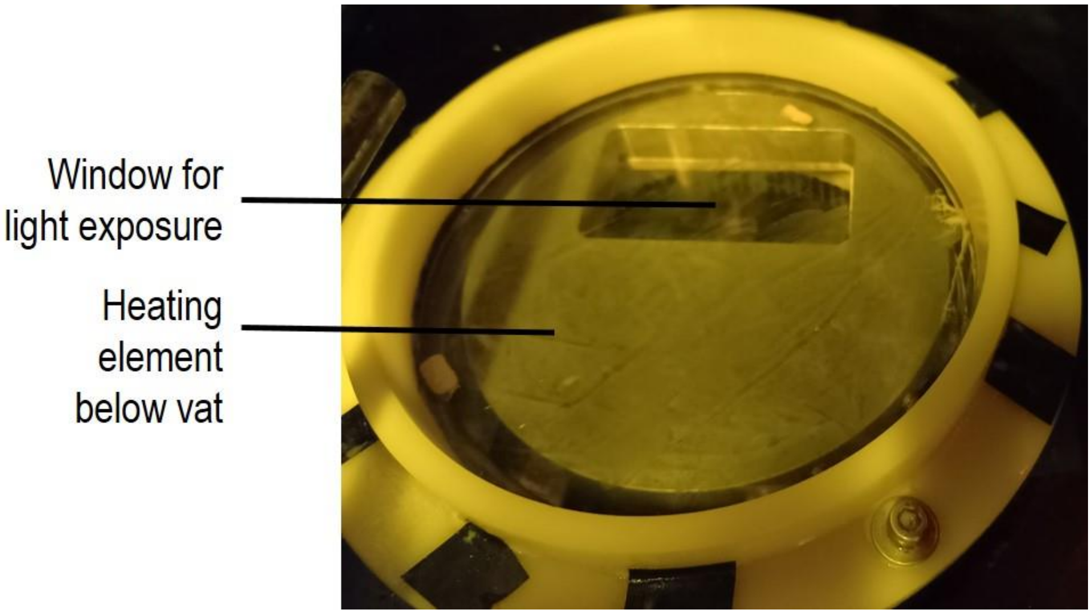

Figure 35. Top view of the vat. The heating element contains a window for the exposure by the light source below.

In order to withstand the high temperature differences generated by the heating element, special boron-silicate glass is utilised [110]. The vat is rotatable and with a coating knife attached to it (see Figure 36).

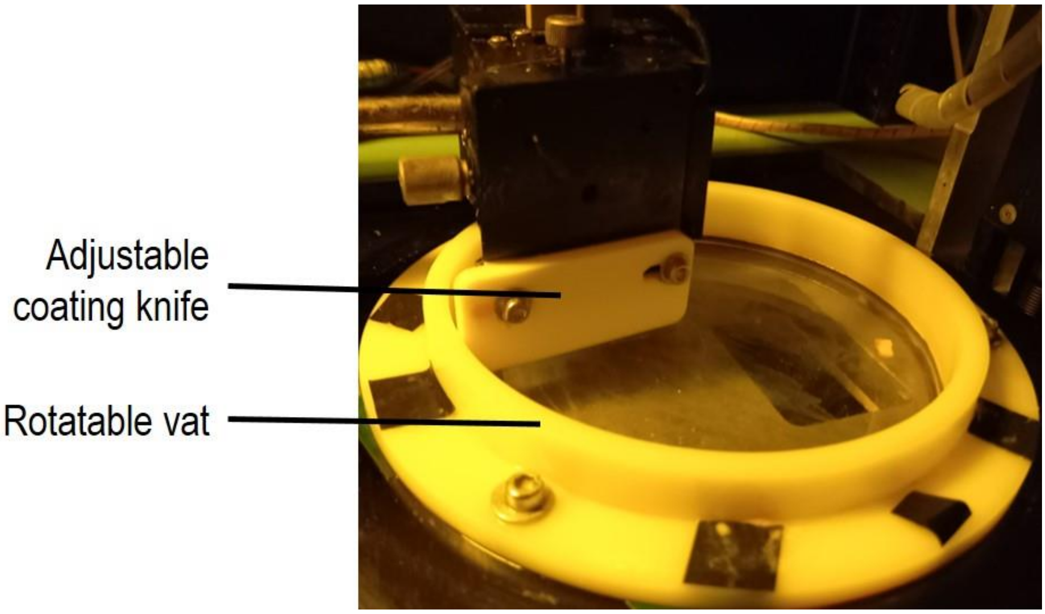

Figure 36. Rotatable vat with the height adjustable coating knife attached.

This rotational coating mechanism allows a more compact machine design than traditional linear coating systems. Moreover, the coating time and thus the overall printing time can be reduced drastically by this design. This mechanism ensures good circulation of the resin resulting in homogeneously distributed thin liquid resin layers.

The building platform consists of a glass surface, which is roughened to increase the surface area and consequently the adhesive forces between the solidified resin and the building platform [111]. The glass board is permanently attached to a metal holder (see Figure 37).

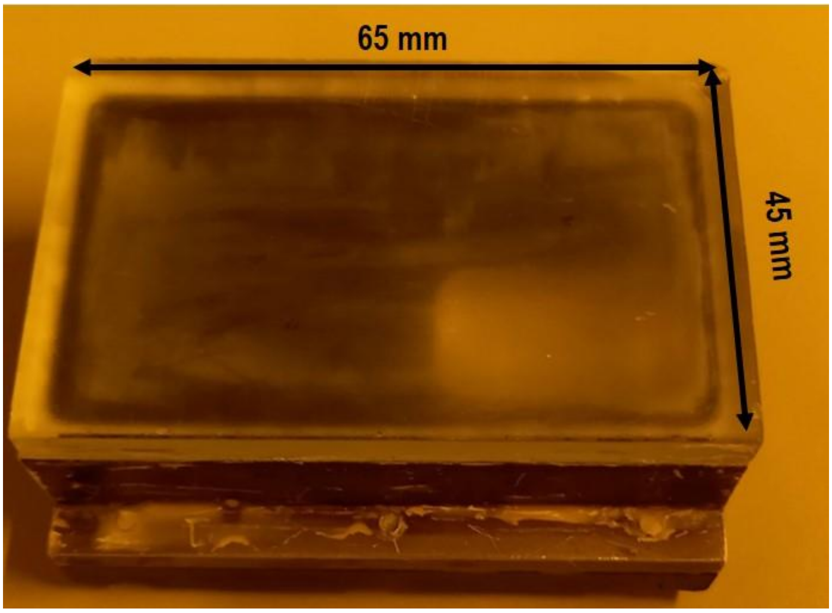

Figure 37. Building platform consisting of a glass plate fixed to a metal mounting.

This metal holder can be mounted to the movable axis of the printer. Via this attachment, the building platform can be moved linearly in vertical direction as well as rotated (see Figure 38).

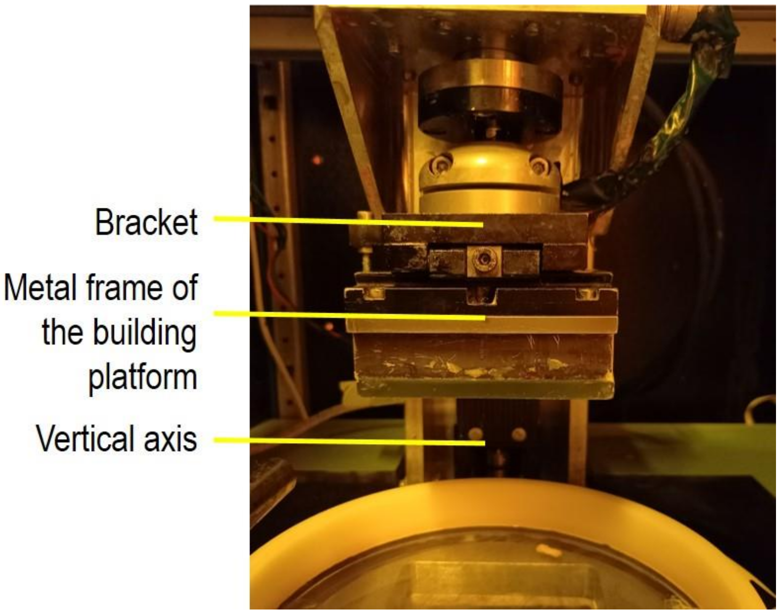

Figure 38. Building platform mounted to the printer. The rotatable vat is visible at the bottom side.

The building space is defined by the dimensions of the rectangular building platform limiting the possible specimen sizes to 65 mm x 45 mm in x- and y-direction, respectively. The maximum size in z-direction is around 80 mm restricted by the length of the vertical machine axis of the printer. The main components of the 3D-printer as well as an exemplary working cycle are displayed in Figure 39.

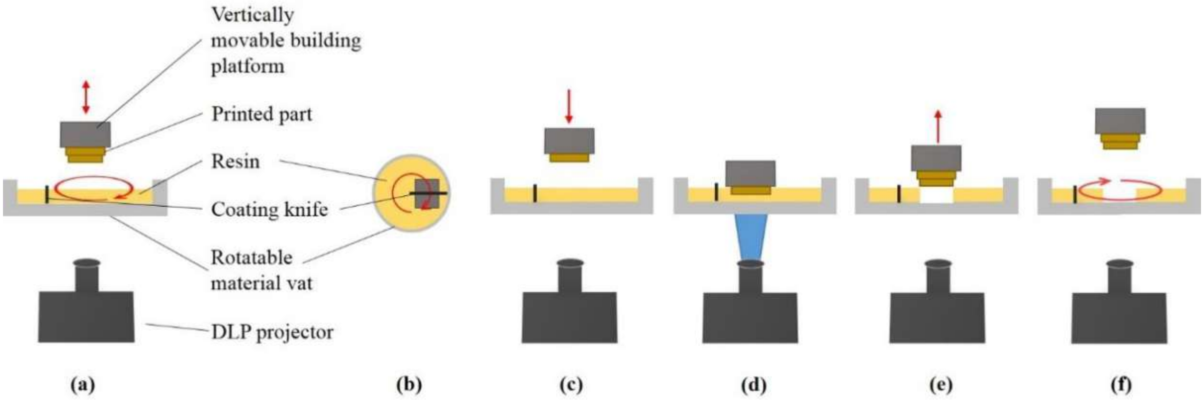

Figure 39.Workflow of the 3D-printing process. Main components of the 3D-printer (a). Top view of the building platform (b). Building platform with the attached layers is immersed into the vat (c). A layer is cured by UV light and attaches to the already existing layers (d). The platform is lifted (e). Vat surface is coated with fresh resin (f). Adapted from [112]

Printing parameters used to process the different TCP resins are summarised in Table 7.

Table 7. Printing parameters for TCP resins.

Parameter	TCP I	TCP II	TCP III
Layer height	25 µm	25 µm	505 µm
Vat temperature	25 °C	55 °C	25 °C
Exposure time layers 1-5	3 s	3.5 s	3 s
Exposure time layers > 5	2.5 s	3 s	2.5 s
Exposure intensity	40 mW/cm²	40 mW/cm²	40 mW/cm²

3.3.2 Inkjet system

The inkjet system consists of multiple components essential for the constant production of inkjet droplets at the desired locations. This DOD system operates through activation of piezo crystals building the walls of the nozzle channels. When charged with electric current, these walls deform creating a pressure wave inside the channels. The pressure wave presses ink through the channels towards the nozzle openings, where ink droplets are jetted. Through alteration of the waveform and the frequency of the electric pulses, the jetting pattern can be adjusted. The main components in permanent contact with the flowing ink are an inkjet print head (Xaar 1003 GS40, Xaar, UK) as well as two stainless steel tanks. These two elements in combination with flexible tubes form the fluid system. The fluid system allows constant ink circulation through the system even if it is not jetting. The ink flow is ensured by a pressure gradient between the two tanks. On one of the tanks (T1) negative pressure (P_{out}) is applied, while on the other tank (T2) positive pressure (P_{in}) is applied. Furthermore, T2 contains a floating sensor measuring the current ink level in the tank. T1 and T2 are connected via a membrane pump pumping ink from T1 to T2. The pump is activated when the fluid level reaches a predefined value in T2. The pressure gradient provides a constant flow of ink through the inkjet print head installed between T1 and T2. The flow rate can be manipulated by changing the applied pressure on the tanks. A bigger pressure gradient results in a higher ink flow rate. P_{in} and P_{out} must be adapted to provide sufficient meniscus pressure at the nozzles. First, P_{in} is increased yielding a higher amount of ink transferred into the print head. Thus, ink starts to leak from the nozzles. Second, P_{out} is increased until ink leakage stops. At this point P_{out} is increased slightly more to ensure a negative meniscus pressure at the nozzle location.

With this basic setting, the ink circulates through the entire system including the print head. The liquid flows through the inlet into the central ink chamber of the print head. From this location, two channels lead to the outlet where the liquid flows towards the tank. The symmetrically located channels run over the nozzles. Hence, the circulating ink permanently flows over the nozzles.

The print head is equipped with 1000 nozzles and provides a spatial resolution of 360 dots per inch (dpi), which is two rows of nozzles with 180 dpi each and a distance of approximately 141 µm between nozzles of one row. This print head has a nozzle diameter of 48 µm. The device operates in single pass mode with 70.5 µm between adjoining drops and around 40 pL drop volume. The tanks can be heated electrically to a maximum temperature of 100 °C thus allowing the adaptation of the rheological properties of the ink (e.g., viscosity, surface tension). The permanent circulation of the ink through the whole system ensures homogenous temperature in all parts of the inkjet system. In addition, phase separation and sedimentation of inkjet components are prohibited by this technique. The application of ink is managed via two colour bitmap-files of according resolution. The entire surface of the building platform is represented by individual pixels. The bitmap-files define each pixel to be jetted or to be omitted (i.e., black or white pixels in the bitmap-file). A printing manager board regulates the excitation of the piezo crystals resulting in the jetting of ink droplets. Firing rate of the piezo elements as well as supplied voltage can be adapted via the board. Rough evaluation of droplet quality can be done by means of a drop-watching system (DW) also integrated in this inkjet system. This subsystem allows the qualitative assessment of meniscus pressure, potential print head coating, as well as formation of desired drops and undesired satellite drops and their shape.

After jetting, the liquid ink is fixated to the building platform or previously solidified material by exposition to a LED array ($\lambda = 455$ nm). The curing of the ink is performed under nitrogen atmosphere to reduce oxygen inhibition reducing the polymerisation process [113]. The array provides an exposure dose of 45 mW/cm² and a penetration depth of 200 µm. Although the inkjet system is running automated with regard to ink circulation, drop generation, and jetting, the curing process has to be done manually. The LED panel equipped with the nitrogen supply is not integrated in the inkjet device, thus activation and application of the curing step are not performed automatically. A schematic illustration of the inkjet system is depicted in Figure 40.

Different settings are used to provide satisfactory drop production. The different parameters used for the cyano ink and the Tango ink are displayed in Table 8.

Table 8. Inkjet parameters for the different inks.

Parameter	Cyano ink	Tango ink
Active nozzle rows	2	2
Driving voltage for piezo crystals	27 V	25.5V
Printing distance	4 mm	5 mm
System temperature	25 °C	75 °C

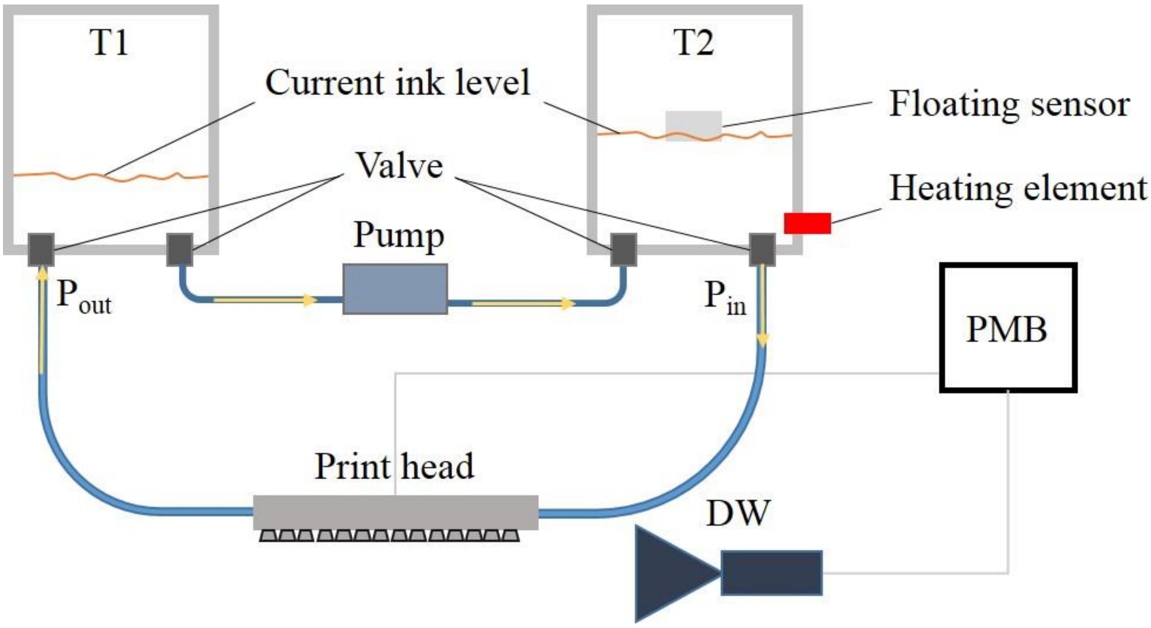

Figure 40. Illustration of the inkjet system. Yellow arrows indicate the direction of the ink flow.

3.3.3 Hybrid printing system

The hybrid printing system consists of the combination of both the SLA printer and the inkjet system. The device allows the printing of specimens consisting of an arbitrary sequence of SLA printed layers and areas of applied inkjet. Although the SLA printer and the inkjet system are active at the same time, the systems operate consecutively. While the SLA printer solidifies a material layer, the inkjet system is idle and vice versa. The raw liquid materials are specifically composed to suit requirements of the hybrid printing system. Two different photoinitiators are used in the resin and ink components offering distinguished absorbance spectra. Thus, the curing process of the ink component only marginally affects the liquid resin, while the fixated ink is additionally cured by the next SLA curing cycle. A working cycle of the hybrid printing system is depicted in Figure 41.

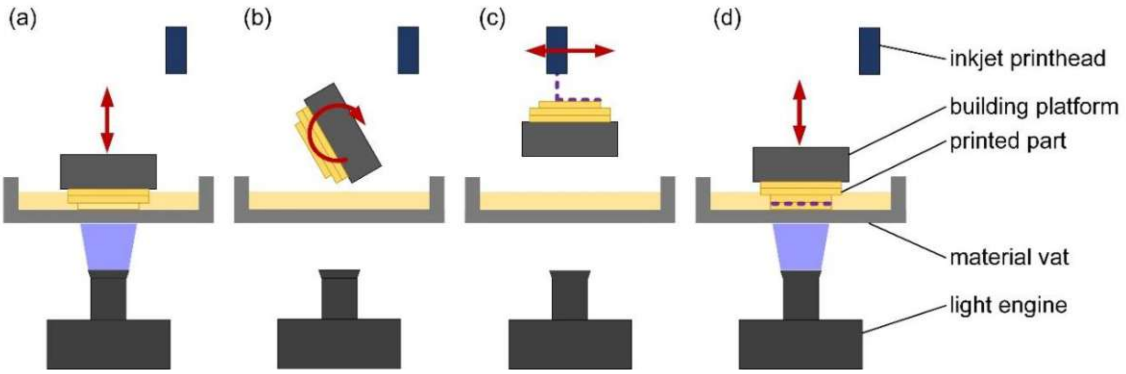

Figure 41. Workflow of the hybrid printing system. (a) The building platform immerses into the vat and a layer is printed; (b) the building platform rotates upwards; (c) an inkjet layer is printed and fixated; (d) after rotating downwards, the ink layer is fully cured and the next resin layer is printed [114].

4 Experimental

In the following section, the experimental results are shown, grouped into three parts.

In the first part, potential anisotropic behaviour of SLA printed samples is examined. Anisotropy could influence the results from thermo-mechanical testing. A major consequence would be the necessity to produce and measure samples printed in at least three main printing orientations to acquire somewhat comparable results. Thus, a larger amount of required samples along with drastically increased production time would be required.

In the second section, a new approach to increase toughness of SLA printed samples is used. A hybrid printing system allowing the application of ink via inkjet system in combination with conventional SLA is utilised to produce a two material system. The main aim is to increase the fracture toughness by application of a second component (i.e., ink) with substantially different mechanical properties.

In the final part, deeper analysis of the fracture behaviour of samples produced with the hybrid printing system is conducted. Adapted raw materials are used to increase the overall performance of the samples and their applicability. Thorough assessment of the fracture mechanical properties as well as the underlining effects leading to the respective behaviour is done.

4.1 Assessment of thermo-mechanical anisotropy

In solid material systems, thermo-mechanical anisotropy (i.e., the directional dependence of a material's property) plays a significant role. It is a characteristic of natural materials (e.g., wood, human bones) as well as engineered materials [115]–[118]. In 3D printing technology, this property is of particular interest due to the layer-wise building pattern characteristic to all 3D printing techniques. Each part consists of layers featuring a specific orientation leading to a macroscopic material orientation in the constructed part. Anisotropy can have a major impact on the mechanical properties and thus might affect the overall performance of the produced part. Studies on AM technologies suggest varying anisotropy of printed parts depending on the manufacturing process and the raw materials [119]–[121]. In case of SLA, there are studies suggesting limited mechanical anisotropy compared to other techniques [122]–[124]. However, the majority of the studies investigating photopolymers do not consider composite materials. Therefore, the thermo-mechanical anisotropy of the composite material must be assessed in order to correctly incorporate the potential effect of this phenomenon in future studies.

Moreover, isotropic behaviour would decrease the production time of samples and increase the capacity of a single printing job due to arbitrary sample orientation of samples on the building platform.

4.1.1 Sample preparation

Samples for various thermo-mechanical tests are produced in the three orthogonal directions XYZ, YZX, and ZXY according to DIN EN ISO/ASTM 52921. A schematic view of a sample featuring the respective building orientation adhering to the building platform is displayed in Figure 42.

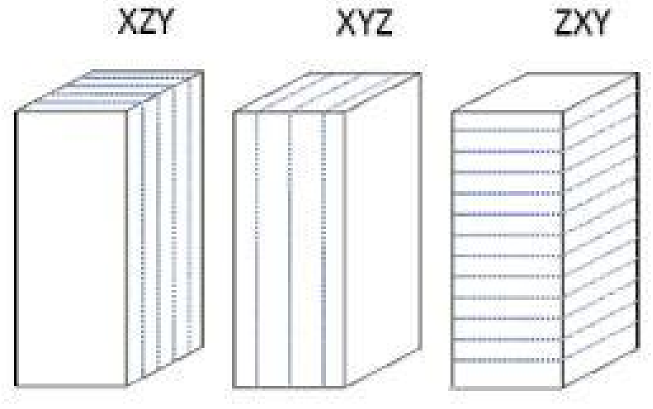

Figure 42. Illustration of the three orthogonal building directions

The raw material is a polymer composite. For the exact composition see 3.1.1 TCP I Resin. The samples are printed with the SLA printer described in 3.3.1 SLA Printer.

4.1.2 Thermo-mechanical tests

In the following sections, all mechanical and thermomechanical testing procedures are described. Apart from those measurements requiring a specific or varying testing conditions, all measurements are conducted under standard atmosphere for conditioning and testing (i.e., $t = 23$ °C, relative humidity $\varphi = 50\%$) according to DIN EN ISO 291. Additionally, all testing specimens, are post-cured in a UV floodlight device (Intelliray 600, Uvitron, West Springfield, USA) for 10 minutes. Afterwards, the samples are sanded and stored in a desiccator according to DIN EN ISO 291 after the preparation and prior to the testing.

4.1.2.1 Thermogravimetric analysis

Thermogravimetric analysis (TGA) is used to analyse the stability of the liquid components during the 3D-printing process. Small cylinders with a base area diameter of 6 mm and a height of 50 mm are printed over a duration of 20 hours. These cylinders are cut into ten sections of equivalent volume (see Figure 43).

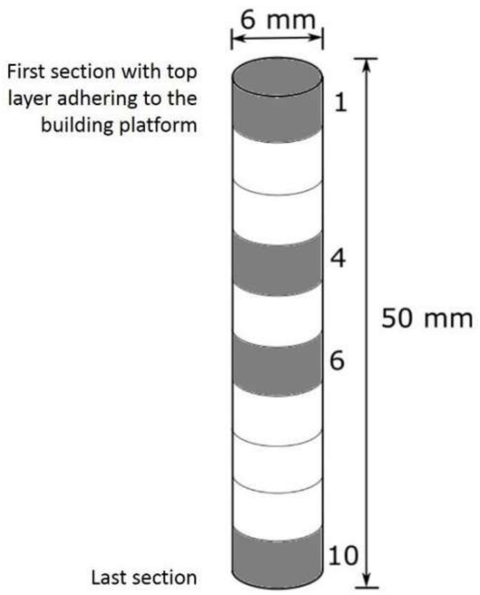

Figure 43. Cylinder for resin stability measurements.

The solid particle content of each section is measured in a TGA device (TGA 500, TA Instruments, Lukens Drive, USA) under ambient air condition. The volatilization temperature of the inorganic particles and the organic substances are significantly different. Thus, a temperature profile to thermally remove all organic parts is selected. The testing process uses a temperature rate of 22 °C/min up to a maximum temperature of 800 °C. The starting mass at 100 °C as well as the remaining mass at 800 °C are measured and the relative mass remaining in the sections is assessed. The testing cylinder is built in ZXY direction according to DIN EN ISO/ASTM 52921, hence the building time is deliberately maximized to test the stability of the liquid resin over a longer time period. In this case, the building time exceeds 20 hours which is longer than the average printing time of the other testing samples in this study.

4.1.2.2 Bending tests

Material behaviour under bending conditions is assessed using a 3-point bending testing setup. The standard specimen size used for bending tests requires 80 mm in length, which is not procurable in the present 3D-printer. Thus, smaller specimens are prepared measuring 50 mm x 25 mm x 2 mm in accordance to DIN EN ISO 178. The span width of the bearings required for these specimen dimensions is 40 mm. The samples are tested in a universal testing machine type Zwick Z050 (ZwickRoell, Ulm, Germany), until fracture occurs. A deformation rate of 1 mm/min and a preloading of 0.1 MPa are chosen to perform the tests. The bearings can be adjusted to the necessary span width. During the examination no pulling through of the samples is observed. Analysation of the data points is done by the corresponding software testXpertII (Version 3.6, ZwickRoell, Ulm, Germany).

4.1.2.3 Fracture toughness tests

Two different fracture toughness testing methods are conducted to investigate the impact strength both at low and high impact speeds. Fracture toughness under high loading rates (i.e., impact loading) is conducted using Dynstat specimens. A 3-point bending test set-up is used to investigate the fracture toughness behaviour of notched samples.

Unnotched Dynstat testing specimens according to DIN 53435 are tested using a pendulum impact tester Frank 573 (Karl Frank GmbH, Weinheim, Germany) with a 1 J hammer attached. This particular testing set-up is selected because more commonly used impact strength tests (i.e., Izod DIN EN ISO 180 and Charpy DIN EN ISO 179-1) are not feasible. These standards require bigger sample sizes, which are not producible with the present 3D-printer due to the limited dimensions of the building platform. Sample dimensions for Dynstat testing specimens are 15 mm x 10 mm x 4 mm, while Izod and Charpy testing standards require a sample length of 80 mm. Both unnotched and notched samples can be measured according to DIN 53435. Due to small sample size and micro defects arising from the 3D-printing process notching of the Dynstat testing samples is omitted to receive more robust results. The difference in height reached by the hammer, which is equivalent to the energy absorbed by the specimen is indicated by a drag indicator. The resistance of the machine originating from friction or unevenness are measured by swinging the hammer without a sample fixed in the machine. These losses are included in the assessment of the true impact strength, which is conducted manually.

SENB testing specimens are utilised to examine the fracture toughness at lower loading rates. The standard length of 3-point bending testing specimens exceeds the producible sample size limited by the building platform. Thus, sample dimensions are adapted in agreement with ISO 13586 [125]. Samples are prepared with 50 mm x 11 mm x 3.5 mm in length, width, and height respectively. The notch is created using a notching device (Notchvis 6951, Ceast, Pianezza. Italy) as well as a sharp razor blade. The initial crack length is 6.1 mm.

All SENB samples are loaded in a universal testing machine type Zwick Z050 (ZwickRoell, Ulm, Germany) until fracture occurs. The set-up used offers a minimal span width of 30 mm, which is sufficient for the dimension of the tested specimens. Individual displacement corrections for each printing direction are conducted with additional specimens according to ISO 13586. A deformation rate of 1 mm/min and a preloading of 0.15 MPa are used as testing preconditions. Data analysis is conducted via the corresponding software testXpertIII (Version 3.6, ZwickRoell, Ulm, Germany).

4.1.2.4 Hardness measurements

Specimen hardness is measured via indentation tests. Using a Vickers shaped indenter the surface hardness of the samples is assessed. Prior to the hardness measurement the samples are polished with a sample preparation machine (TegraPol-31, Struers, Willich, Germany). Thereafter, all hardness tests are performed with a HV1 set-up (M1C 010, EmcoTest, Kuchl, Austria) DIN EN ISO 6507-1. These parameters provide well-defined indentations marks, which are a necessity for the measurement of the diagonal length of the marks. The length is examined by means of optical methods. An integrated light microscopy is utilised to analyse the indentation marks manually. These measurements are prone to error to some extent. Thus, eight different indentation marks distributed on the specimen surface in accordance to DIN EN ISO 6507-1 are measured on each sample. The mean value of the diagonal lengths is taken to gain higher valid results. The position of the indentation marks on the samples is displayed in Figure 44.

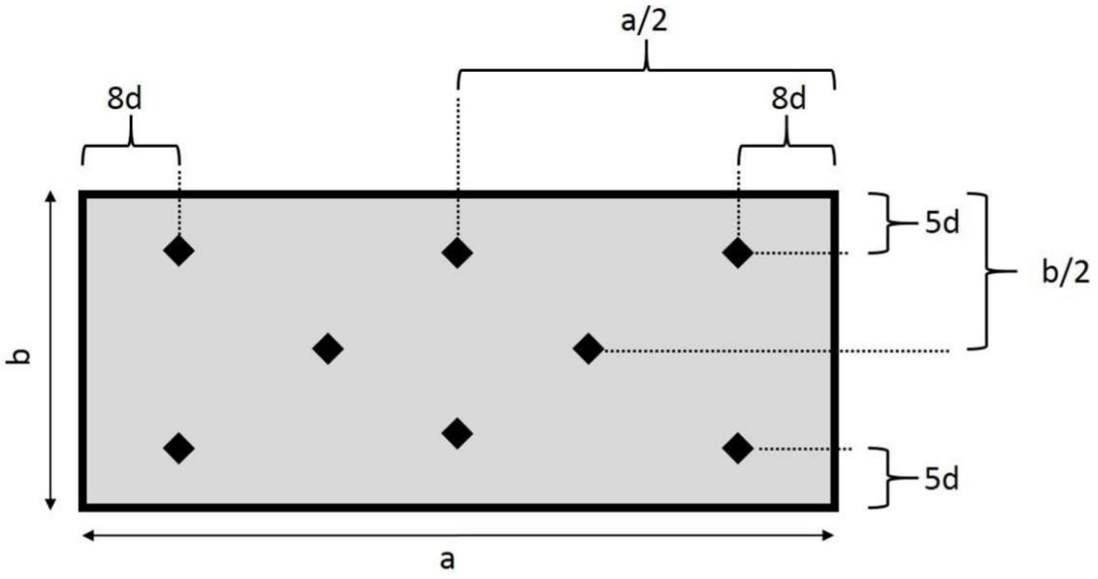

Figure 44. Positioning of Vickers indentation marks fixed by diagonal length of indentations and distance to the specimen boundaries. The distance between two adjacent marks is bigger than 10*d. [112].

4.1.2.4 DMA

The investigation of the temperature dependence of elastic properties are conducted via the DMA. A DMA 2980 Dynamic Mechanical Analysis testing device (TA Instruments, New Castle, USA) and the testing software Universal Analysis 2000 (TA Instruments, New Castle, USA) are used for sample analysation. All DMA measurements are conducted in a 3-point bending set-up. A temperature range from -50 °C to 110 °C was evaluated. First, samples are cooled to -50 °C using liquid nitrogen. Second, sample temperature is held constant at -50 °C for 5 minutes to ensure homogeneous temperature distribution in all sample regions. Third, the samples are heated up to 110 °C with a chosen heating rate of 3 °C per minute. All samples are preloaded with 0.1 N and examined at a constant frequency and amplitude of 1 Hz and 20 µm, respectively.

4.1.3 Results

The first assessment involved the verification of resin stability via TGA measurements. The results for the four sections of the testing cylinder highlighted in Figure 43 are displayed in Figure 45.

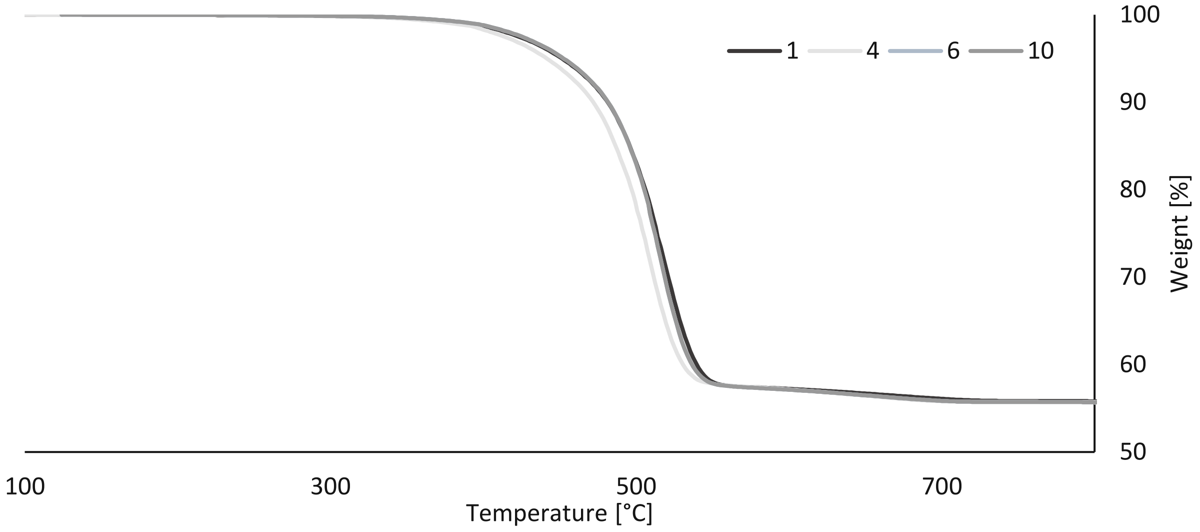

Figure 45. Results of the TGA measurements.

Clearly, all organic components are evaporated and/or decomposed thermally, only the inorganic particles remain at the target temperature of 800 °C. Characteristics of curves from all sections are almost identical, indicating similar behaviour and filler content in the entire testing specimen. Since the printing process of these cylinder exceeds 20 hours which is far more than the typical printing time for specimens in this study, stability of the liquid resin can safely be assumed.

Next, the material behaviour is assessed qualitatively to find the correct theoretical approach. The force-displacement curve of bending test samples from all three groups as well as their fracture surfaces are analysed. Figure 46 shows a representative curve of all three samples under 3-point bending conditions.

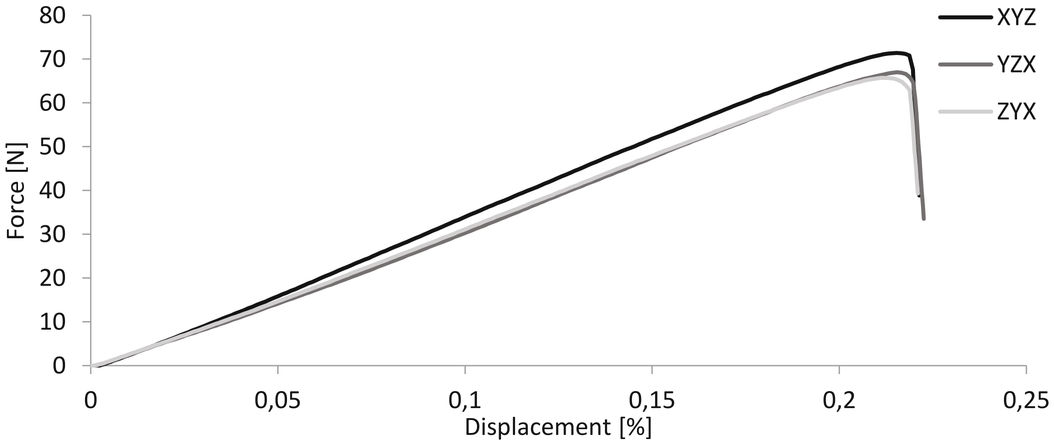

Figure 46. Representative curve of 3-point bending test specimens for each respective group [112].

Figure 47 shows the fracture surfaces of all three groups.

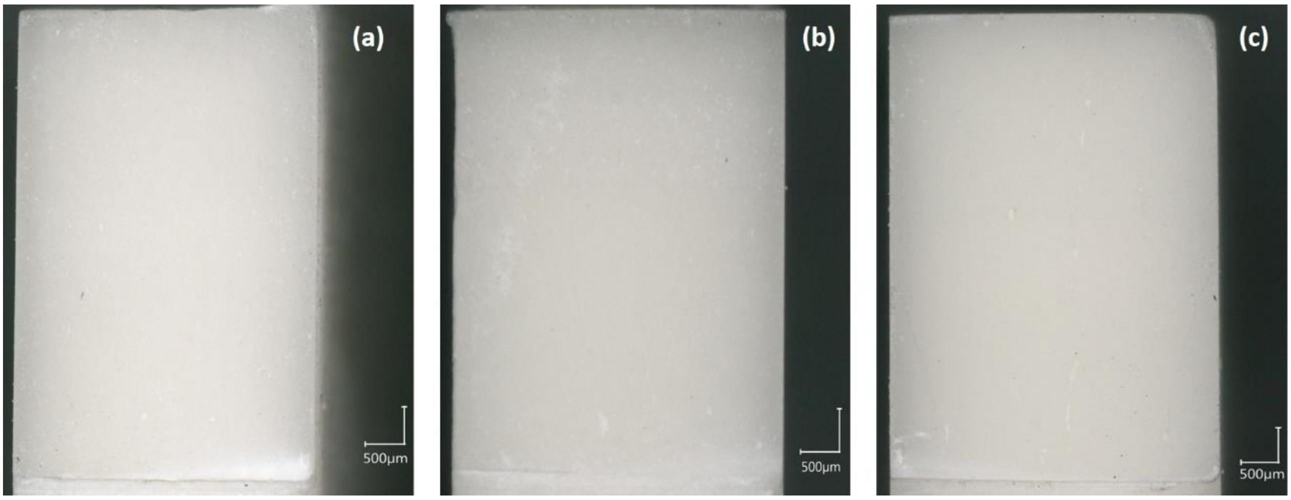

Figure 47. Figure 6. Fracture surface of 3-point bending specimens in XYZ (a), YZX (b), and ZXY (c) direction [112].

The results from both examinations complement each other. The force-displacement cures display clear linear-elastic behaviour with virtually no plastic deformation prior to fracturing. This finding is supported by the smooth and plain fracture surfaces, indicating instant crack propagation, characteristic to brittle fracture.

4.1.3.1 Fracture toughness

The almost ideal linear-elastic fracture behaviour of samples from all groups justifies the description of fracture toughness under low impact speed of SENB by means of the critical stress intensity factor K_{IC}. Calculated values for groups XYZ, YZX, and ZXY are 1.62 MPa*m(1/2) ± 0.14 MPa*m(1/2), 1.67 MPa*m(1/2) ± 0.13 MPa*m(1/2), and 1.52 MPa*m(1/2) ± 0.05 MPa*m(1/2). The results are displayed graphically in Figure 48.

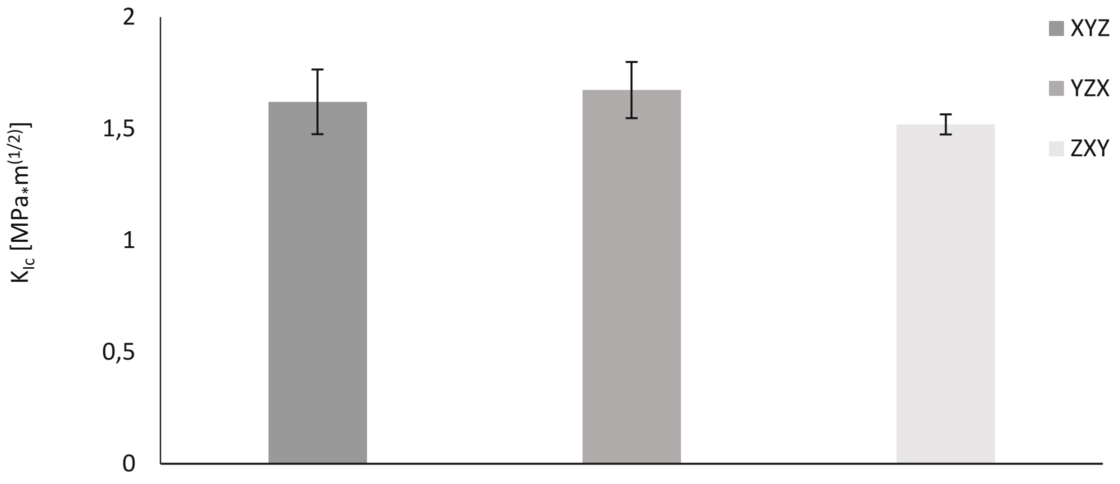

Figure 48. Influence of the building directions on the fracture toughness K_{IC} [112].

For the fracture toughness under impact speed unnotched Dynstat impact test samples are tested. The examination yields the impact strength a_{dU}. Measured mean values are 6.51 kJ/m² ± 1.27 kJ/m², 7.30 kJ/m² ± 1.76 kJ/m², and 5.76 kJ/m² ± 0.84 kJ/m² for groups XYZ, YZX, and ZXY, respectively. Means and standard deviations are displayed in Figure 49.

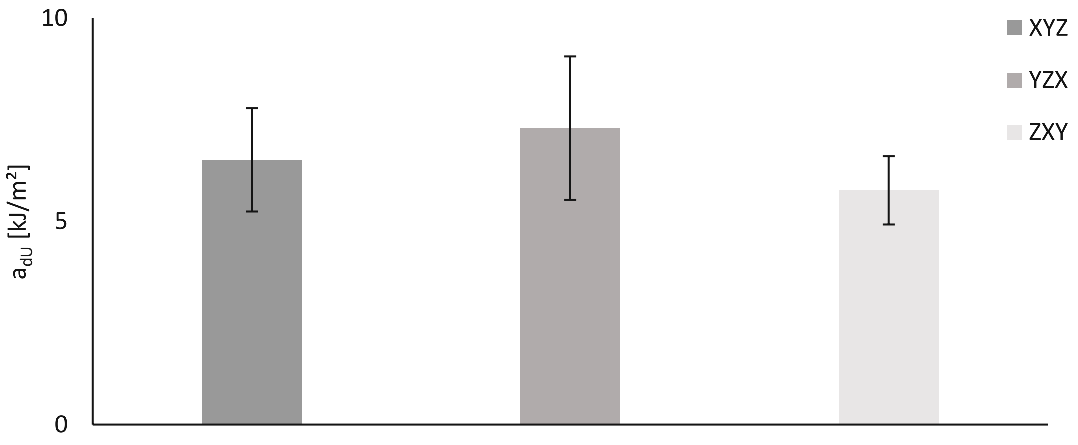

Figure 49. Influence of the building direction on the toughness under impact loading [112].

4.1.3.2 Bending behaviour

Various standard material parameters are assessed by 3-point bending tests using unnotched bending test samples. Bending modulus, bending strength, and elongation at break of theses samples are measured for all three layer orientations. The results are summarized in Table 9 and processed graphically in Figure 50.

Table 9. Summarized results of the bending tests [112].

Parameter	XYZ	YZX	ZXY
Bending modulus [MPa]	6200 ± 1020	5962 ± 1032	6175 ± 644
Bending strength [MPa]	65.4 ± 10,5	64.0 ± 8.2	60.5 ± 11.7
Elongation at break [%]	2.09 ± 0.56	1.89 ± 0.41	1.65 ± 0.56

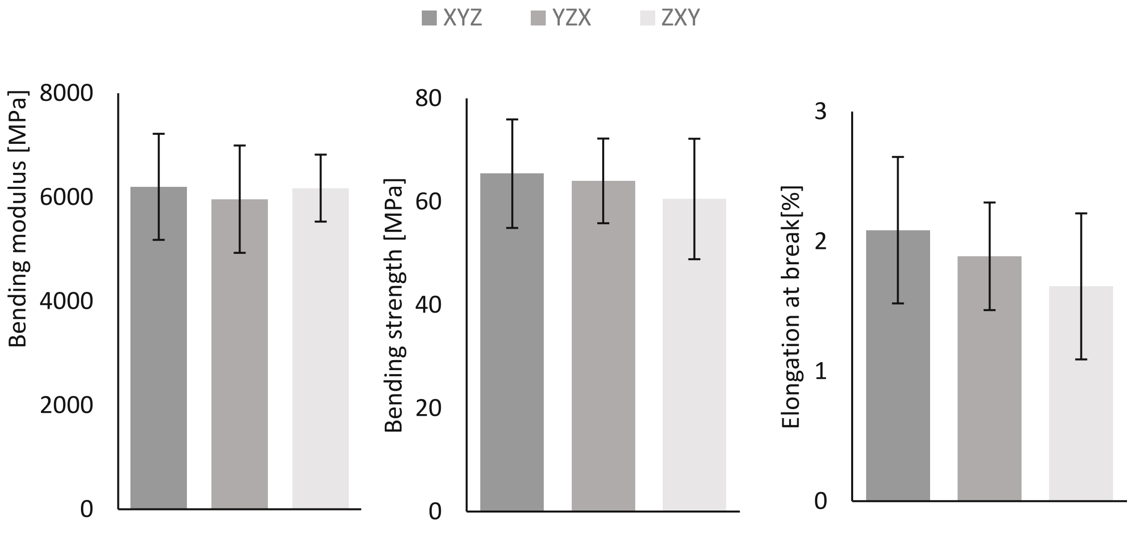

(a) (b) (c)

Figure 50. Influence of building direction on bending modulus (a), bending strength (b), and elongation at break (c) [112].

4.1.3.3 Hardness measurements

Vickers hardness is measured by indentation on eight different well-defined spots on the sanded and polished sample surface. Mean HV 1 values of eight samples per building direction are 27.5 ± 0.9 for XYZ, 27.0 ± 0.5 for YZX, and 26.4 ± 0.6 for ZXY. The results are displayed in Figure 51.

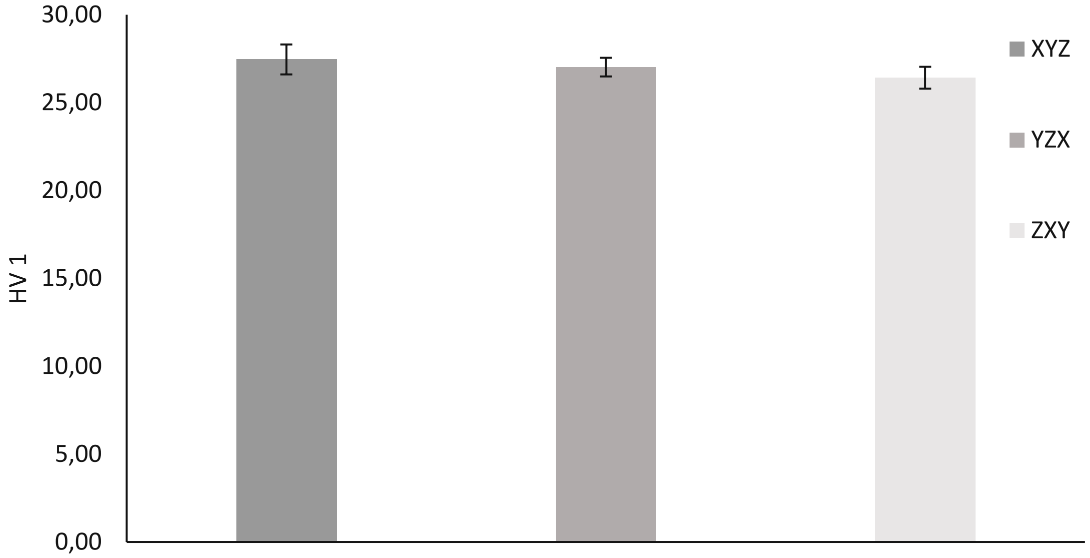

Figure 51. Influence of building directions on Vickers hardness [112].

4.1.3.4 Dynamic mechanical analysis

Dynamic mechanical analysis is conducted using two samples per layer orientation. The results for the storage modulus and *tan δ* are displayed in Figure 52.

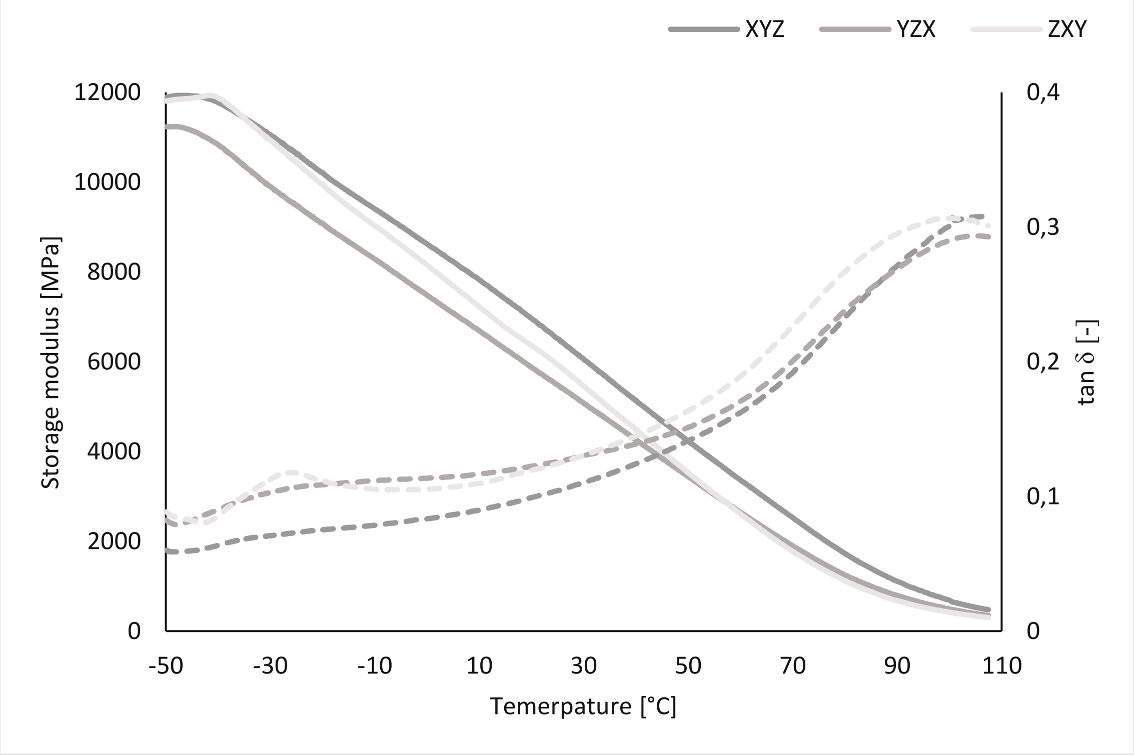

Figure 52. Results of the DMA measurements. Storage moduli (continuous line) and tan δ (dashed line) for all three sample orientations [112].

4.1.3.5 Statistical evaluation

Deeper insight in potential differences between the groups is gathered by means of statistical analysis. The mean values of all measured parameters are analysed statistically to find significant differences. The comparison of three independent groups (i.e., the three printing directions) is done by the analysis of variances (ANOVA) method. This technique compares the mean values of all dependent factors (e.g., bending strength) of all independent groups against each other to find statistically significant differences within the factors. The assessment is done by testing two hypothesis. The null hypothesis H_0, stating that there is no difference between the factors and the alternative hypothesis H_1, asserting differences between the parameters. Depending on the outcome of the test either H_0 or H_1 needs to be rejected and the other one is accepted. The level of significance (i.e., the probability to falsely reject a true H_0) for all tests is set to $p = 0.05$.

ANOVA requires normal distribution of all dependent factors as well as homogeneity of variances in these parameters. Thus, as a prerequisite these two requirements are assessed prior to the analysis with ANOVA. Normal distribution is tested via Shapiro-Wilk test which is well suited for the testing of small samples because of its high test power [126]. Homogeneity of variances is tested using the Levene test. Table 10 shows the results of the Shapiro-Wilk test and Levene test.

Table 10. Results of Shapiro-Wilk test and Levene test. * Significant difference (p= 0.05) [112].

Dependent factor	**Normal distribution (Shapiro-Wilk test)**	**Homogeneity of variances (Levene test)**
Bending modulus	0.589	0.332
Bending strength	0.236	0.286
Elongation at break	0.027 *	0.561
Dynstat impact strength	0.461	0.296
K_{IC}	0.508	0.720
HV1	0.455	0.152

The prerequisites are met for all factors with the exception of elongation at break. Thus, ANOVA is not applicable for this specific variable. Instead, the Welch-ANOVA, a more robust alternative to the conventional ANOVA is utilised for the assessment of this parameter. The Welch-ANOVA benefits from a reduced effect of non-normality and is therefore preferable in this particular case [127], [128].

The results of the statistical analysation of all factors via ANOVA and Welch-ANOVA is displayed in Table 11.

Table 11. Results of the ANOVA and Welch-ANOVA (†) showing no significant differences (p=0.05) [112].

Dependent factor	**Significance**
Bending modulus	0.068
Bending strength	0.510
Elongation at break	0.203 †
Dynstat impact strength	0.132
K_{Ic}	0.220
HV1	0.189

Clearly, no statistically significant differences between the groups (i.e., printing directions) are found in the parameters present. This is an important finding considering the examined factors represent fundamental mechanical properties of the measured specimens. Under the testing conditions determined in this study, mechanical isotropy can be safely assumed. Furthermore, DMA measurements yield similar results for the parameters storage modulus and *tan δ* for all building directions in the defined temperature range which exceeds the typical application area of these materials. Thus, the isotropic material behaviour is not affected by temperature variations. All findings strongly support the assumption of thermo-mechanical isotropy for this material.

The results impact future usage of this material in a twofold manner. First, the printing process itself can be adapted to optimize the outcome. The optimisation is performed either by producing the maximum number of parts at the same time regardless of their layer orientation. This means placing as many parts as possible on the building platform, thus maximising the sample production in one production cycle. The other optimisation approach would be to minimise the production time of a single printing job. This implies manufacturing solely the specific sample orientation requiring the least amount of layers to complete the specimen. In the present study, bending test samples produced in XYZ direction required about two hours of production time, whereas samples in ZXY direction required about 19 hours.

As a second consequence of the results from this study, anisotropy has not to be considered when printing parts with similar polymer composite materials. This implies that potential findings in following researches are not related to anisotropic behaviour and not all building directions are required to be examined. Future assessments can focus on the particular building directions of interest.

Nevertheless, generalisation of results and measured values from on specific to arbitrary layer orientation is only valid to some extent. Although ANOVA tests show no significant differences, the results from the mechanical tests vary somewhat. Especially the examination of small specimens (i.e., Dynstat) yields higher variability of results. Small impurities and voids are inevitable in layer by layer production methods, especially when processing a particle filled resin. Particle size and shape vary to some extent thus prohibiting completely homogeneous layer morphology. These production induced impurities represent potential weaknesses and starting points for cracks leading to fracture.

4.2 Bio-inspired toughening of a polymer composite

Combining strength and stiffness on one side and toughness on the other is a challenging task in engineered materials because these properties are to some degree mutually exclusive. An approach in artificially produced parts is the application of the so-called material inhomogeneity effect. This effect can be observed in naturally occurring materials such as the deep sea sponge Euplectella Aspergillum. The skeletal body of this animal is composed of cylindrical spicules ordered in a regular manner. Each single rod mainly consists of silica layers and very thin organic layers in between. Figure 53 shows the composition of the deep sea sponge’s skeleton in different degrees of detail.

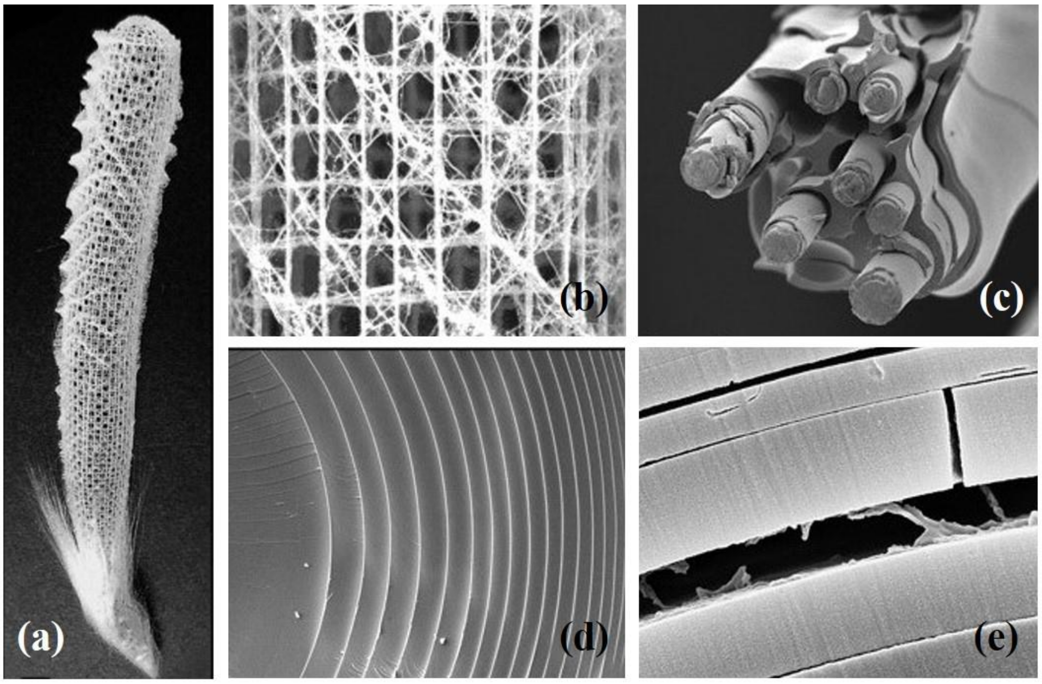

Figure 53. Structural analysis of the skeleton of Euplectella Aspergillum. Entire skeleton (a). Regular structure of the cage structure (b). Single beam of the cage showing multiple spicules inside (c). Cross-section through a single spicule. Inorganic areas (dark) are divided by thin organic layers (bright) (d). Fractured spicule displaying an organic interlayer between silica regimes (e). Adapted from [129].

Layers of silica platelets representing about 99 % of the total volume dominate the overall structure of the spicules [130]–[132]. Hence, the stiffness and strength are similar to engineered glasses. Despite the small amount of organic material, these thin layers increase the fracture toughness of this biological structure and reduce the typical inherent brittleness of glasses drastically.

The remarkable performance is achieved by these thin compliant material layers acting as crack stoppers between stiff and brittle inorganic material layers. An emerging crack is arrested inside the soft material and further propagation is prohibited [133]. This shielding of the effect is dependent on a significant and abrupt change in mechanical properties between the different layers [134]. A strong difference between typical mechanical parameters describing the stiffness and strength of materials (i.e., Young's modulus and yield strength) is essential. The minimum ratio in Young's modulus between the two different materials is 1:5. However, bigger differences are beneficial [135].

Taking an example from the build-up of the naturally occurring deep sea sponge, the shielding effect can be increased by inserting multiple soft material layers. Thus, multiple instances of crack stoppers are introduced in the material. Continuous alteration of material layers with strongly varying mechanical properties achieves the biggest toughening effect. If the thickness of both material layers is selected in an optimal manner, the fracture toughness of the engineered material can be maximised without reduction of the stiffness and strength.

This toughening technique is very appealing for 3D printing processes due to their layer-wise structuring. In conventional SLA printing, however, only one raw material can be processed at the same time. This deficiency is overcome by the usage of a hybrid printing system (see section 3.3.1 SLA Printer, 3.3.2 Inkjet system, and 3.3.3 Hybrid printing system). The combination of an SLA printing unit and an inkjet print head allows the application of two different materials in the same specimen. These materials feature strongly varying mechanical properties fulfilling the prerequisites for the material inhomogeneity effect. Hence, multi-material parts for the testing of this effect in additive manufacturing can be produced by means of photopolymerisation.

4.2.1 Sample preparation

For the composition of the two raw materials used in this study (i.e., resin and ink) see section 3.1.2 TCP II Resin and 3.2.1 Cyano Ink, respectively.

The resin is reinforced with mineral particles, giving it high stiffness and strength. This compound represents the stiff and brittle matrix material. Ink layers resemble the soft interlayers and should act as crack stoppers similar to the protein layers in the deep sea sponge. As described in 2.4.6.3 a high difference in Young's modulus between the two materials is desired to enhance the toughening effect. The minimum ratio between the two materials is 1:5. Both components are tested separately to ensure their applicability. The results of preliminary tensile tests are displayed in Table 12.

Table 12. Comparison of homogeneous materials.

Parameter	Resin	Ink	Ratio of property
Young's modulus	360 MPa	10 MPa	36
Elongation at break	3.8 %	150 %	$25 * 10^{-3}$

Thus, the ratio between the two materials clearly exceeds the minimum ratio of 1:5 and the primary design criterion for toughness improvement via the introduction of compliant material layers is met. However, the material inhomogeneity effect heavily relies on distinct areas with varying Young's modulus, that is the change in stiffness should be as abrupt as possible. Hence, any interaction between the separated layers leading to the harmonisation of the mechanical properties and consequently enlarging the interfacial area must be suppressed. Potential diffusion between the polymer layers caused by unreacted monomers or the non-reactive diluent could equalise the strong mechanical differences between resin and ink and thus deteriorate the toughening effect caused by the interlayers.

Overall layer thickness for all samples is 25 µm and controlled by the 3D printer. Although thinner layers are feasible by the 3D printer, particle size of the TCP filler prohibits thinner layers. The building platform is lowered to the vat in such a way that a gap of 25 µm in height remains. The overall vertical position of the building platform is increased by 25 µm before each curing step. For samples featuring the multi-material approach, ink layers are alternated with resin layers. Hence, the number of soft crack stopping interlayers within the sample is maximised. Ink layer thickness is calculated by ink and print head properties. The present set-up yields a resolution of 360 dpi and drop volume of 40 pl with the ink density of 1.1 g/cm³. This results in a homogeneous ink layer of thickness between 5-7 µm. Although ink layers could potentially be thinner in order to better conserve matrix properties, ensuring a continuous and homogeneous interlayer through the sample is the priority.

For the complete assessment of a potential effect, three testing groups with different compositions are produced. For the first group (A), the inkjet system is omitted and samples solely consisting of resin are built in a conventional SLA process. The second group (B) consists of a blended batch of resin and ink. The specimens for group B are built solely with the SLA system utilising the blended material in the vat. For the third group (C), alternating layers of resin and ink are solidified separately. Table 13 shows the compositions and systems used for the manufacturing of each group.

Table 13. Composition and printing systems used for each group, adapted from [114].

Group	Composition	Printing System
A	Resin	SLA
B	Resin and ink (blended)	SLA

Group	Composition	Printing System
C	Resin and ink (hybrid structure)	SLA and inkjet

Different types of testing samples are printed in the same 3D printer, utilising a single master batch for resin and ink, respectively. The vat surface temperature is held constantly at 55 °C by an electric heating device positioned underneath the vat to reduce resin viscosity which provides sufficient coating. The heating is enabled one hour before the first printing job of the day to ensure homogeneous temperature on the entire vat surface. All specimens are manufactured in XYZ orientation according to DIN EN ISO/ASTM 52921.

Resin layer thickness for groups A and B solely manufactured by DLP is 25 µm. In group C samples, an inkjet layer is added. However, the overall sample layer thickness remains at 25 µm. Thus, resin layers in group C samples are thinner than in groups A and B, reduced by the thickness of the inserted ink layer. Calculated values for sample dimensions, number of layers to gain the respective height, and layer thickness for all test specimens and groups are summarised in Table 14.

Table 14. Sample dimensions and respective layer heights for all groups [114].

Group	Sample	Length [mm]	Width [mm]	Height [mm]	Layers DLP	Layer Thickness DLP [µm]	Layers Inkjet	Layer Thickness Inkjet [µm]
A	Dynstat	15	10	4	160	25	0	0
A	Bending	40	25	2	80	25	0	0
A	DMA	25	4	2	80	25	0	0
B	Dynstat	15	10	4	160	25	0	0
B	Bending	40	25	2	80	25	0	0
B	DMA	25	4	2	80	25	0	0
C	Dynstat	15	10	4	160	19	160	6
C	Bending	40	25	2	80	19	80	6
C	DMA	25	4	2	80	19	780	6

4.2.2 Thermo-mechanical testing

Fracture toughness under impact loading is measured using unnotched Dynstat specimens according to DIN 53435, which is applicable for small sample dimensions and batch sizes (for details why this standard is used see 4.1.2 Thermo-mechanical tests). The testing is conducted using a pendulum impact tester Frank 573 (Karl Frank, GmbH, Weinheim, Germany) with a 0.5 J hammer. Samples are fixed in the testing device in a specific manner. The potential toughening effect via shielding of the soft interlayers is only feasible if the crack propagates through the layers in consecutive order. Thus, layer orientation and the direction of the applied force by the hammer must be perpendicular. The experimental set-up is depicted in Figure 54.

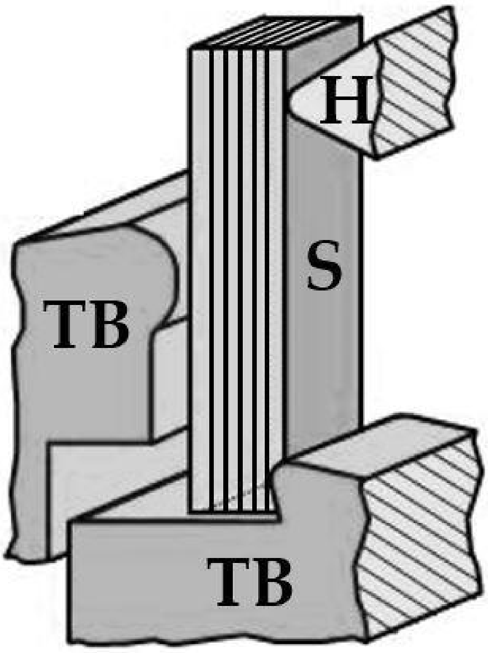

Figure 54. Dynstat impact strength test set-up for an unnotched sample (S) fixed between two thrust blocks (TB). The force applied by the hammer (H) is perpendicular to the orientation of the layers [114].

Only values from samples completely fractured by the hammer are taken into account. Eight samples per group are tested.

Samples for bending tests are built according to DIN EN ISO 178. The tests are conducted in a 3-point bending set-up with a universal testing machine type Zwick Z050 (ZwickRoell, Ulm, Germany), until total fracture occurs. Test parameters include a deformation rate of

200 mm/min and a preloading of 0.1 MPa. Data recording and analysation is done with the related software testXpertIII (Version 3.6., ZwickRoell, Ulm, Germany). Ten samples per group are tested.

Thermo-mechanical analysation is conducted via DMA. Samples for this test are produced according to DIN EN ISO 6721-1. A DMA 2980 Dynamic Mechanical Analysis testing device (TA Instruments, New Castle, USA) and the corresponding testing software Universal Analysis 2000 (TA Instruments, New Castle, USA) are used for sample analysation. All DMA measurements were conducted in a 3-point bending setup. The testing parameters are fixed to a preloading of 0.1 N and constant frequency and amplitude of 1 Hz and 20 µm, respectively. Samples are cooled to -50 °C with liquid nitrogen. This temperature is held constantly to ensure homogeneous temperature in the entire specimen. Afterwards the temperature is increased to a maximum of 110 °C with a constant heating rate of 3 °C per minute.

4.2.3 Results

4.2.3.1 Toughness under impact loading

All samples are positioned in the Dynstat impact strength testing apparatus so that the first printed layer (i.e., the layer adhering to the building platform during the printing process) faces the direction of the incoming hammer. Results from the Dynstat impact tests reveal significant differences between groups A and B on the one and C on the other side. Measured values are 2.35 kJ/m² ± 0.20 kJ/m² for group A, 2.33 kJ/m² ± 0.25 kJ/m² for group B, and 4.07 kJ/m² ± 0.72 kJ/m² for group C. The results are displayed in Figure 55.

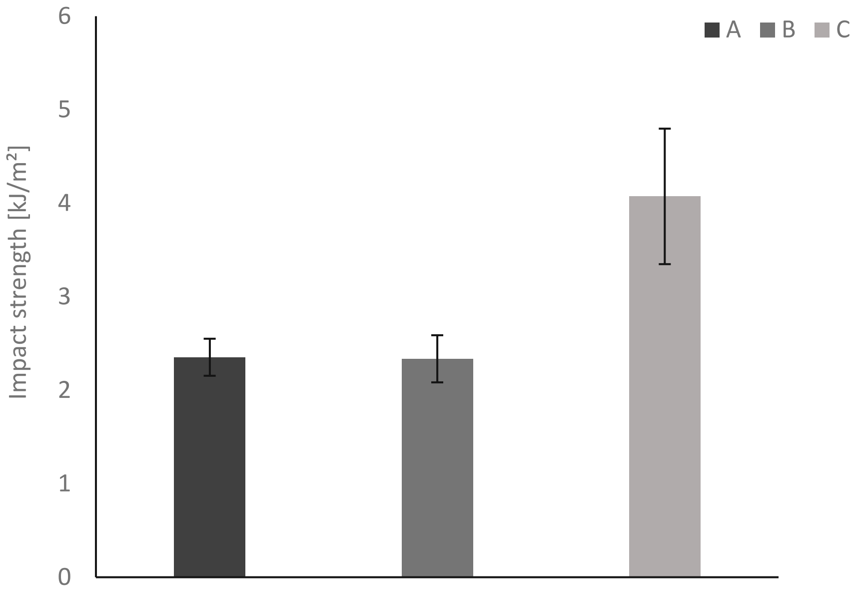

Figure 55. Dynstat impact strength tests show no differences between groups A and B and significantly higher values for group C [114].

4.2.3.2 Bending tests

All testing samples are positioned in the testing machine in such a way that the first printed layer represents the compression side of the sample. Tested values for Young's modulus, Yield strength, and elongation at break show partially significant differences between the groups. Mean values and standard deviations are summarized in Table 15 and processed graphically in Figure 56, Figure 57, and Figure 58.

Table 15. Results of the bending tests [114].

Parameter	**Group A**	**Group B**	**Group C**
Young's modulus [MPa]	353. 00 ± 33.91	347.25 ± 39.48	175.00 ± 38.41
Yield strength [MPa]	11.18 ± 0.91	10.16 ± 0.19	9.81 ± 0.21
Elongation at break [%]	3.32 ± 0.24	3.10 ± 0.24	4.05 ± 0.45

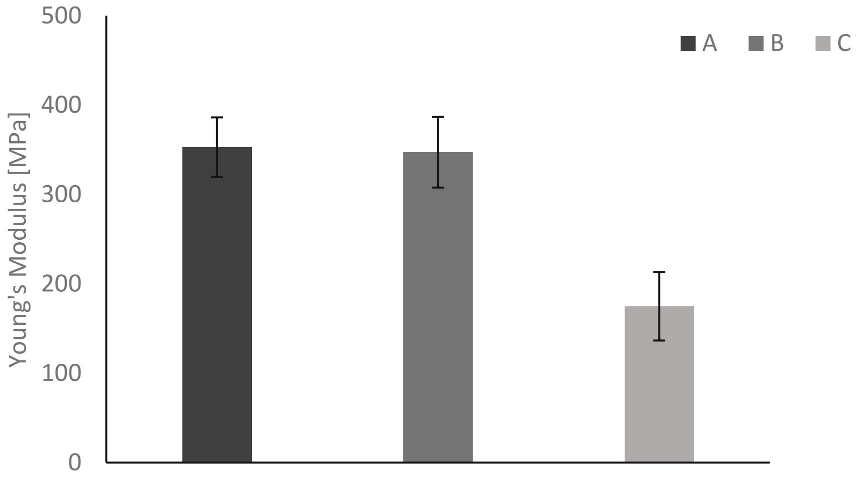

Figure 56. Bending tests clearly show a reduction in Young's modulus for group C samples [114].

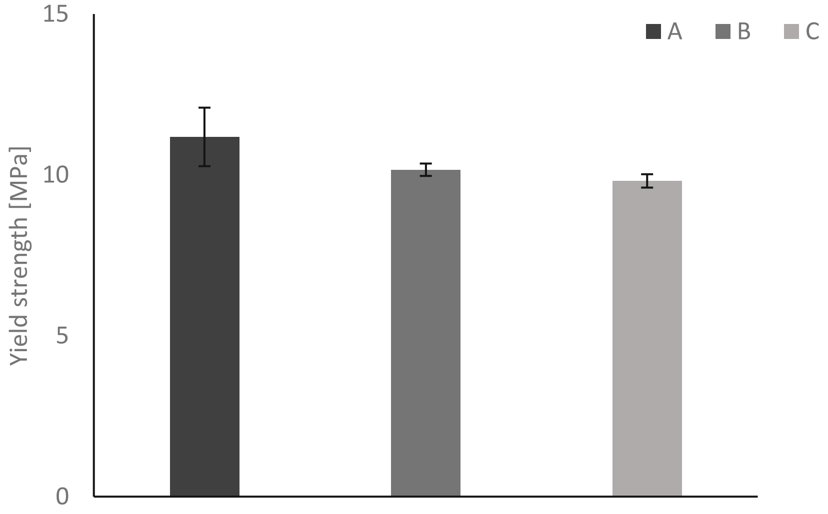

Figure 57. Bending tests yield a slight decrease in yield strength for group C samples [114].

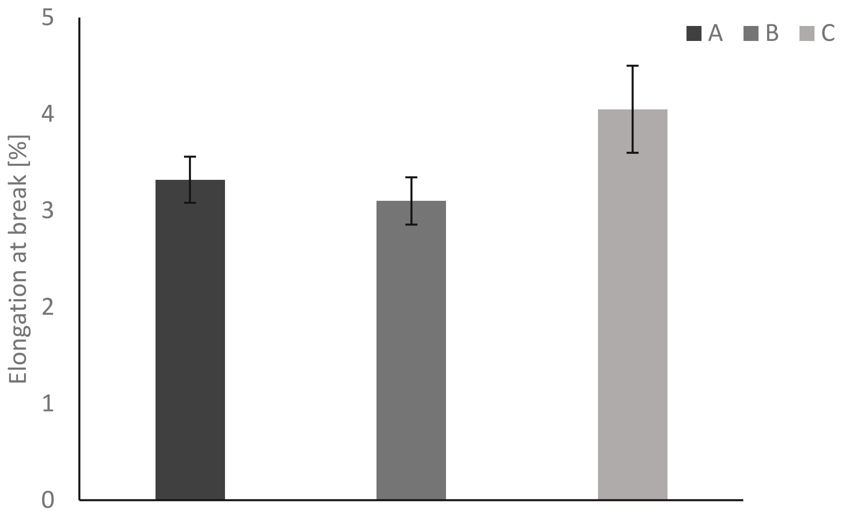

Figure 58. Bending tests reveal a significant increase in elongation at break for group C samples [114].

4.2.3.5 Statistical evaluation

Deeper analysation of the quantitative data from Dynstat impact and bending tests is conducted via statistical analysis. The primary objective of this process is to confirm differences observed in the testing procedure in a statistical manner. Hence, the ANOVA is conducted to find significant differences between the three testing groups. This is done in a three-step process. First, the prerequisites of the ANOVA are tested (i.e., normal distribution of dependent factors, homoscedasticity). Second, the ANOVA or its alternatives are performed and third post-hoc tests are conducted to decisively state where the found differences are located (see 4.1.3.5 Statistical evaluation). The level of significance is set to $p = 0.05$.

Normal distribution is tested by the Shapiro-Wilk test appropriate for the testing of small samples. Homogeneity of variances is tested via the Levene test. Results from these two tests are summarized in Table 16.

Table 16. Results of Shapiro-Wilk test and Levene test. * Significant difference (p= 0.05).

Dependent factor	**Normal distribution (Shapiro-Wilk test)**	**Homogeneity of variances (Levene test)**
Dynstat impact strength	0.008 *	0.056
Bending modulus	0.140	0.742

Dependent factor	Normal distribution (Shapiro-Wilk test)	Homogeneity of variances (Levene test)
Bending strength	0.092	0.210
Elongation at break	0.150	0.478

The prerequisites are met for all factors with the exception of Dynstat impact strength. Normal distribution of all values within this parameter cannot be assumed. Thus, the ANOVA procedure is not applicable for this specific variable. A more robust alternative to the conventional ANOVA is the Welch-ANOVA.

The results of the statistical analysation of all factors via ANOVA and Welch-ANOVA are displayed in Table 17.

Table 17. Results of the ANOVA and Welch-ANOVA (†). * Significant differences (p=0.05).

Dependent factor	Significance
Dynstat impact strength	0.009 * †
Bending modulus	0.000 *
Bending strength	0.006 *
Elongation at break	0.000 *

The analysation yielded significant differences within all dependent factors. However, these procedures give no further information about the pairwise differences between the groups. Thus, the Bonferroni post-hoc test is conducted to find specific information about the pairwise variation of the groups. The results of this test are depicted in Table 18.

Table 18. Results from the Bonferroni post-hoc test specifying the differences between the groups.

Dependent factor	Group	Groups	Significance	Mean difference
	A	B	1.000	0.01672

Dynstat impact strength		C	0.001 *	-1.72015
	B	A	1.000	-0.01672
		C	0.001 *	-1.73687
	C	A	0.001 *	1.72015
		B	0.001 *	1.73687
Young’s modulus	A	B	1.000	-21.00000
		C	0.000	178.00000
	B	A	1.000	21.00000
		C	0.000 *	199.00000
	C	A	0.000 *	-178.00000
		B	0.000 *	-199.00000
Yield strength	A	B	0.019 *	1.35000
		C	0.013 *	1.44500
	B	A	0.019 *	-1.35000
		C	1.000	0.09500
	C	A	0.013 *	-1.44500
		B	1.000	-0.09500
Elongation at break	A	B	1.000	0.11258100
		C	0.001 *	-.95318067
	B	A	1.000	-0.11258100
		C	0.001 *	-1.06576167
	C	A	0.001 *	0.95318067
		B	0.001 *	1.06576167

Summarising the data displayed in Table 18, it can be seen that group C samples differ in every factor from the other two groups except for yield strength. Complementary to that, groups A and B show no significant differences between them except in yield strength. Generally speaking, group C samples show significantly higher impact strength as well as elongation at break than the other two groups. These two findings support each other, since higher elongation at break arises from bigger deformation prior to failure. Complementary, the ability for bigger deformation without cracking results in higher toughness. On the flip side, group C samples show significantly lower stiffness (i.e., factor Young’s modulus) than the other two groups. Moreover, the yield strength in samples from the former group is significantly lower than the yield strength of parts produced out of pure resin. Thus, samples from groups A and B display quite similar behaviour while samples from group C exhibit higher impact strength and deformation before cracking which is accompanied by reduced strength and stiffness.

4.2.3.3 DMA

Temperature dependent material behaviour is analysed via DMA. Mean curves of storage modulus and tan δ for two samples of each group are depicted in Figure 59.

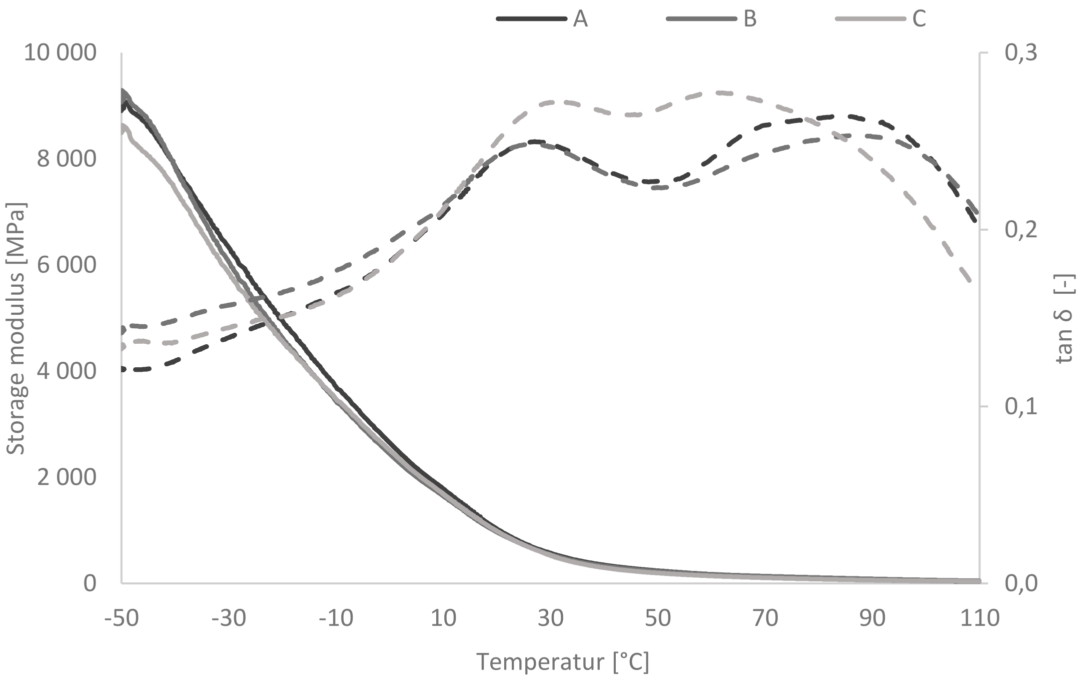

Figure 59. Results of DMA measurements. Means of storage modulus (continuous) and *tan δ* (dashed) for sample of all groups [114].

4.2.3.4 Optical analysis

Digital microscopy imaging of the cross section of fractured samples clearly shows differences of samples from group A and B on the one hand and group C on the other. The cross section of a sample from each group is depicted in Figure 60.

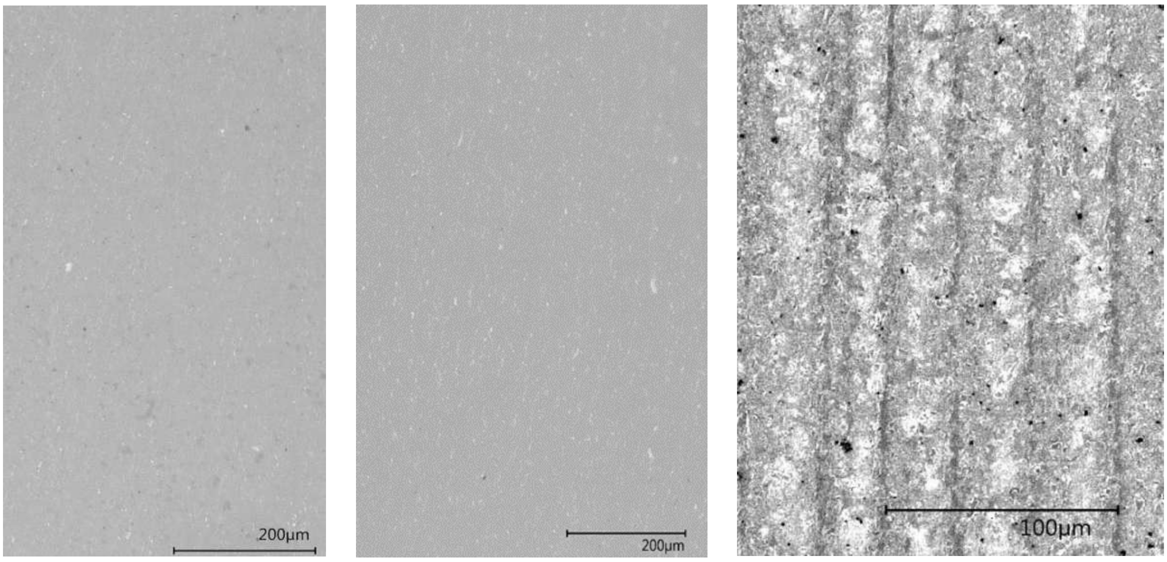

(**a**) (**b**) (**c**)

Figure 60. Digital microscopy imaging of the cross sectional area. Samples from group A (a) and B (b) appear homogeneous. Separated resin and ink layers are visible in group C samples (c) [114].

Small defects arising from the manufacturing process (i.e., white dots) are visible in group A and B samples. Apart from this feature no indication of the layer wise build up is recognisable. In samples from group C singular lines (i.e., resin layers separated by ink layers) are visible.

Light microscopy imaging of the cross section of a group C sample further verifies the existence of separate material layers (see Figure 61).

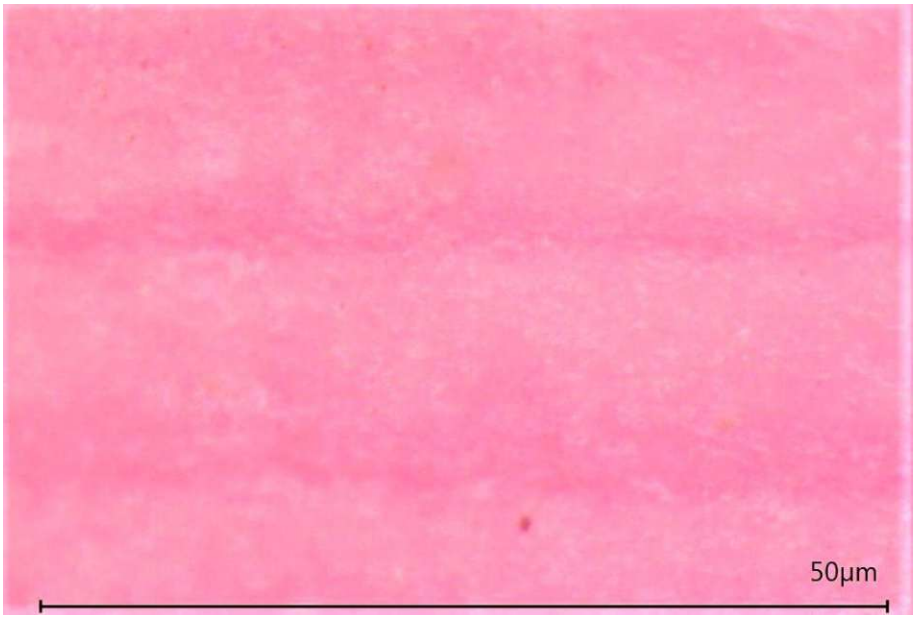

Figure 61. Coloured cross section of a group C sample. Ink layers (thin dark lines) are visible between brighter resin layers [114].

Aside from the existence of ink layers, another undesired effect is apparent. The red colouring agent is solely added to the ink component. Nevertheless, all parts of the specimen appear in a somewhat light red or pink colour. This indicates a form of diffusion process between the material layers after the manufacturing.

Further verification of separate material layers is conducted via scanning election microsope (SEM) imaging in combination with EDX for group C samples. Results of these measurements are depicted in Figure 62.

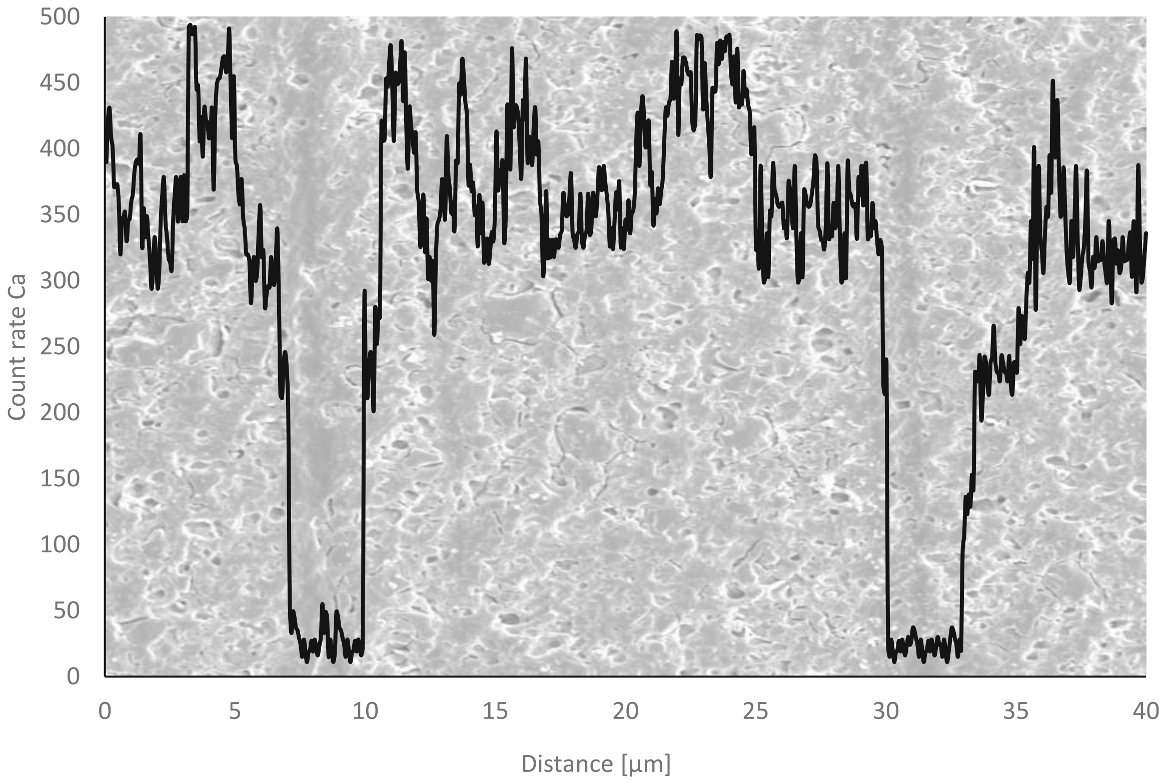

Figure 62. SEM image of a group C sample. Count rate for Ca equivalent to the Ca content in this region is decreased in the area of ink layers [114].

The *Ca* count rate indicated the amount of calcium in a certain area. This element is characteristic for the resin component filled with TCP particles. However, calcium is totally absent in the ink component. Hence, the periodic decrease in calcium verifies the existence of separate ink layers.

The study present yields multiple results. The findings as well as their impact will be discussed in the following. The first major result of this research is the fact that the methodological approach could be taken process-wise and that the approach yielded proper results. The prototype of the hybrid printing system used in this examination allows the application and connection of two separate materials via light induced polymerisation. Optical methods as well as SEM imaging in combination with EDX verify the existence of somewhat separate ink layers characterised by an absence of calcium (i.e., TCP particles). Furthermore, the production of 3-dimensional parts with distinct morphology is possible. Additionally, the impact of the material inhomogeneity effect is clearly visible and statistically relevant. The impact strength of samples featuring separate material layers is increased by about 70%. Higher capability of deformation (i.e., elongation at break) of these samples compared to the other groups in bending tests correspond with the former results. Nevertheless, the ultimate goal, namely the increase of fracture toughness while conserving the initial strength and stiffness (i.e., properties of the pure resin) is not achieved. Samples with alternating material layers suffer a loss of about 50% in Young's modulus and 12% in yield strength compared to pure resin samples.

Another remarkable result is that there are only minor differences between groups A composed of solely resin and B resembling the blend. The addition of small amounts of soft ink component prior to the manufacturing process has little impact on the overall performance. The only statistically significant effect is the reduction of the yield strength in blended samples compared to pure resin samples, which is reasonable. More importantly this finding clearly shows that the increase in impact strength arises from the separate material layers present in samples from group C and consequently from the proper application of the material inhomogeneity effect.

DMA sheds light on the temperature dependency of samples in a range between -50 °C and 110 °C. The overall characteristic of the curves from all groups are similar indicating no substantial change in the temperature dependent performance. Minor differences are still visible. The maximum of *tan δ*, corresponding to the glass transition temperature is at around 85 °C for groups A and B and reduced in group C to 62 °C. Typically, engineered parts produced with this method are used below their glass transition temperature. Hence, these findings slightly reduce the application range. However, in the temperature range between 20 °C and 70 °C, the *tan δ* curve of group C samples lays clearly above the respective ones from groups A and B. This indicates more energy dissipation in group C samples which supports the findings of increased impact strength. DMA yields similar curve characteristics and values for the storage modulus, connected to the elastic properties, at room temperature (i.e., 25 °C). Although these findings do not correspond with the results of the bending tests revealing significantly lower Young's modulus in samples from group C these values cannot be directly transferred. The results are in frequency domain and thus require extensive additional measurements and transformation to be comparable to other results in time domain. Overall, DMA measurements support the findings from the other mechanical tests.

Apart from the undesired decrease in some mechanical parameters, optical analysis reveals another concerning result. Although only the ink component is stained with red colour all parts of the sample appear in red or pink colour in light microscopy. Hence, some form of diffusion process is occurring resulting in the colouring of all parts of the sample. The actual diffusion of colouring agent is only the most obvious change in macroscopic properties but the fact that diffusion between the material layers is present represents a major challenge. A reasonable explanation for the diffusion process are unreacted monomers in the finished part diffusing through the sample. This movement of material leads to a partially harmonisation between the properties of the different materials in the separate layers. Since the toughening effect of the material inhomogeneity approach strongly depends on large differences in the mechanical properties between the materials, this diffusion process reduces the overall effect. The shielding effect applies in the transition area of two materials, where a significant change in mechanical properties should occur.

Hence, future usage of the hybrid printing system depends on the reduction or full suppression of diffusion processes to increase the toughening effect while also conserving the initial strength and stiffness. This challenge can be tackled by adapting the raw materials of the two components (e.g., increase the reactivity of the polymeric systems) as well as the solidification processes itself. Nevertheless, this study yields promising results showing the potential of a different toughening approach than typical approaches (e.g., core-shell particles, liquid rubbers). This two-component system allows the selective adaptation of mechanical properties without changing the composition of the main matrix component.

4.3 Application of the hybrid printing system to enhance fracture toughness

Primary results using the hybrid printing system consisting of separate SLA and inkjet printing production systems merged into one 3D printing unit display the great potential of this new approach (see 4.2 Bio-inspired toughening of a polymer composite). The fracture toughness of polymer composite materials is increased significantly. Thus, a fundamental disadvantage of inherently brittle raw materials can somewhat be circumvented. Nevertheless, the ultimate goal of totally conserving the stiffness and strength of the original material is not met. Hence, various adaptations are made in the follow-up study. First, the raw materials are changed to increase the performance. Second, the printing pattern as well as the examination methods are altered to gain deeper insight in the mechanisms present in the manufactured specimens. The basic idea of the application of the material inhomogeneity effect as the underlying phenomenon persists, however. The impact of this effect is strongly dependent on the continuous alteration of the mechanical properties in the specimen. The layer-wise structure fundamental to all 3D printing processes is naturally suited for the application of this phenomenon. The key idea is the improvement of important mechanical properties (i.e., elongation at break, fracture toughness) without compromising others. Small defects arising from the production process itself or the handling of the parts are potential challenges, since they might be the origin of material failure. Under load, these micro cracks can grow and form bigger cracks propagating through the specimen. Ultimately, this leads to total failure and destruction of the part.

The crack initiation is strongly dependent on the geometry of the crack, particularly on the shape of the crack tip. The radius at the crack tip and its curvature determine the stress at the foremost point of the crack. Thus, blunting of the crack tip to increase the radius and consequently reduce the applied stress at the tip is a key aspect in increasing the fracture toughness [136].

Depending of the material's response to an external load and the failure mechanisms, the fracture behaviour can be described by various theories. Considering completely linear-elastic fracture behaviour without plastic deformation, the fracture toughness can be assessed by the stress intensity factor K_c (see 2.4.6.2 Basic concepts of linear elastic fracture mechanics). However, if the tested specimens display some form of plastic deformation prior to fracturing, a different theoretical approach must be taken. In case of a small area of plasticification in front of the crack tip where plastic deformation occurs, the fracture toughness can be described by the nonlinear-elastic fracture theory. The fracture toughness of materials displaying this behaviour is given by the parameter J_c derived from the concept of J-Integral (see 2.4.6.2 Basic concepts of linear elastic fracture mechanics).

4.3.1 Sample preparation

Two separate materials (i.e., ink and resin) are used to produce the parts with the desired composition. The compositions are displayed in detail in 3.1.3 TCP III Resin and 3.2.2 Tango Ink.

Samples for mechanical tests are produced in the two orthogonal directions XYZ and YZX according to DIN EN ISO/ASTM 52921. For the sake of simplicity, groups featuring these layer orientations are labelled with X and Y, respectively. Samples featuring alternating material layers of resin and ink (i.e., testing group) and specimens consisting solely of resin (i.e., control group) are prepared in both building directions. To account for this distinction the first group of samples is labelled with T, while the latter is labelled with C. Composition, building direction, and labelling of all groups is displayed in Table 19.

Table 19. Labelling, building direction, and composition of all groups.

Name	Building direction	Composition
XT	XYZ	Resin and ink
XC	XYZ	Resin
YT	YZX	Resin and ink
YC	YZX	Resin

The layer height for pure resin layers is 50 µm and for pure ink layers about 12 µm. Naturally, the macroscopic geometry of all samples for one specific testing method must be constant, regardless of the manufacturing technique. Hence, there are differences in thickness and amount of layer between the varying groups. Additionally, the necessary specimen height depends on the building direction of the samples (i.e., the orientation of the specimens with regard to the vertical axis of the 3D printer). The number of layers as well as the layer thickness and the achieved height for samples of all groups are displayed in Table 20.

Table 20. Number of layers and layer thickness for all groups.

Name	Resin layers	Ink layers	Total layers	Thickness resin layers [µm]	Thickness ink layers [µm]	Required height [mm]
XT	80	80	160	42	8	4
XC	80	0	0	50	0	4
YT	200	200	400	42	8	10
YC	200	0	200	50	0	10

4.3.2 Testing

If no specific information is given, all mechanical tests are conducted under standard testing conditions (i.e., room temperature, humidity). Prior to all tests, samples are stored in a desiccator according to ISO 291.

4.3.2.1 Preliminary tests

The particle size and the respective distribution is analysed using a laser diffraction device (Mastersizer 2000, Malvern Panalytical, UK).

The Young's modulus of both raw materials (i.e., resin and ink) is tested separately. A ratio of at least 1:5 is the lowest threshold required for the material inhomogeneity effect to be effective. Bigger differences are beneficial, however.

Soft materials featuring very low stiffness cannot be measured using a bending test set-up. The compliant material behaviour in conjuncture with the testing geometry yields no valid results. The combination of applied compressive and tensile forces leads to specimen movement during the deformation process. The contact area between testing specimen and bearing is constantly reduced resulting in a slipping of the specimen prior to fracture. This phenomenon prevents the assessment of fracture related properties (e.g., elongation at break) and distorts other characteristic values examined before fracture (e.g., Young's modulus, bending strength). Thus, these materials are examined by tensile testing. This set-up yields appropriate values through clamping of the samples on both sides. All samples are produced according to DIN EN ISO 527-2. 10 Type 5B samples sample per raw material are produced. The samples are tested in a universal testing machine type Zwick Z050 (ZwickRoell, Ulm, Germany), until fracture occurs. A clamping length of 18 mm is set at the start. A preloading of 0.1 MPa and a deformation rate of 5 mm/min are selected. Results are analysed with the corresponding software testXpertII (Version 3.6, ZwickRoell, Ulm, Germany).

Liquid viscosity of both the resin and the ink component is measured using a rheometer (MCR 300, Anton Paar, Austria). Viscosity of the raw materials must be sufficiently low to ensure proper processing during the printing process. Adequate resin viscosity is required for homogeneous coating resulting in a solidified layer with constant height. Low resin viscosity is fundamental for the generation of inkjet droplets and the creation of the jetting pattern. 80 µL of each material is placed in the machine with a chosen gap of 48 µm between top and bottom plate. First, the temperature is measured at 25°C for 60 s. Then the temperature dependent viscosity is measured by increasing the temperature constantly between 25 °C and 75 °C.

4.3.2.2 Fracture mechanics tests

For the investigation of fracture mechanics behaviour at low speed, 3-point bending specimens according to DIN EN ISO 178 are printed. In agreement with DIN EN ISO 178, standard dimensions for these specimens are adapted to 55 mm x 10 mm x 4 mm. This is the maximum geometry feasible with the present 3D printer due to limited space on the building platform.

After the building process, the samples are cleaned manually and post-cured in a UV chamber equipped with a UV flood light (Intelliray 600, Uvitron, USA). Thereafter, a notch is created in a two-step process in agreement with ISO 13586. First, a notching device (Notchvis 6951, Ceast, Italy) is utilised to notch the sample coarsely. Second, a fine notch tip is produced by tapping a sharp razor blade into the pre-notch.

Fracture mechanics tests are conducted using a universal testing machine (Zwick Z050, ZwickRoell, Germany) in a 3-point bending setup. The samples are loaded until total fracture occurred. The span width between the rollers is 40 mm. A deformation rate of 1 mm/s and a preloading of 0.15 MPa are selected. The initial crack length (i.e., crack created by the notching device and the tapping of the razor blade) is 5.5 mm. Individual displacement corrections for each printing direction are performed with an additional unnotched specimen of each group according to ISO 13586. 10 Samples per group are measured. Data analysis is done with the corresponding testing software (testXpertIII, Version 3.6, ZwickRoell, Germany).

The variation in the building direction between groups XT and XC on the one hand and YT and YC on the other lead to a difference in layer orientation in the samples with regard to the initial crack and the clamping in the testing machine. The testing set-up for all groups is displayed schematically in Figure 63.

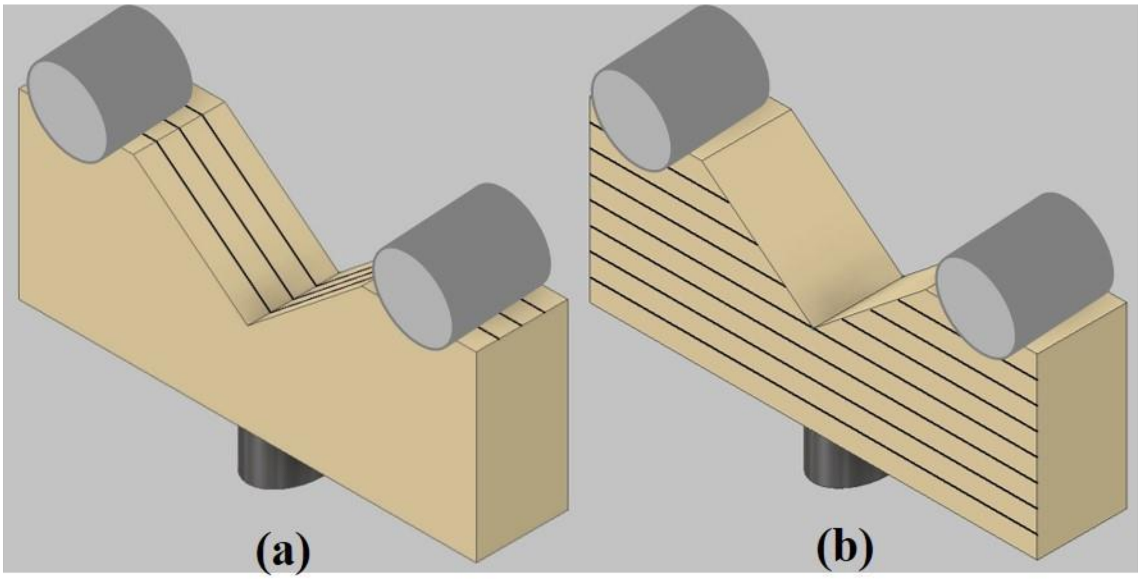

Figure 63. Schematic view of the 3-point bending test setup (dark objects symbolize rollers) with respect to the layer orientation (i.e., dark lines) of groups XT and XC (a) as well as YT and YC (b).

The quantitative examination of the fracture mechanical results for these samples are conducted in accordance with ISO 13586 and the testing protocol by Hale and Ramsteiner [137]. These protocols allow the analysation of samples displaying a limited amount of plastic deformation prior to fracturing. The resistance to critical crack growth is described by *J*. In case of small crack extensions, a preliminary value J_0 can be calculated via

$$J_0 = \frac{\eta U}{B * (W - a_0)}, \qquad \text{(XXVIII)}$$

where J_0 is the fracture resistance not allowing uncontrolled crack growth, η is a geometry parameter (i.e., 2 for the present samples), *U* is the area under the load versus load-point displacement curve, *B* is the thickness of the specimen, *W* is the specimen width, and a_0 is the initial crack length [137]. However, this formula is only appliable if the maximum crack extension is small compared to the uncracked ligament (i.e., the remaining pristine width of the sample).

$$\Delta a_{max} \leq 0.1 * (W - a_0) \qquad \text{(XXIX)}$$

In the present study, the soft ink layers are distributed throughout the sample to maximise the impact of the material inhomogeneity effect by continuous alteration of the materials. Thus, the full effect of all interlayers can only be assessed by complete failure of the sample (i.e., fracturing). However, this implies that the requirement of small crack extensions (XXIX) is not satisfied and the that (XXVIII) cannot be applied.

(XXVIII) has to be corrected to correctly assess the fracture toughness *J* via

$$J = J_0 * \left(\frac{(0.75\eta - 1)\Delta a}{W - a_0} \right), \qquad \text{(XXX)}$$

where Δa is the current crack extension [138].

This adaptation requires the continuous measurement of the current crack length during the examination. This task is fulfilled by filming the sample from a frontal view during the whole assessment. A digital camera (AxioCam, ERc5s, Zeiss, Germany) is attached to a light microscope (Axioscope, Zeiss, Germany). The microscope is focused on the front side of the sample. Proper magnification is selected to allow the recording of the complete fracturing process (i.e., crack tip and whole uncracked ligament are visible). The camera records with a resolution of 25 frames per second. Length measurements are only possible if the system is calibrated correctly. A calibration scale of known length is positioned in the front plane of the sample inside the testing device, before the measurements.

4.3.2.3 Optical analysis

Optical analysis is conducted to ensure the correct build-up of samples from groups XT and YT. Separate material layers are essential for the material inhomogeneity effect. Hence, a laser scanning confocal microscope (LSM 700, Zeiss, Germany) at a wavelength of 555 nm is utilised to verify the existence of separate material layers. The selected wavelength matches the absorption spectrum of the colouring agent (i.e., Rhodamine B), thus triggering emissions [139].

The initial crack length of each sample is measured with a digital microscope (VHX-6000, Keyence, Japan) with a magnification of 200.

4.3.2.4 Nanoindentation

Micro indentation measurements are conducted to confirm the existence of separated material layers. This technique uses a Vickers shaped indenter to penetrate the sample surface. Continuous recording of hardness, Young's modulus, and penetration depth allows to assess the location of materials with varying mechanical properties.

4.3.3 Results

Particle size distribution measurements show a mass-median-diameter of 8.8 µm. Particle diameters vary between 2.0 µm and 31.7 µm. Hence, the minimum layer thickness for resin layers containing TCP particles must be bigger than 31.7 µm to ensure proper layers with smooth surfaces.

Preliminary tensile tests conducted with pure resin and ink specimens reveal substantially different values in Young's modulus and elongation at break. Measured values for these parameters are 6100 MPa ± 824 MPa and 3% as well as 0.0086 MPa ± 0.0005 MPa and 175% for pure resin parts and pure ink samples, respectively. Although these absolute values are derived from moulded parts and can thus not be compared to 3D printed parts the large difference is in very good agreement with the expected values. A difference in Young's modulus in the magnitude of 10^6 not only meets the minimum criterion for the application of the material homogeneity but exceeds it in a beneficial manner.

Liquid viscosity assessments of the raw materials conducted by Bettina Koch yield divers results. Viscosity of the resin is 70 mPa*s at 25 °C which is sufficiently low for the application in the DLP system. Homogeneous coating and layer thicknesses can be guaranteed at room temperature. Measured ink viscosity, however, is 106 mPa*s at 25 °C. This renders the ink unusable in the present inkjet system at room temperature. Ink viscosity must be in the range of 10 – 20 mPa*s to be jettable and proper droplet formation is possible. A temperature profile is compiled to find a temperature range in which the viscosity is low enough to provide an applicable raw material. The results are displayed in Figure 64.

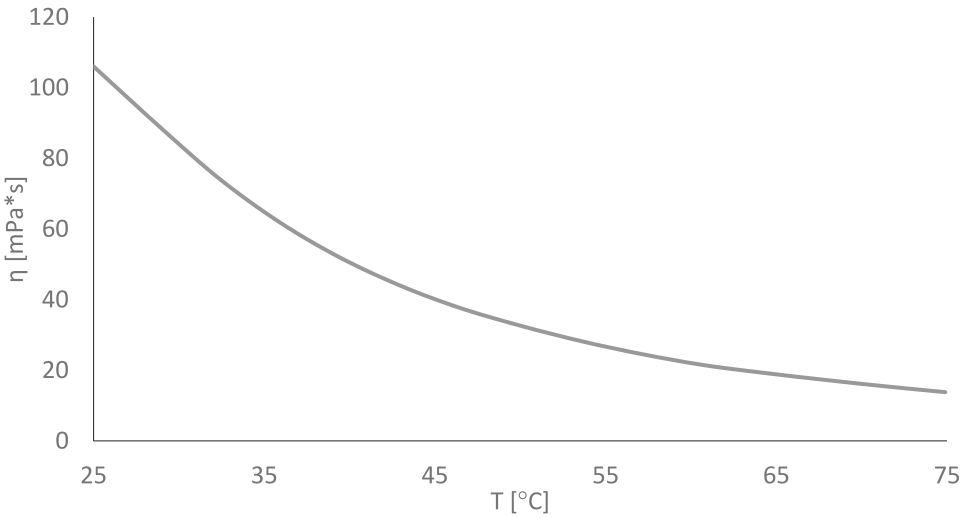

Figure 64. Temperature profile of pure ink viscosity.

Measured viscosity values are 15.5 MPa*s at 71.3 °C and 13.8 MPa*s at 74.9 °C. Hence, the heating temperature in the inkjet system is set to 75 °C to ensure sufficiently low ink viscosity.

In the first step of the fracture mechanical analysation, the correct methodological approach for the description of the fracture behaviour has to be found. The force displacement curves of samples from all groups are analysed qualitatively. Representative curves of samples from all groups are displayed in Figure 65.

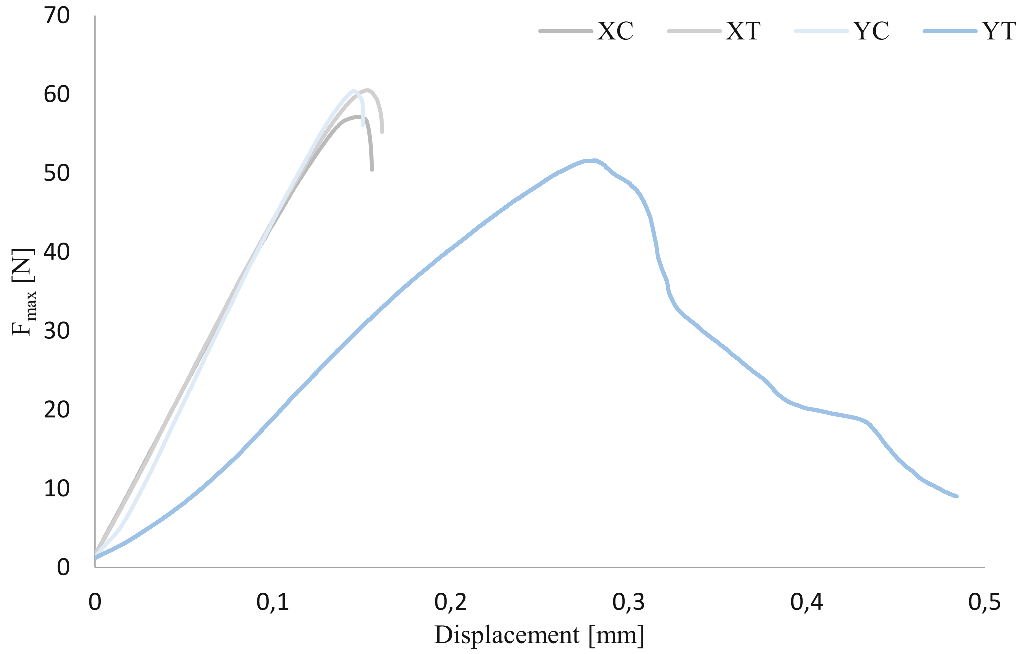

Figure 65. Force-displacement curves of SENB samples from all groups displaying significant differences prior to total failure.

Clearly, samples from groups XC, XT, and YC show a somewhat similar fracture pattern, while YT samples display a substantially different behaviour in the test. The first three groups similarly show close to ideal linear-elastic behavior before total failure occurs by abrupt unstable crack propagation through the sample. Group YT samples on the other hand display stable crack propagation after the point of crack initiation. This leads to a remarkable increase in displacement before the specimen completely fails.

Quantitative assessment of the fracture toughness *J* of all groups is conducted using the large crack extension compensation (XXX). This yields the total fracture toughness *J* until specimen failure occurs. Calculated mean values are 0.99 kJ/m² ± 0.12 kJ/m² for group YT and 0.50 kJ/m² ± 0.03 kJ/m², 0.54 kJ/m² ± 0.03 kJ/m², and 0.49 kJ/m² ± 0.03 kJ/m² for groups XC, XT, and YC, respectively. Means and standard deviations are displayed in Figure 66.**Fehler! Verweisquelle konnte nicht gefunden werden.**

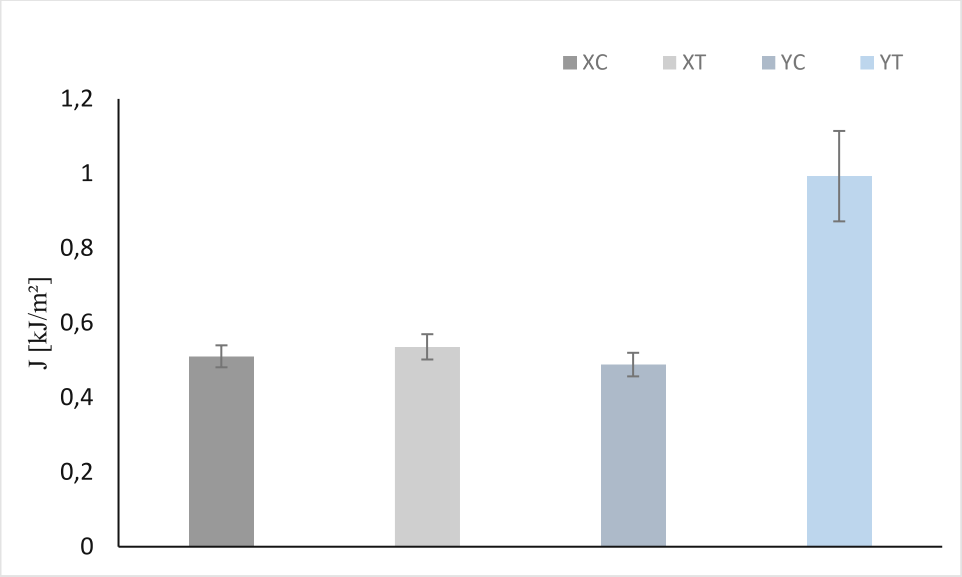

Figure 66. Means and standard deviations of J fracture toughness for all groups.

Thourough analysis of the sample behavior is done by assessing specific mechanical parameters directly obtained from the fracture mechanical tests. These parameters include the maximum force applied to the samples, the elongation at break, the elongation at crack initiation, and the work to crack initiation. Mean values and standard deviations for these factors are summarised in Table 21.

Table 21. Assessed mechanical parameters for all groups.

Parameter	XC	XT	YT	YC
F_{max} [N]	61,7 ± 3,05	60,8 ± 3,49	60,0 ± 3,93	49,3 ± 2,49
Elongation/ break [mm]	0,166 ± 0,016	0,169 ± 0,022	0,167 ± 0,021	0,474 ± 0,042
Elongation/ crack initiation [mm]	0,158 ± 0,0156	0,160 ± 0,0208	0,161 ± 0,0185	0,225 ± 0,0221
Work/ crack initiation [Nmm]	5,3 ± 0,5	6,2 ± 1,0	5,0 ± 0,2	11,5 ± 1,7

The existence of separate material layers in samples of groups XT and YT is verified by means of LSM. The fluorescent ink layers between resin layers are displayed in Figure 67.

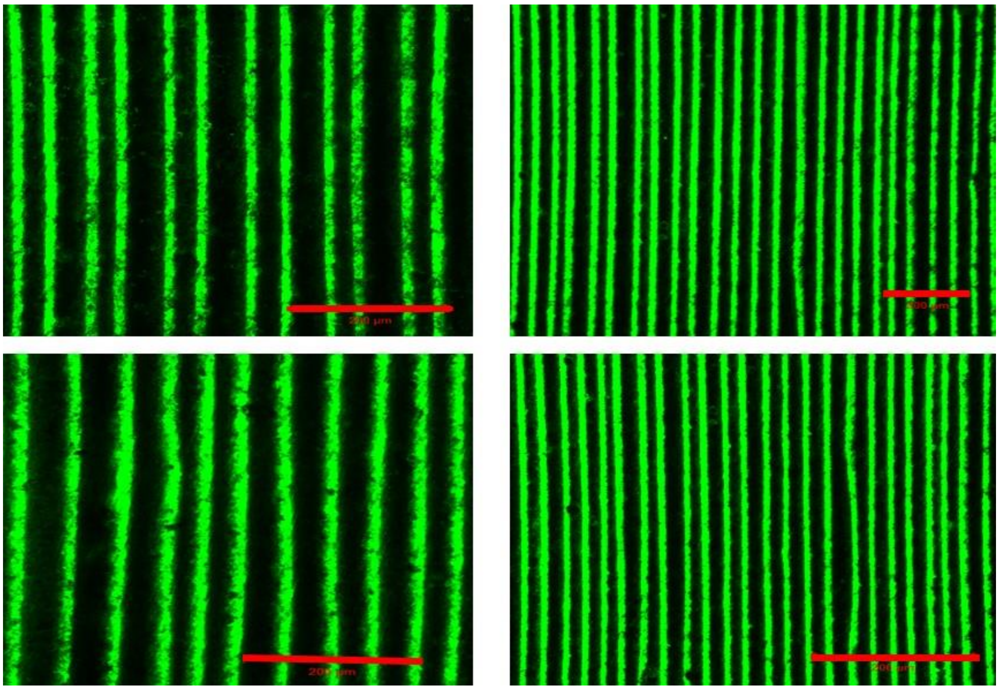

Figure 67. LSM images showing fluorescent ink layers between dark resin layers for group XT (top) and YT (bottom). Scale bar is 200 µm

Further verification of separate ink layers between matrix material layers is done via SEM imaging conducted by Thomas Koch. Figure 68 shows the structure of a YT sample, clearly indicating the periodic alteration of material.

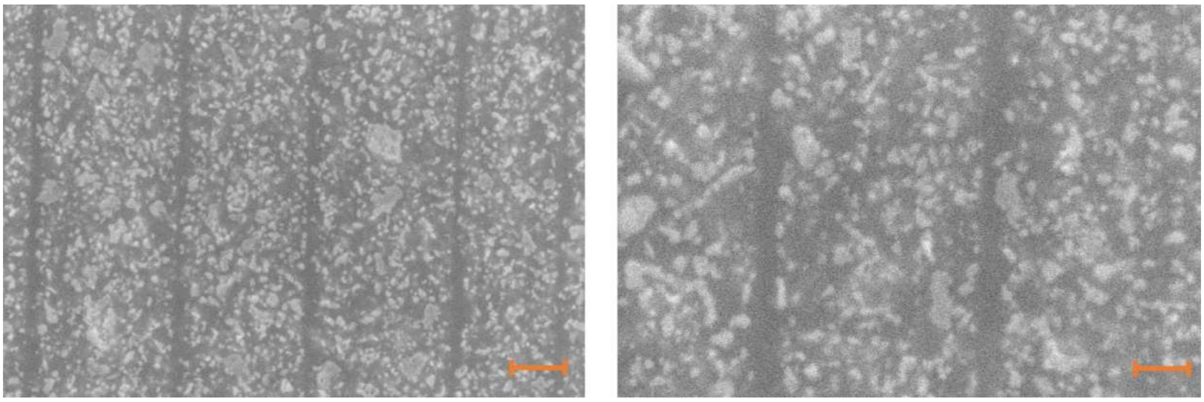

Figure 68. SEM imaging of a YT sample. Ink layers appear as dark vertical lines. Scale bars are 20 µm (left) and 10 µm (right).

SEM imaging of the fracture surface of a YT sample is displayed in Figure 69.

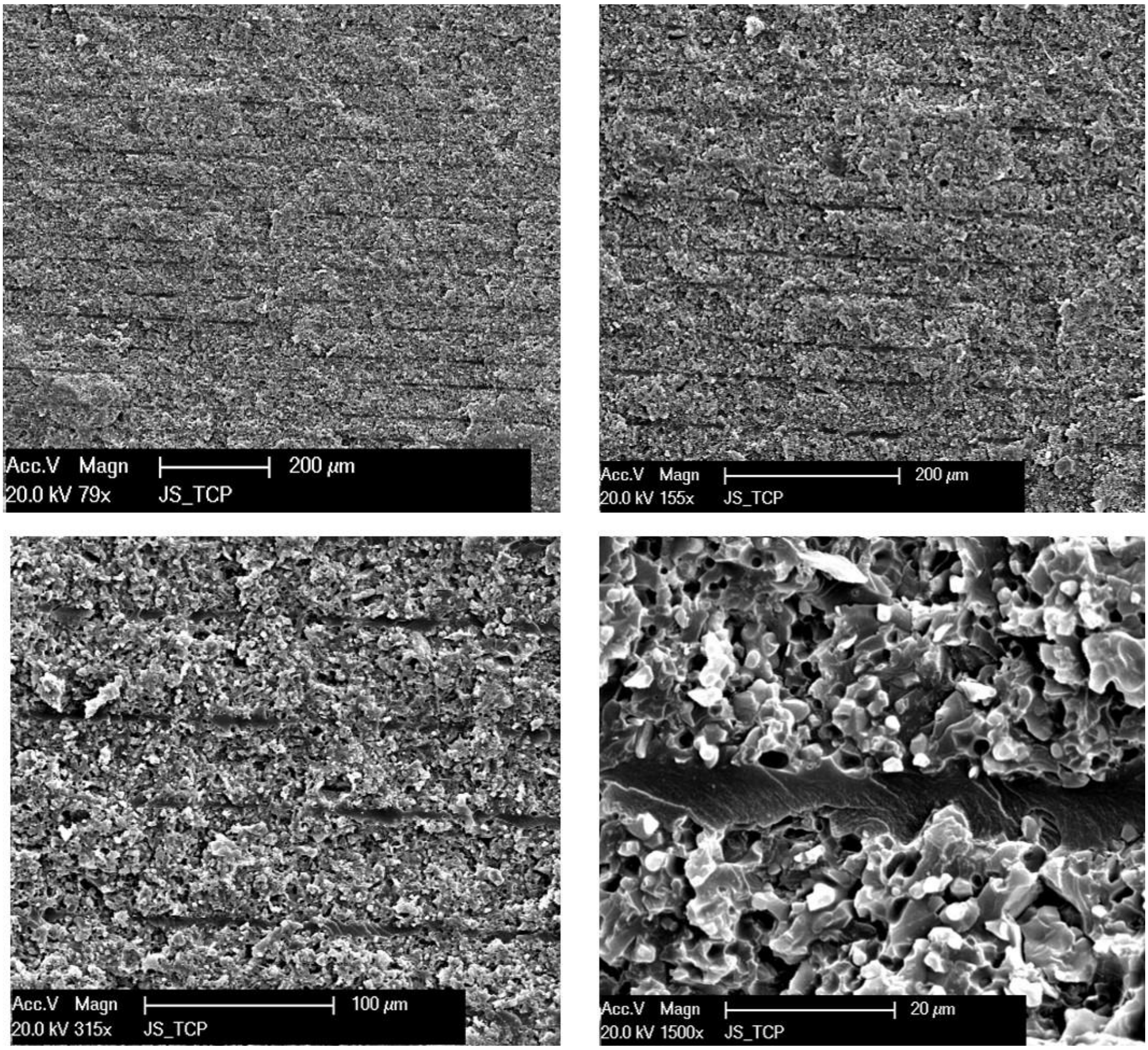

Figure 69. SEM imaging of a YT sample fracture surface in different magnifications. Ink layers appear as dark lines.

Dark ink layers periodically separate the sample surface. The fractured surface appears rugged and irregular but displays no indication of plastic deformation.

Additionally, analysation of the Young's modulus from sample with alternating layers can be done by virtue of nanoindentation performed by Thomas Koch. The variations of Young's modulus in a YT sample are displayed in Figure 70.

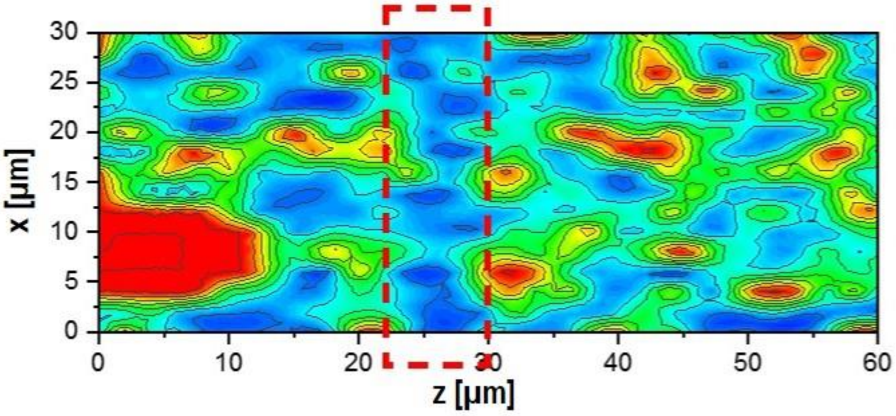

Figure 70. Analysation of the Young's modulus with z being the vertical direction of the sample with respect to printing direction. The marked region of low stiffness represents an ink layer.

Again, the existence of separated ink layers is verified by. The examination displays a defined region featuring low stiffness compared to the surrounding. However, the stiffness in the adjoining regions varies significantly. Small areas of very high stiffness are visible, representing TCP particles of the matrix. These particulate regions are divided by areas of low stiffness representing organic components.

5 Discussion and Outlook

During the course of this thesis, various research questions are answered and new insights are acquired. The hybrid printing system representing a radically novel approach to 3D printing is the focal point. Nevertheless, different scientific issues in closer or wider connection with this 3D printer are solved. These involved manufacturing (e.g., material processability, feasibility of hybrid 3D printing) as well as material topics (e.g., impact of the application, adaptations of mechanical properties). Naturally, the gained knowledge leads to even more challenges and possibilities in the future.

5.1 Resin characterisation and thermo-mechanical performance

In a first step, the analysation of the main component for all manufacturing processes in the present studies (i.e., resin) is paramount. The examination not only involves the measurement of the mechanical properties of the finished parts but also the investigation of the raw material in its liquid state and the processability in the 3D printing unit. Furthermore, the composition is improved to refine the printing process itself and the resulting specimens.

The resin used is inspired by other compositions of composite materials traditionally used in the dental industry. Tooth crowns and implants based on the curing of monomers via UV light are common applications. The composition of the resin is adapted to improve the performance in multiple ways. In the liquid state proper viscosity and the prevention of sedimentation (i.e., sinking of particles in the dispersion due to gravity) are essential to achieve homogeneous results over the course of a printing job. Proper viscosity allows the coating of liquid resin layers with constant height in the vat, necessary for the production of solidified layers with constant height. Sedimentation would lead to a vertical gradient in particle concentration with a maximum at the bottom of the resin container. Consequently, this results in a heterogeneous particle content in the cured layers and the macroscopic specimen. Apart from these factors, the spatial resolution in horizontal directions should be increased as much as possible. This includes the correct amount of photoinitiator and absorber as well as a sufficient curing time. Exaggerated curing time or reactivity of the system might result in over-polymerisation and thus in additional post-processing steps (e.g., extensive sanding). This is time consuming and can potentially alter the macroscopic properties of the sample. On the flip side, insufficient curing results in uncured monomers moving inside the solidified specimen. This molecular movement can corrupt the performance of the printed part and be a health risk if the constituents are toxic.

A material combination is found to ensure a satisfying compromise between all these factors. This composition is used to print testing specimens for the analysation of the thermo-mechanical performance of this resin.

The various thermo-mechanical tests conducted cover a wide range of essential properties for the thermo-mechanical performance of the samples. However, the superordinate goal is to find potential anisotropic behaviour between different printing directions (i.e., orientation of printed layers). For this reason, samples featuring three different orthogonal layer orientations are manufactured and tested. Anisotropy is a crucial phenomenon in 3D printing. Depending on the specific printing technique the produced samples are more or less prone to anisotropic behaviour. Results from other studies draw a diverse picture with regard to anisotropy in SLA 3D printing. Additionally, very limited data addressing SLA printing of composites is available. Hence, examination of potential anisotropic behaviour for the present material is vital for the successive studies with this resin.

The values found in the different tests are in good agreement with results of similar compositions. Bending tests yield values for bending modulus, bending strength and elongation at break in the range of 5000 MPa to 7000 MPa, 50 MPa to 75 MPa, and 1.5 % to 2.5 %, respectively. These numbers are in good agreement with studies examining similar resins [140], [141]. All samples displayed linear elastic fracture behaviour in fracture mechanics tests. Assessed values are in the range of 1.6 MPa*m$^{(1/2)}$ at low speed and between 5 kJ/m² to 8 kJ/m² at impact speed, which are reasonable compared to other studies with comparable resins [142], [143]. All samples tested yield comparable results independently of the printing direction. Moreover, statistical analysis reveals no significant differences ($p=0.05$) between the various printing directions in any assessed parameter. Hence, the assumption of isotropic behaviour of samples printed with this composition and this printing unit is justified.

These findings affect the production capabilities and the printing time. Optimized usage of the limited space available on the building platform through arbitrary positioning of the samples is possible without risking lower performance of certain samples. However, two other implications are even more profound in the framework of this thesis. First, it is not necessary to test samples in various printing directions if not desired by the study design. Results from one printing direction are representative for this material. Second, anisotropy caused by the printing of resin layers can be safely excluded as a reason for potential differences in different printing directions.

5.2 Toughness modification by 3D hybrid printing

The second study involves the first attempts to manufacture samples using the hybrid 3D printing system. The main aim of this research is to prove that the production of testing samples with this machine is possible and beneficial. The underlying idea behind the design is to mimic the structure of composite materials found in marine deep-sea sponge. These composites mostly consist of inorganic glass separated by very thin organic proteins. Although the overall glass content in the skeleton exceeds 99% of mass the mechanical properties of this structure is significantly different compared to common glass. The main difference is the ability to deform and hence the increased fracture toughness compared to SiO_2. The alteration of the typically very brittle behaviour of glass is based on the organic component which separates the glassy regions in the form of thin layers. Nevertheless, the stiffness and strength of the skeleton is comparable to common glass. Thus, the enhancement in toughness is achieved without corrupting the diametrical properties. The underlying material inhomogeneity effect relies on the continuous and abrupt change in mechanical properties (i.e., Young's modulus, yield strength) and allows the slowing or even stopping of a propagating crack.

The hybrid printing system allowing the combined manufacturing with SLA and inkjet printing and the application of two materials featuring completely different mechanical properties is well suited to mimic the structure of the deep-sea sponge. The system allows the solidification of a particle filled resin, resembling the stiff and strong matrix as well as thin layers of soft ink similar to the protein layers. These components feature a Young's modulus ratio of 1:25, clearly exceeding the minimum ratio 1:5 for the material inhomogeneity effect to work. The ultimate goal is to produce parts featuring stiffness and strength similar to pure matrix material samples while simultaneously increasing the toughness. The toughening effect heavily relies on distinct layers resulting in an abrupt change in stiffness. Each transitional area from soft to brittle material reduces the crack driving force. Hence, crack propagation gets hindered or even stopped every time the crack tip reaches the boundary between soft and brittle material. Thus, samples featuring continuous alteration of resin and ink layers are produced and compared to pure resin parts as well as samples produced of a premixed blend of resin and ink.

The first result is the verification of the proper functionality of the hybrid printing system. The system semi-automatically produces samples of the desired structure. Layer heights of resin and ink are adjustable to a certain degree. The height of resin layers can be set very precisely in the range of singular µm via the distance between the building platform and the liquid resin in the vat and is only limited by the size of the filling particles. Ink layer height, on the other hand,can only be adjusted by manipulating the jetting pattern (i.e., location of drop placement and quantity of droplets per unit area.). However, the resolution of the inkjet print head is limited to 360 dpi and the drop size is only indirectly adjustable through the liquid ink properties (e.g., surface tension, viscosity) as well as print head parameters (e.g., driving voltage). The focus in this study is to ensure a continuous and homogeneous soft interlayer to verify the applicability of the selected toughening approach. Consequently, relatively thick ink layers in the range of 5-7 µm are accepted to guarantee separation between matrix material layers. This comes at the cost of reduced stiffness and strength compared to homogeneous matrix material. Young's Modulus and yield strength are reduced by 50 % and 12 %, respectively.

The toughening effect of the soft interlayers is confirmed with Dynstat impact strength tests. Hybrid material samples displayed an increase of 70 % in impact strength compared to pure resin specimens. Correspondingly, elongation at break is increased by 22 % in bending tests for hybrid material parts.

Another noteworthy finding is that there is no statistical relevant difference between pure resin samples and blended ones. This clearly shows that the toughening effect arises from the the distinct structure of the samples featuring separate material layers. Thus, adding the low functional monomers of the ink to the resin has no impact on the toughness or other mechanical properties of the final part.

At last, microscopic imaging reveals some form of diffusion between the layers resulting in the colouring of large areas of the specimens. The non-reactive diluent present in the resin as well as unreacted monomers in both materials could cause this effect. This undesired interaction between initially separated material layers leads to a levelling effect between the different mechanical properties. Consequently, the transitional area between the layers is enlarged and the difference in Young's modulus is somewhat equalised. Hence, the reduction of crack driving force occurring at the sharp transition from soft to stiff material is diminished and the toughening effect reduced.

With the selected materials and printing strategy, there is still a remarkable increase in fracture toughness, albeit the diffusional process due to the relatively thick interlayers. However, these result in a significant reduction in strength and stiffness. Clearly, adaptations to the raw materials and the printing patterns are necessary to suppress the diffusion process and conserve the initial mechanical parameters. Considering all results, the first manufacturing attempts with this new machine show promising results in terms of an innovative toughening mechanism in polymer 3D printing.

5.3 Application of the material inhomogeneity effect

In the last step, the proven concept of the material inhomogeneity effect via the hybrid printing system is analysed in more detail. The overarching objective is to solve the problems found in the first study with this machine. Additionally, a more precise analysation of the fracturing process and a more accurate way to quantify the toughening effect are performed.

First, the raw materials are adapted to tackle the main drawback of the former composition, namely the diffusion process. The non-reactive diluent is completely omitted and replaced by a reactive component. Thus, all organic substances are part of the polymerisation process reducing the amount of potentially remaining unreacted liquid phases in the solidified specimen. Additionally, a product featuring lower stiffness replaces the original ink component. The ratio of Young's Modulus and elongation at break between resin and ink is $66 * 10^3$ and $14 * 10^{-3}$. Hence, the difference in Young's Modulus required for the toughening effect is remarkably larger than in the previous study. This further strengthens the shielding effect of the transitional area between two material layers and consequently increases the macroscopic fracture toughness.

SENB specimens are printed for the examination of fracture toughness at quasi-static conditions in two different orthogonal directions. Samples consisting of alternating layers of resin and ink as well as pure resin parts are produced in both printing directions. A three-point bending test set-up is selected. This set-up allows closer analysation of the loading process due to its slow deformation rate compared to impact strength tests. To gain deeper insight into the propagation of the crack, all samples are recorded using a camera attached to a microscope. This allows continuous measurement of the crack tip position as well as qualitative analysis of its behaviour.

Samples with alternating material layers in a direction perpendicular to the crack propagation show a significantly different behavior in bending tests than the other three groups. These other three groups display an almost ideal linear elastic material behavior before total failure occurs, albeit one of those groups featuring separate material layers. The first group, with the correct layer direction for effective crack deflection displays a larger deformation and some form of non-linear elastic behaviour before fracturing.

Different mechanical parameters are assessed to quantify differences between the groups. The mean maximum force reached in the tests is similar for groups XC,XT, and YC and 17 % lower for group YT. On the other hand, mean elongation at break is increased by 35 % in group YT samples compared to the other three groups. Mean elongation at crack initiation is 29 % higher and the mean work to crack initiation is doubled for YT samples compared to the other three groups.

Fracture toughness is assessed by means of J-Integral. This parameter is suited for the quantification of non-linear elastic fracture behavior. J-values for hybrid material specimens featuring the correct layer orientation display J fracture toughness of about 1 kJ/m² practically doubling assessed values from the other three groups (values between 0.49 kJ/m² and 0.53 kJ/m²). This represents an increase of 100 % in fracture toughness.

LSM imaging proves the existence of separate ink layers via a fluorescent colouring agent incorporated in the ink. Ink layers appear relatively stable in direction and height showing no indication of a diffusion process. SEM imaging and nanoindentation measurements further verify the existence of periodic material alteration. Still, ink layers appear remarkably thicker (15-17 µm) in LSM compared to the other methods (6-8 µm). This difference indicates that the colouring agent diffuses from originally colour ink layers to the adjoining matrix layers. Again, this diffusion includes not only the colouring of larger areas in the sample but also the harmonisation of material properties. Hence, the interfacial zone between separate layers, which should be as thin as possible resulting in an abrupt change in mechanical properties, is enlarged.

Analysis of the stiffness of the separate regions shows that the mechanical properties vary remarkably within the matrix layers. Although TCP particles are confined to distinct areas and not present in ink layers, which are confirmed by SEM imaging, matrix layers appear rugged to some extent. Thus, the difference in mechanical properties at the interface between separate material layers is not constant. Consequently, the full potential of the material inhomogeneity effect (i.e., crack stopping) is not unlocked in the present material. Sample behaviour is changed from nearly ideal linear elastic to non-linear elastic along with an increase in displacement before fracture occurs. However, mechanical tests show no indication of plastic deformation in any of the groups. This result is supported by SEM analysis of the fracture surfaces. Fracture faces display no evidence of plastic deformation (e.g. crazes).

This study represents an advancement to the first hybrid printing system study. The results clearly show the effectiveness of the material inhomogeneity effect and its dependency not only on separated material layers but also on their orientation. The increase in fracture toughness is noticeable while the reduction of maximum force reached, as an indicator for stiffness and strength is contained compared to the former study. The ultimate goal of increased toughness and full conservation of the other parameters is still not reached but the adapted materials show the potential for further improvement in the future.

5.4. Outlook

The combination of two separate additive manufacturing processes offers a wide range of possibilities for the production of samples. One of the greatest advantages of 3D printing is the fact that final material properties are determined during the production process. Hence, the application of the hybrid printing system allows the selective adaptation of macroscopic properties in the course of the manufacturing process. In the present studies, modification of mechanical properties particularly fracture toughness is paramount. This task is fulfilled with remarkable success. These modifications most often involve the entire structure of the printed specimens. However, partial alteration of samples produced with this technique is just as feasible. Even greater potential arises from the fact that other properties beside mechanical parameters can be manipulated assuming suited raw materials. Some examples for application areas of the hybrid printing technology are described in the following.

One of the most obvious applications which is conducted even in the present studies as a side effect is the intended colouring of printed parts. This could be done for aesthetic or optical purposes, allowing a better reproduction of original parts. Additionally, personal decorations and embellishments are possible. Aside from these artful purposes functional colouring indicating wear or abrasion as well as barcodes are conceivable.

Another application is the connection of resins with conductive inks. Inks containing particles allowing electrical conductivity are already available for industrial applications. The application of such an ink in the hybrid printing process would enable the production of conductor tracks within complex geometries without the requirement to implement them after the initial building process.

A third possible field of application is specifically designated to lithography based 3D printing methods. Depending on the geometry, these techniques often require support structures to stabilise overhanging areas within the printed part. Although the material requirement for the production of these support structures is typically small compared to the actual part, the post-processing steps become significantly laborious. The detachment of these structures is time-consuming and involves the risk of damaging the actual part. Furthermore, the attachment spot on the surface of the sample might suffer from the dismantling process. With the aid of the hybrid printing system, entire support structures or solely the conjunction areas between support and manufactured part could be produced from a different material with desired properties (e.g., low melting point). This would simplify the post-processing step and eventually might even allow the automation of the whole process.

The practicability of the hybrid printing system is verified in the studies present. Although the focus lays on the improvement of the mechanical properties, other applications are possible. The combination of different materials in conjunction with almost arbitrary geometries feasible with SLA offer a wide range of potential application fields.

References

[1] Anonymous, „Airbus standardizes stratasys 3D printing material for use in making airplane parts.“, *Mod. Mach. Shop*, Bd. 89, Nr. 7, S. 52, Dez. 2016.

[2] M. R. Nichols, „How does the automotive industry benefit from 3D metal printing?“, *Met. Powder Rep.*, Bd. 74, Nr. 5, S. 257–258, 2019, doi: https://doi.org/10.1016/j.mprp.2019.07.002.

[3] X. Zhu, H. Li, L. Huang, M. Zhang, W. Fan, und L. Cui, „3D printing promotes the development of drugs“, *Biomed. Pharmacother.*, Bd. 131, S. 110644, 2020, doi: https://doi.org/10.1016/j.biopha.2020.110644.

[4] C. Gosselin, R. Duballet, P. Roux, N. Gaudillière, J. Dirrenberger, und P. Morel, „Large-scale 3D printing of ultra-high performance concrete – a new processing route for architects and builders“, *Mater. Des.*, Bd. 100, S. 102–109, 2016, doi: https://doi.org/10.1016/j.matdes.2016.03.097.

[5] X. Zhang *u. a.*, „Large-scale 3D printing by a team of mobile robots“, *Autom. Constr.*, Bd. 95, S. 98–106, 2018, doi: https://doi.org/10.1016/j.autcon.2018.08.004.

[6] F. Melchels, J. Feijen, und D. Grijpma, „A review on stereolithography and its applications in biomedical engineering“, *Biomaterials*, Bd. 31, S. 6121–6130, 2010.

[7] J. W. Halloran, „Ceramic Stereolithography: Additive Manufacturing for Ceramics by Photopolymerization“, *Annu. Rev. Mater. Res.*, Bd. 46, Nr. 1, S. 19–40, 2016.

[8] S. Zakeri, M. Vippola, und E. Levänen, „A comprehensive review of the photopolymerization of ceramic resins used in stereolithography“, *Addit. Manuf.*, Bd. 35, S. 101177, 2020, doi: https://doi.org/10.1016/j.addma.2020.101177.

[9] W. Wang und J. Sun, „Dimensional accuracy and clinical adaptation of ceramic crowns fabricated with the stereolithography technique“, *J. Prosthet. Dent.*, Bd. 125, Nr. 4, S. 657–663, 2021.

[10] L. M. Kalossaka, A. A. Mohammed, G. Sena, L. Barter, und C. Myant, „3D printing nanocomposite hydrogels with lattice vascular networks using stereolithography“, *J. Mater. Res.*, Bd. 36, Nr. 21, S. 4249–4261, 2021.

[11] H.-W. Kang, I. H. Lee, und D.-W. Cho, „Development of a micro-bellows actuator using micro-stereolithography technology“, *Microelectron. Eng.*, Bd. 83, Nr. 4, S. 1201–1204, 2006.

[12] C. Gorsche *u. a.*, „Rapid formation of regulated methacrylate networks yielding tough materials for lithographybased 3D printing“, *Polym. Chem.*, Bd. 7, 2016, doi: 10.1039/c5py02009c.

[13] S. C. Ligon-Auer, M. Schwentenwein, C. Gorsche, J. Stampfl, und R. Liska, „Toughening of photo-curable polymer networks: a review“, 2015.

[14] Gibson, Ian, D. Rosen, B. Stucker, und M. Khorasani, *Additive Manufacturing Technologies*, 3. Aufl. Cham: Springer, 2021.

[15] J. Butt und H. Shirvani, „Additive, Subtractive, and Hybrid Manufacturing Processes“, in *Advances in Manufacturing and Processing of Materials and Structures*, 1. Aufl., Boca Raton: Taylor & Francis Group, 2019.

[16] A. Gebhardt und J.-S. Hötter, *Additive Manufacturing 3D Printing for Prototyping and Manufacturing*, 1. Aufl. München: Carl Hanser, 2016.

[17] A. Gebhardt, *Generative Fertigungsverfahren*, 4. Aufl. München: Carl Hanser, 2013.

[18] A. Gebhardt, J. Kessler, und L. Thurn, *3D Printing. Understanding Additive Manufacturing*, 2. Aufl. München: Carl Hanser, 2019.

[19] „Additive manufacturing (Amsterdam) Additive manufacturing.“, *Additive manufacturing.* Elsevier B.V., Amsterdam, 2014.

[20] J. Z. Manapat, Q. Chen, P. Ye, und R. C. Advincula, „3D Printing of Polymer Nanocomposites via Stereolithography“, *Macromol. Mater. Eng.*, Bd. 302, Nr. 9, S. 1600553, 2017, doi: https://doi.org/10.1002/mame.201600553.

[21] H. Kadry, S. Wadnap, C. Xu, und F. Ahsan, „Digital light processing (DLP) 3D-printing technology and photoreactive polymers in fabrication of modified-release tablets“, *Eur. J. Pharm. Sci.*, Bd. 135, S. 60–67, 2019, doi: https://doi.org/10.1016/j.ejps.2019.05.008.

[22] Y. Lu, G. Mapili, G. Suhali, S. Chen, und K. Roy, „A digital micro-mirror device-based system for the microfabrication of complex, spatially patterned tissue engineering scaffolds“, *J. Biomed. Mater. Res.*, Bd. 77, Nr. 2, S. 396–405, 2006.

[23] „Digital Light Processing“, *3DPrinting.Lighting*. https://www.3dprinting.lighting/3d-printing-technologies/digital-light-processing/ (zugegriffen 8. Oktober 2021).

[24] „Технология DLP“. https://www.ixbt.com/digimage/dlp.html (zugegriffen 11. Oktober 2021).

[25] I. Hutchings, G. Martin, und S. Hoath, „Introductory Remarks“, in *Fundamentals of Inkjet Printing. The Science of Inkjet and Droplets*, 1. Aufl., Weinheim: Wiley, 2016.

[26] S. Barui, „3D inkjet printing of biomaterials: Principles and applications“, *Med. DEVICES Sens.*, Bd. 4, Nr. 1, S. e10143, Feb. 2021, doi: 10.1002/mds3.10143.

[27] M. Singh, H. M. Haverinen, P. Dhagat, und G. E. Jabbour, „Inkjet Printing—Process and Its Applications“, *Adv. Mater.*, Bd. 22, Nr. 6, S. 673–685, 2010, doi: https://doi.org/10.1002/adma.200901141.

[28] Y. Guo, H. S. Patanwala, B. Bognet, und A. W. Ma, „Inkjet and inkjet-based 3D printing: connecting fluid properties and printing performance“, *Rapid Prototyp. J.*, Bd. 23, Nr. 3, S. 562–576, 2017, doi: 10.1108/RPJ-05-2016-0076.

[29] B.-J. de Gans, P. C. Duineveld, und U. S. Schubert, „Inkjet Printing of Polymers: State of the Art and Future Developments“, *Adv. Mater.*, Bd. 16, Nr. 3, S. 203–213, 2004, doi: https://doi.org/10.1002/adma.200300385.

[30] P. Wang, J. Zhou, B. Xu, C. Lu, Q. Meng, und H. Liu, „Bioinspired Anti-Plateau–Rayleigh-Instability on Dual Parallel Fibers“, *Adv. Mater.*, Bd. 32, Nr. 45, S. 2003453, 2020, doi: https://doi.org/10.1002/adma.202003453.

[31] Lord Rayleigh, „On The Instability Of Jets“, *Proc. Lond. Math. Soc.*, Bd. s1-10, Nr. 1, S. 4–13, 1878, doi: https://doi.org/10.1112/plms/s1-10.1.4.

[32] M. Ikegawa, E. Ishii, N. Harada, und T. Takagishi, „Development of Ink-Particle Flight Simulation for Continuous Inkjet Printers“, *J. Manuf. Sci. Eng.*, Bd. 136, Nr. 5, Aug. 2014, doi: 10.1115/1.4027943.

[33] R. Daly, T. S. Harrington, G. D. Martin, und I. M. Hutchings, „Inkjet printing for pharmaceutics – A review of research and manufacturing“, *Int. J. Pharm.*, Bd. 494, Nr. 2, S. 554–567, 2015, doi: https://doi.org/10.1016/j.ijpharm.2015.03.017.

[34] D. Wallace, „Overview of Inkjet-Based Micromanufacturing“, in *Inkjet-based Micromanufacturing*, 1. Aufl., Weinheim: Wiley, 2012.

[35] H. Wijshoff, „The dynamics of the piezo inkjet printhead operation“, *Phys. Rep.*, Bd. 491, Nr. 4, S. 77–177, 2010, doi: https://doi.org/10.1016/j.physrep.2010.03.003.

[36] N. Morita, „Thermal Inkjet“, in *Inkjet-based Micromanufacturing*, 1. Aufl., Weinheim: Wiley, 2012.

[37] E. Parry, S. Bolis, S. J. Elston, A. A. Castrejón-Pita, und S. M. Morris, „Drop-on-Demand Inkjet Printing of Thermally Tunable Liquid Crystal Microlenses“, *Adv. Eng. Mater.*, Bd. 20, Nr. 3, S. 1700774, 2018, doi: https://doi.org/10.1002/adem.201700774.

[38] H. Dong, W. W. Carr, und J. F. Morris, „Visualization of drop-on-demand inkjet: Drop formation and deposition“, *Rev. Sci. Instrum.*, Bd. 77, Nr. 8, S. 085101, 2006, doi: 10.1063/1.2234853.

[39] O. A. Basaran, „Small-scale free surface flows with breakup: Drop formation and emerging applications“, *AIChE J.*, Bd. 48, Nr. 9, S. 1842–1848, 2002, doi: https://doi.org/10.1002/aic.690480902.

[40] D. Jang, D. Kim, und J. Moon, „Influence of Fluid Physical Properties on Ink-Jet Printability“, *Langmuir*, Bd. 25, Nr. 5, S. 2629–2635, März 2009, doi: 10.1021/la900059m.

[41] Z. Tang, K. Fang, M. N. Bukhari, Y. Song, und K. Zhang, „Effects of Viscosity and Surface Tension of a Reactive Dye Ink on Droplet Formation“, *Langmuir*, Bd. 36, Nr. 32, S. 9481–9488, Aug. 2020, doi: 10.1021/acs.langmuir.0c01392.

[42] G. H. McKinley und M. Renardy, „Wolfgang von Ohnesorge“, *Phys. Fluids*, Bd. 23, Nr. 12, S. 127101, 2011, doi: 10.1063/1.3663616.

[43] A. Lee, K. Sudau, K. H. Ahn, S. J. Lee, und N. Willenbacher, „Optimization of Experimental Parameters to Suppress Nozzle Clogging in Inkjet Printing“, *Ind. Eng. Chem. Res.*, Bd. 51, Nr. 40, S. 13195–13204, Okt. 2012, doi: 10.1021/ie301403g.

[44] J. V. Crivello und E. Reichmanis, „Photopolymer Materials and Processes for Advanced Technologies“, *Chem. Mater.*, Bd. 26, Nr. 1, S. 533–548, Jan. 2014, doi: 10.1021/cm402262g.

[45] J. Zhang und P. Xiao, „3D printing of photopolymers“, *Polym Chem*, Bd. 9, Nr. 13, S. 1530–1540, 2018, doi: 10.1039/C8PY00157J.

[46] R. Young und P. Lovell, *Introduction to Polymers*, 3. Aufl. Boca Raton: Taylor & Francis Group.

[47] A. Peacock und A. Calhoun, *Polymer Chemistry*, 1. Aufl. München: Hanser, 2006.

[48] H. Domininghaus, P. Elsner, P. Eyerer, und T. Hirth, *Kunststoffe*, 8. Aufl. Heidlberg: Springer, 2004.

[49] P. Eyerer und H. Schüle, *Polymer Engineering*, 2. Aufl. Heidlberg: Springer, 2020.

[50] J. Stampfl und O. Guillaume, „Biocompatible Materials - Course handout“. 2021.

[51] H. B. Song, A. Baranek, B. T. Worrell, W. D. Cook, und C. N. Bowman, „Photopolymerized Triazole-Based Glassy Polymer Networks with Superior Tensile Toughness“, *Adv. Funct. Mater.*, Bd. 28, Nr. 22, S. 1801095, Mai 2018, doi: 10.1002/adfm.201801095.

[52] S. Ligon, R. Liska, J. Stampfl, M. Gurr, und R. Mülhaupt, „Polymers for 3D Printing and Customized Additive Manufacturing“, *Chem. Rev.*, Bd. 117, S. 10212–10290, 2017, doi: 10.1021/acs.chemrev.7b00074.

[53] S. Orman, C. Hofstetter, A. Aksu, F. Reinauer, R. Liska, und S. Baudis, „Toughness enhancers for bone scaffold materials based on biocompatible photopolymers“, *J. Polym. Sci. Part Polym. Chem.*, Bd. 57, Nr. 2, S. 110–119, Jan. 2019, doi: 10.1002/pola.29273.

[54] J. C. J. Bart, *Additives in Polymers: Industrial Analysis and Applications*, 1. Aufl., Nr. ISBN: 9780470850626. Hoboken: Hoboken: Wiley, 2005. doi: 10.1002/0470012064.

[55] Bolgar Michael, Hubball Jack, Groeger Joseph, und Meronek Susan, Hrsg., *Handbook for the Chemical Analysis of Plastic and Polymer Additives*. CRC Press, 2015. doi: 10.1201/b19124.

[56] T. F. Tadros, *Dispersion of Powders: In Liquids and Stabilization of Suspensions*. Weinheim: John Wiley & Sons, Incorporated, 2012.

[57] T. Tadros, *Encyclopedia of Colloid and Interface Science*, Nr. ISBN: 3642206646. Berlin, Heidelberg: Berlin, Heidelberg: Springer Berlin / Heidelberg, 2013.

[58] „Performance Coating Dispersants“. http://explore.lubrizol.com/performance-coating-dispersants (zugegriffen 16. November 2021).

[59] „Steric stabilization“. https://ebooks.byk.com/en/wetting-and-dispersing/steric-stabilization/ (zugegriffen 16. November 2021).

[60] M. Kontopoulou und M. Kontopoulou, *Applied polymer rheology: polymeric fluids with industrial applications.*, Nr. ISBN: 9780470416709. WILEY, 2011. doi: 10.1002/9781118140611.

[61] B. Janet, „The History of Dyes and Pigments: From Natural Dyes to High Performance Pigments“, in *Colour Design - Theories and Applications*, 2nd Edition., Elsevier, 2017, S. 1–1.

[62] I. S. Ahmed, S. A. Shama, M. M. Moustafa, H. A. Dessouki, und A. A. Ali, „Synthesis and spectral characterization of CoxMg1−xAl2O4 as new nano-coloring agent of ceramic pigment“, *Spectrochim. Acta. A. Mol. Biomol. Spectrosc.*, Bd. 74, Nr. 3, S. 665–672, Okt. 2009, doi: 10.1016/j.saa.2009.07.024.

[63] A. M. Gueli, G. Bonfiglio, S. Pasquale, und S. O. Troja, „Effect of particle size on pigments colour“, *Color Res. Appl.*, Bd. 42, Nr. 2, S. 236–243, Apr. 2017, doi: 10.1002/col.22062.

[64] J. P. Fouassier und J. Laleveacute;e, *Photoinitiators for Polymer Synthesis: Scope, Reactivity, and Efficiency*, 1. Aufl. Weinheim: Wiley-VCH, 2012.

[65] F. M. Alejandro *u. a.*, *3D Printing with Light*. Berlin Boston: De Gruyter, 2021. [Online]. Verfügbar unter: 10.1515/9783110570588

[66] H. S. Wang, J. Cho, D. S. Song, J. H. Jang, J. Y. Jho, und J. H. Park, „High-Performance Electroactive Polymer Actuators Based on Ultrathick Ionic Polymer–Metal Composites with Nanodispersed Metal Electrodes“, *ACS Appl. Mater. Interfaces*, Bd. 9, Nr. 26, S. 21998–22005, Juli 2017, doi: 10.1021/acsami.7b04779.

[67] S. Myllymäki, M. Teirikangas, und M. Kokkonen, „BaSrTiO3 ceramic-polymer composite material lens antennas at 220–330 GHz telecommunication applications“, *Electron. Lett.*, Bd. 56, Nr. 22, S. 1165–1167, Okt. 2020, doi: 10.1049/el.2020.1875.

[68] J. Guo *u. a.*, „Recent Progress in Applications of the Cold Sintering Process for Ceramic–Polymer Composites“, *Adv. Funct. Mater.*, Bd. 28, Nr. 39, S. 1801724, Sep. 2018, doi: 10.1002/adfm.201801724.

[69] N. Grossiord *u. a.*, „High-Conductivity Polymer Nanocomposites Obtained by Tailoring the Characteristics of Carbon Nanotube Fillers“, *Adv Funct Mater*, Bd. 18, Nr. ISSN: 1057-9257, S. 3234, 2008, doi: 10.1002/adfm.200800528.

[70] H. Shin, S. Yang, J. Choi, S. Chang, und M. Cho, „Effect of interphase percolation on mechanical behavior of nanoparticle-reinforced polymer nanocomposite with filler agglomeration: A multiscale approach“, *Chem. Phys. Lett.*, Bd. 635, S. 80–85, Aug. 2015, doi: 10.1016/j.cplett.2015.06.054.

[71] „Mechanical Testing“, in *Practical Testing and Evaluation of Plastics*, John Wiley & Sons, Ltd, 2019, S. 87–131. doi: https://doi.org/10.1002/9783527667314.ch5.

[72] W. Grellmann und S. Seidler, *Kunststoffprüfung*, 3. Aufl. München: Hanser, 2015.

[73] J. Bergström, „2 - Experimental Characterization Techniques“, in *Mechanics of Solid Polymers*, J. Bergström, Hrsg. William Andrew Publishing, 2015, S. 19–114. doi: https://doi.org/10.1016/B978-0-323-31150-2.00002-9.

[74] „Mechanical Properties“, in *Handbook of Plastics Testing and Failure Analysis*, John Wiley & Sons, Ltd, 2007, S. 17–93. doi: https://doi.org/10.1002/9780470100424.ch2.

[75] M. F. H. Wolff, V. Salikov, S. Antonyuk, S. Heinrich, und G. A. Schneider, „Three-dimensional discrete element modeling of micromechanical bending tests of ceramic–polymer composite materials“, *Powder Technol.*, Bd. 248, S. 77–83, 2013, doi: https://doi.org/10.1016/j.powtec.2013.07.009.

[76] F. Mujika, „On the difference between flexural moduli obtained by three-point and four-point bending tests“, *Polym. Test.*, Bd. 25, Nr. 2, S. 214–220, 2006, doi: https://doi.org/10.1016/j.polymertesting.2005.10.006.

[77] S. S. Chauhan, B. P. Singh, R. S. Malik, P. Verma, und V. Choudhary, „Detailed dynamic mechanical analysis of thermomechanically stable melt-processed PEK–MWCNT nanocomposites“, *Polym. Compos.*, Bd. 39, Nr. 7, S. 2587–2596, 2018, doi: https://doi.org/10.1002/pc.24247.

[78] A. Etaati, S. Pather, Z. Fang, und H. Wang, „The study of fibre/matrix bond strength in short hemp polypropylene composites from dynamic mechanical analysis“, *Compos. Part B Eng.*, Bd. 62, S. 19–28, 2014, doi: https://doi.org/10.1016/j.compositesb.2014.02.011.

[79] „Indentation“, in *Chemistry and Physics of Mechanical Hardness*, John Wiley & Sons, Ltd, 2009, S. 11–26. doi: https://doi.org/10.1002/9780470446836.ch2.

[80] F. Alisafaei, C.-S. Han, und S. H. R. Sanei, „On the time and indentation depth dependence of hardness, dissipation and stiffness in polydimethylsiloxane“, *Polym. Test.*, Bd. 32, Nr. 7, S. 1220–1228, 2013, doi: https://doi.org/10.1016/j.polymertesting.2013.07.013.

[81] J. Menčík, L. H. He, und J. Němeček, „Characterization of viscoelastic-plastic properties of solid polymers by instrumented indentation“, *Polym. Test.*, Bd. 30, Nr. 1, S. 101–109, 2011, doi: https://doi.org/10.1016/j.polymertesting.2010.11.006.

[82] G. K. Banini *u. a.*, „Nanoindentation around Vickers microindentation in MgO (100) crystal“, *Int. J. Mater. Res.*, Bd. 93, Nr. 9, S. 875–878, 2002, doi: doi:10.3139/ijmr-2002-0150.

[83] R. Buchs, S. Basu, O. A. Elshrief, R. Coward, und M. W. Barsoum, „Spherical nanoindentation and Vickers microhardness study of the deformation of poled BaTiO3 single crystals“, *J. Appl. Phys.*, Bd. 105, Nr. 9, S. 093540, 2009, doi: 10.1063/1.3117496.

[84] K. Kasraee, M. Yousefpour, und S. A. Tayebifard, „Microstructure and mechanical properties of Ti5Si3 fabricated by spark plasma sintering“, *J. Alloys Compd.*, Bd. 779, S. 942–949, 2019, doi: https://doi.org/10.1016/j.jallcom.2018.11.319.

[85] N. Domun, H. Hadavinia, T. Zhang, T. Sainsbury, G. H. Liaghat, und S. Vahid, „Improving the fracture toughness and the strength of epoxy using nanomaterials – a review of the current status“, *Nanoscale*, Bd. 7, Nr. 23, S. 10294–10329, 2015, doi: 10.1039/C5NR01354B.

[86] „Polymer Service Merseburg“. https://wiki.polymerservice-merseburg.de/index.php/Schlagbiegeversuch (zugegriffen 4. Juni 2020).

[87] K. S. Anderson, K. M. Schreck, und M. A. Hillmyer, „Toughening Polylactide“, *Polym. Rev.*, Bd. 48, Nr. 1, S. 85–108, 2008, doi: 10.1080/15583720701834216.

[88] E. E. Gdoutos, „Linear Elastic Stress Field in Cracked Bodies“, in *Fracture Mechanics: An Introduction*, Cham: Springer International Publishing, 2020, S. 15–63. doi: 10.1007/978-3-030-35098-7_2.

[89] C. T. Sun und Z.-H. Jin, „Chapter 1 - Introduction“, in *Fracture Mechanics*, C. T. Sun und Z.-H. Jin, Hrsg. Boston: Academic Press, 2012, S. 1–10. doi: https://doi.org/10.1016/B978-0-12-385001-0.00001-8.

[90] M. Berer und G. Pinter, „Determination of crack growth kinetics in non-reinforced semi-crystalline thermoplastics using the linear elastic fracture mechanics (LEFM) approach“, *Polym. Test.*, Bd. 32, Nr. 5, S. 870–879, 2013, doi: https://doi.org/10.1016/j.polymertesting.2013.03.022.

[91] J. J. Hoyos, M. Masoumi, V. F. Pereira, A. P. Tschiptschin, M. T. P. Paes, und J. A. Avila, „Influence of hydrogen on the microstructure and fracture toughness of friction stir welded plates of API 5L X80 pipeline steel“, *Int. J. Hydrog. Energy*, Bd. 44, Nr. 41, S. 23458–23471, 2019, doi: https://doi.org/10.1016/j.ijhydene.2019.06.210.

[92] S. Pillot und P. Pacqueau, „An attempt to define a Charpy V-notched mastercurve to fit transition of ferritic steels“, *Eng. Fract. Mech.*, Bd. 135, S. 259–273, 2015, doi: https://doi.org/10.1016/j.engfracmech.2015.01.012.

[93] V. Rizov, „Mixed-mode I/II fracture study of polymer composites using Single Edge Notched Bend specimens“, *Comput. Mater. Sci.*, Bd. 77, S. 1–6, 2013, doi: https://doi.org/10.1016/j.commatsci.2013.04.021.

[94] M. R. Mehraban, M. R. Ayatollahi, B. Bahrami, und F. Berto, „Higher order stress terms in sharp notch problems under pure-out-of-plane loading“, *Fatigue Fract. Eng. Mater. Struct.*, Bd. 45, Nr. 2, S. 500–513, 2022, doi: https://doi.org/10.1111/ffe.13613.

[95] L. P. Pook, „A 50-year retrospective review of three-dimensional effects at cracks and sharp notches“, *Fatigue Fract. Eng. Mater. Struct.*, Bd. 36, Nr. 8, S. 699–723, 2013, doi: https://doi.org/10.1111/ffe.12074.

[96] D. A. Lados und D. Apelian, „Limitations of elastic definitions in Al–Si–Mg cast alloys with enhanced plasticity: linear elastic fracture mechanics versus elastic–plastic fracture mechanics“, *Eng. Fract. Mech.*, Bd. 73, Nr. 4, S. 435–455, 2006, doi: https://doi.org/10.1016/j.engfracmech.2005.08.010.

[97] J. Yan, B. Taskonak, J. A. Platt, und J. J. Mecholsky, „Evaluation of fracture toughness of human dentin using elastic–plastic fracture mechanics“, *J. Biomech.*, Bd. 41, Nr. 6, S. 1253–1259, 2008, doi: https://doi.org/10.1016/j.jbiomech.2008.01.015.

[98] A. S. Argon, *The Physics of Deformation and Fracture of Polymers*. Cambridge: Cambridge University Press, 2013.

[99] J. R. Rice, „A Path Independent Integral and the Approximate Analysis of Strain Concentration by Notches and Cracks“, *J. Appl. Mech.*, Bd. 35, Nr. 2, S. 379–386, Juni 1968, doi: 10.1115/1.3601206.

[100] J. Wiener, F. Arbeiter, A. Tiwan, O. Kolednik, und G. Pinter, „Bioinspired toughness improvement through soft interlayers in mineral reinforced polypropylene“, *Mech. Mater.*, Bd. 140, S. 1–13, 2020, doi: https://doi.org/10.1016/j.mechmat.2019.103243.

[101] O. Kolednik, J. Predan, F. D. Fischer, und P. Fratzl, „Bioinspired Design Criteria for Damage-Resistant Materials with Periodically Varying Microstructure“, *Adv Funct Mater*, Nr. 21, S. 3634–3641, 2011, doi: 10.1002/adfm.201100443.

[102] M. Pfaffinger, *Entwicklung und Optimierung photopolymerisierbarer Schlicker für den Lithography-based ceramic manufacturing (LCM) Prozess*. Wien, 2017.

[103] M. Pfaffinger, M. Hartmann, M. Schwentenwein, und J. Stampfl, „Stabilization of tricalcium phosphate slurries against sedimentation for stereolithographic additive manufacturing and influence on the final mechanical properties“, *Int. J. Appl. Ceram. Technol.*, Bd. 14, Nr. 4, S. 499–506, 2017, doi: https://doi.org/10.1111/ijac.12664.

[104] M. Hartmann, *Chemische und technologische Optimierung der lithografie-basierten Additiven Fertigung von Dentalkeramik*. Wien, 2020. [Online]. Verfügbar unter: 20.500.12708/16992

[105] U. Blaschke, K. Eismann, A. Böhme, A. Paschke, und G. Schüürmann, „Structural Alerts for the Excess Toxicity of Acrylates, Methacrylates, and Propiolates Derived from Their Short-Term and Long-Term Bacterial Toxicity“, *Chem. Res. Toxicol.*, Bd. 25, Nr. 1, S. 170–180, Jan. 2012, doi: 10.1021/tx200395k.

[106] F. Kotz, P. Risch, D. Helmer, und B. Rapp, „Highly Fluorinated Methacrylates for Optical 3D Printing of Microfluidic Devices“, *Micromachines*, Bd. 9, Nr. 115, März 2018, doi: 10.3390/mi9030115.

[107] B. Steyrer, P. Neubauer, R. Liska, und J. Stampfl, „Visible Light Photoinitiator for 3D-Printing of Tough Methacrylate Resins“, *Materials*, Bd. 10, Nr. 1445, 2017.

[108] „Tango: A Soft Flexible 3D Printing Material - Stratasys“. https://www.stratasys.com/en/materials/materials-catalog/polyjet-materials/tango/ (zugegriffen 16. März 2022).

[109] J. Ebert, W. Wachter, G. Rohner, und J. Stampfl, „Verfahren Zum Aufbau Eines Dreidimensionalen Formkörpers“, EP2855119B1, 24. Februar 2016

[110] M. M. R. A. Lima, R. C. C. Monteiro, M. P. F. Graça, und M. G. F. da Silva, „Structural, electrical and thermal properties of borosilicate glass–alumina composites“, *J. Alloys Compd.*, Bd. 538, S. 66–72, 2012, doi: https://doi.org/10.1016/j.jallcom.2012.05.024.

[111] D. Quéré, „Wetting and Roughness“, *Annu. Rev. Mater. Res.*, Bd. 38, Nr. 1, S. 71–99, 2008, doi: 10.1146/annurev.matsci.38.060407.132434.

[112] J. Stögerer, S. Baumgartner, T. Rath, und J. Stampfl, „Analysis of the mechanical anisotropy of stereolithographic 3D printed polymer composites“, *Eur. J. Mater.*, Bd. 0, Nr. 0, S. 1–21, 2022, doi: 10.1080/26889277.2022.2035196.

[113] S. C. Ligon, B. Husár, H. Wutzel, R. Holman, und R. Liska, „Strategies to Reduce Oxygen Inhibition in Photoinduced Polymerization“, *Chem. Rev.*, Bd. 114, Nr. 1, S. 557–589, Jan. 2014, doi: 10.1021/cr3005197.

[114] J. Stögerer, S. Baumgartner, A. Hochwallner, und J. Stampfl, „Bio-Inspired Toughening of Composites in 3D-Printing“, *Materials*, Bd. 13, Nr. 21, 2020, doi: 10.3390/ma13214714.

[115] R. A. Ketcham und T. M. Ryan, „Quantification and visualization of anisotropy in trabecular bone“, *J. Microsc. Oxf.*, Bd. 213, Nr. 2, S. 158–171, 2004.

[116] C. Dong, Y. Yang, C. Yuan, X. Bai, und Z. Guo, „Effects of anisotropy of lignum vitae wood on its tribological performances“, *Compos. Part B Eng.*, Bd. 228, S. 109426, 2022.

[117] C. Buksnowitz, R. Evans, U. Müller, und A. Teischinger, „Indented rings (hazel growth) of Norway spruce reduce anisotropy of mechanical properties“, *Wood Sci. Technol.*, Bd. 46, Nr. 6, S. 1239–1246, 2012.

[118] T. Ozyhar, S. Hering, und P. Niemz, „Moisture-dependent elastic and strength anisotropy of European beech wood in tension“, *J. Mater. Sci.*, Bd. 47, Nr. 16, S. 6141–6150, 2012.

[119] M. Monzon, Z. Ortega, A. Hernandez, R. Paz, und F. Ortega, „Anisotropy of Photopolymer Parts Made by Digital Light Processing“, *Materials*, Bd. 10, Nr. 64, 2017, doi: 10.3390/ma10010064.

[120] S. Shanmugasundaram, J. Razmi, J. Mian, und L. Ladani, „Mechanical Anisotropy and Surface Roughness in Additively Manufactured Parts Fabricated by Stereolithography (SLA) Using Statistical Analysis“, *Materials*, Bd. 13, Nr. 2496, 2020, doi: 10.3390/ma13112496.

[121] T. McLouth, J. Severino, P. Adams, D. Patel, und R. Zaldivar, „The impact of print orientation and raster pattern on fracture toughness in additively manufactured ABS“, *Addit. Manuf.*, Bd. 18, S. 103–109, 2018, doi: http://dx.doi.org/10.1016/j.addma.2017.09.003.

[122] Y. Li *u. a.*, „Isotropic stereolithography resin toughened by core-shell particles“, *Chem. Eng. J.*, Bd. 394, S. 124873, Aug. 2020, doi: 10.1016/j.cej.2020.124873.

[123] R. Hague, S. Mansour, N. Saleh, und R. Harris, „Materials analysis of stereolithography resins for use in Rapid Manufacturing“, *J. Mater. Sci.*, Bd. 39, Nr. 7, S. 2457–2464, Apr. 2004, doi: 10.1023/B:JMSC.0000020010.73768.4a.

[124] D. Kazmer und M. Kutz, „Three-dimensional printing of plastics, applied plastics engineering handbook-processing, materials, and applications“, *Vol. Plast. Des. Libr.*, Nr. 2, S. 617–634, 2017.

[125] „Plastics — Determination of fracture toughness (GIC and KIC) — Linear elastic fracture mechanics (LEFM) approach (ISO 13586)“. 2018.

[126] N. M. Razali und Y. B. Wah, „Power comparisons of Shapiro-Wilk, Kolmogorov-Smirnov, Lilliefors and Anderson-Darling tests“, *J. Stat. Model. Anal.*, Nr. 2, S. 21–33, 2011.

[127] N. Celik, „Welch’s ANOVA: Heteroskedastic skew-t error terms“, *Commun. Stat. - Theory Methods*, S. 1–12, Juli 2020, doi: 10.1080/03610926.2020.1788084.

[128] S.-L. Jan und G. Shieh, „Sample size determinations for Welch’s test in one-way heteroscedastic ANOVA“, *Br. J. Math. Stat. Psychol.*, Nr. 67, S. 72–93, 2013, doi: 10.1111/bmsp.12006.

[129] J. Aizenberg, J. C. Weaver, M. S. Thanawala, V. Sundar, D. E. Morse, und P. Fratzl, „Skeleton of Euplectella sp.: Structural Hierarchy from the Nanoscale to the Macroscale“, *Science*, Bd. 309, S. 275–278, doi: DOI: 10.1126/science.1112255.

[130] J. C. Weaver *u. a.*, „Hierarchical assembly of the siliceous skeletal lattice of the hexactinellid sponge Euplectella aspergillum“, *J. Struct. Biol.*, Bd. 158, S. 93–106, doi: doi:10.1016/j.jsb.2006.10.027.

[131] S. L. Walter, B. D. Flinn, und G. Mayer, „Mechanisms of toughening of a natural rigid composite“, *Mater. Sci. Eng.*, Bd. 27, S. 570–574, 2007, doi: doi:10.1016/j.msec.2006.05.020.

[132] J. W. C. Dunlop, R. Weinkamer, und P. Fratzl, „Artful interfaces within biological materials“, *Mater. Today*, Bd. 14, S. 70–78, 2011.

[133] O. Kolednik, J. Predan, und F. D. Fischer, „Cracks in inhomogeneous materials: Comprehensive assessment using the configurational forces concept“, *Eng. Fract. Mech.*, Bd. 77, S. 2698–2711, 2010, doi: doi:10.1016/j.engfracmech.2010.07.002.

[134] M. Sistaninia und O. Kolednik, „Effect of a single soft interlayer on the crack driving force“, *Eng. Fract. Mech.*, Bd. 130, S. 21–41, 2014, doi: http://dx.doi.org/10.1016/j.engfracmech.2014.02.026.

[135] P. Fratzl, H. S. Gupta, F. D. Fischer, und O. Kolednik, „Hindered Crack Propagation in Materials with Periodically Varying Young’s Modulus—Lessons from Biological Materials“, *Adv. Mater.*, Bd. 19, S. 2657–2661, 2007, doi: https://doi.org/10.1002/adma.200602394.

[136] D. Gross und T. Seelig, *Bruchmechanik: Mit einer Einführung in die Mikromechanik*, 6. Aufl. 2016. Berlin, Heidelberg: Springer Berlin Heidelberg.

[137] G. E. Hale und F. Ramsteiner, „J-Fracture toughness of polymers at slow speed“, Bd. 28, Nr. ISSN: 1566-1369, S. 157, 2001, doi: 10.1016/S1566-1369(01)80031-5.

[138] K.-H. Schwalbe und B. Neale, „A procedure for determining the fracture behaviour of materials. The unified fracture mechanics test method. EFAM GTP 94, *Fatigue Frac. Eng. Mater. Struct.*, Bd. 18, Nr. ISSN: 8756-758X, S. 424, 1995, doi: 10.1111/j.1460-2695.1995.tb01185.x.

[139] N. Ioannides *u. a.*, „Approaches to mitigate polymer-core loss in plastic optical fibers: A review“, *Mater. Res. Express*, Bd. 1, S. 032002, Sep. 2014, doi: 10.1088/2053-1591/1/3/032002.

[140] S. Wille, I. Hölken, H. Galina, R. Adelung, und M. Kern, „Biaxial flexural strength of new Bis-GMA/TEGDMA based composites with different fillers for dental applications“, *Dent. Mater.*, Bd. 32, S. 1073–1078, 2016, doi: https://doi.org/10.1016/j.dental.2016.06.009.

[141] R. Wang, E. Habib, und X. X. Zhu, „Evaluation of the filler packing structures in dentalresin composites: From theory to practice“, *Dent. Mater.*, Bd. 34, S. 1014–1023, 2018, doi: 10.1016/j.dental.2018.03.022.

[142] S. Beigi, H. Yeganeh, und M. Atai, „Evaluation of fracture toughness and mechanical properties of ternary thiol–ene–methacrylate systems as resin matrix for dental restorative composites“, *Dent. Mater.*, Bd. 29, S. 777–787, 2013, doi: http://dx.doi.org/10.1016/j.dental.2013.04.015.

[143] H. Chai, X. Wang, und J. Sun, „Miniature specimens for fracture toughnessevaluation of dental resin composites“, *Dent. Mater.*, Bd. 35, S. 283–291, 2019, doi: 10.1016/j.dental.2018.11.023.